The University of Manchester

Optical Coherence Tomography: applications and developments for imaging in vivo biological tissue

A thesis submitted to The University of Manchester for the degree of Doctor of Philosophy

in the Faculty of Engineering and Physical Sciences

2011

Graham Dinsdale

The Photon Science Institute

School of Physics and Astronomy

Table of contents

Final word count: 37,791

Table of figures

Abstract

The work presented in this thesis was re-submitted to The University of Manchester for the degree of Doctor of Philosophy in July 2011 by Graham Dinsdale and is entitled “Optical Coherence Tomography: applications and developments for imaging in vivo biological tissue”.

In this thesis the design and build of a high-speed, video-rate optical coherence tomography (OCT) imaging system is described. The system was designed for the purpose of imaging human skin in vivo, particularly that of patients suffering from conditions such as systemic sclerosis. Component selection and design decisions are discussed in the context of the intended final application. Initial test images from the system are presented. In the context of building an OCT system, a supercontinuum light source was characterised and tested for its suitability for use in the OCT environment. Parameters such as coherence length were measured using simple interferometry techniques, while practical considerations such as portability and ease of system integration were also considered.

Several applications of OCT imaging techniques were also investigated, using two commercially-available OCT systems from Thorlabs, Inc. A liquid-based skin and blood flow model was constructed using narrow glass capillary tubes, pumped through with scattering solutions of Intralipid or suspensions of polystyrene microspheres. The concentration of the solutions was tuned by dilution in order to best model the scattering parameters of blood. The model also used similar liquid solutions to model static tissue surrounding the blood vessels. Doppler OCT images of the model under various conditions were recorded, and velocity profiles of the flowing liquids were extracted.

Using the same commercial OCT systems, imaging over two separate wavelength regions was also performed on the skin of several different species of neo-tropical tree frog, some of which have interesting reflective properties due to the presence of a pigment called pterorhodin. Cross-sectional OCT images of the skin are presented, and averaged depth profiles extracted from them. This is the first time that OCT imaging has been applied to this problem.

A clinical study of skin thickening and microvascular function in patients with systemic sclerosis compared to healthy controls was also carried out, again involving a Thorlabs, Inc. commercial OCT system. This study was carried out at Salford Royal Hospital under the supervision of the rheumatology research group. Skin thickness was assessed using OCT and high-frequency ultrasound imaging. Microvascular function was measured using nailfold cappilaroscopy and laser Doppler imaging. Images from the study are presented here.

Declaration

No portion of the work referred to in this thesis has been submitted in support of an application for another degree or qualification of this or any other university or institute of learning.

Copyright statement

Publications and presentations

Conference presentation

G. Dinsdale, N. Bensaid, A.K. Murray, P.E.C. Brenchley and M.R. Dickinson, "Blood flow modelling and imaging with Doppler optical coherence tomography (DOCT)", Photonics Northwest 2008, The University of Manchester, May 8th 2008.

Conference poster

G. Dinsdale, N. Bensaid, A.K. Murray, P.E.C. Brenchley and M.R. Dickinson, "A liquid-based skin and blood flow model for Doppler optical coherence tomography imaging", BiOS, SPIE Photonics West 2009, San Jose, California, USA, January 26th 2009.

Conference proceedings

G. Dinsdale, N. Bensaid, A.K. Murray, P.E.C. Brenchley and M.R. Dickinson, "A liquid-based skin and blood flow model for Doppler optical coherence tomography imaging", Proc. SPIE, Vol. 7168, (2009).

Journal article

G. Dinsdale, D. Buckley, T. Moore, J. Manning, E. Wragg, J. Shin, M. Dickinson, C. Griffiths, A. Murray and A. Herrick, "Comparison of skin thickness and microvascular structure and function in patients with systemic sclerosis and healthy controls", (in preparation).

Acknowledgments

Firstly I would like to thank my supervisor Dr. Mark Dickinson for all of his help and support over the last 4 years. His guidance and help throughout have been great, and I have particularly appreciated his practical troubleshooting skills on many occasions. I would also like to thank my second supervisor, Dr. Andrea Murray. Her support and insight have been invaluable to me, and she has shown patience and kindness beyond measure. Without her this work would not have been possible. Thank you to both of you for so much of your time.

Secondly, I would like to thank Professor Paul Brenchley for allowing me the long-term use of the SS-OCT imaging system. This has allowed me to gain experience and results that otherwise would not have been possible. I would also like to thank The Wellcome Trust Clincial Research Facility for allowing the loan of their OCT system for use in the patient study. Thanks must also go to Mohammed Benyezzar for writing the OCT system software, and also to Michael Needham for his help with all electronic matters.

All members of the Rheumatology research group at Salford Royal Hospital deserve my appreciation for helping me in co-ordinating and running the patient study. Particular thanks must go to Tonia Moore for finding suitable study patients and generally making me feel welcome. I would also like to thank my colleagues in the PSI, particularly Stuart, Donna, Reem and Jen, for the drinks, laughs and interesting discussions.

Special thanks go to my parents, and the rest of my family, for their support and encouragement over the years, and their continuing belief in me. Finally, to my girlfriend Joanne I want to say thank you, from the bottom of my heart, for helping me through this.

Chapter 1

Introduction

1.1 An introduction to Optical Coherence Tomography

Optical coherence tomography is a non-invasive technique for obtaining cross-sectional images in scattering media. It utilises the interference properties of low coherence, broadband light sources to provide a depth profile of discontinuities within a sample. Optical coherence tomography is commonly known by the acronym OCT.

OCT was first demonstrated almost 20 years ago [1] as an extension of low-coherence reflectometry. A broadband light source coupled into an interferometer will produce interference fringes at its output only when the optical path lengths of the two arms are equal to within the coherence length of the light source. Low-coherence reflectometry [2], also known as optical coherence domain reflectometry [3], exploits this fact by placing a sample in one arm of the interferometer and a movable mirror in the other. As the mirror is scanned along its axis of reflection, interference is observed only when the optical path lengths to both the mirror and a reflecting object within the sample are equal. OCT produces tomographic images by recording many such longitudinal scans at neighbouring lateral sites.

The OCT field has developed at a rapid pace since its inception due to parallel developments in many of the contributing areas of technology. Advances in computing, data acquisition hardware, light sources, and optical techniques have all allowed OCT to mature quickly and find wide usage, particularly in medical and biological applications. Video-rate imaging at near micron axial resolutions is now fairly routine [4], with fast 4D imaging now becoming a real possibility [5]. OCT systems have found uses in medical fields ranging from ophthalmology to cardio-vascular surgery.

1.2 Motivation & aims

1.2.1 Motivation

The specific motivation for this thesis on OCT comes from an inter-disciplinary link-up with the Dermatological Sciences research group at Salford Royal hospital. The group studies the causes and symptoms of various skin conditions including psoriasis, scleroderma and Raynaud's phenomenon, as well as investigating potential novel treatments. The common link between these conditions is that they all affect the cutaneous microcirculation in some way, as confirmed using techniques such as laser Doppler imaging (LDI) [6] and nail fold capillaroscopy [7] (see section 7.2 and Figure 7.1 for more detail). Monitoring blood flow velocity and flow volume in the microcirculation of patients may provide useful information on, for example, the effect of a particular treatment. The LDI technique can provide flow velocity information from a specific site, but its results are highly dependent on the volume illuminated (which must be estimated). Nail fold capillaroscopy provides excellent structural images of a specific area of the microvasculature, but cannot measure blood flow rates. OCT, functionalized as Doppler OCT (DOCT) is capable of providing both high-resolution structural imaging and flow velocity information from blood vessels within tissue, making it ideal for imaging the microvasculature in these cases.

The study of OCT and OCT imaging encompasses a wide range of fields and technologies, from optical hardware and light sources to image processing and light scattering. This provides a more general motivation within this thesis to look at OCT techniques, systems, and hardware with a view to finding improvements, new applications and imaging opportunities.

1.2.2 Aims

The specific aim of this work has been to design and build an OCT imaging system to be used for imaging the microcirculation in human patients with various skin conditions. The system should produce high resolution structural OCT images, as well as extracting dynamic information on blood flow. Requirements placed on the system capabilities include “video-rate” imaging, live image viewing, and an ability to resolve structures on the scale of the human microvasculature (~10μm length scale).

The general aim of this work has been to investigate the various facets of optical coherence tomography and associated imaging techniques. Areas to be considered include data capture and image processing, as well as possible hardware advances such as new light sources and interferometric systems. Also of interest are new imaging opportunities for OCT, such as previously untested samples/subjects, along with physical modelling of tissue systems to investigate OCT imaging capabilities in the lab.

1.3 Summary of chapters

Chapter 1 (this chapter) introduces the thesis and sets out the aims and motivations for the work described.

Chapter 2 contains OCT theory combined with a review of the relevant literature. Interference effects using broadband light sources are discussed, along with a brief overview of the development of the OCT field. A discussion of optical loss, noise and Fourier domain OCT is also included.

Chapter 3 describes the design, test, and building of a high-speed OCT system suitable for imaging in vivo. The design and testing of all system components is described, as well as the reasons why certain design decisions were made. Initial “lab bench” images taken with the system are also presented and discussed in this chapter.

Chapter 4 details the testing and characterization of a supercontinuum light source, and examines its suitability for use in OCT imaging. Time constraints involving the loan of the light source prevented extensive testing, although potential imaging characteristics, such as resolution, were measured.

Chapter 5 describes work done in modelling blood flow and tissue using liquids in glass capillary tubes. Doppler OCT imaging was performed on the models. Colour-coded images representing phase-shift induced by flow within the models are examined, and the possibility of extracting velocity flow profiles from such images is explored.

Chapter 6 describes dual-wavelength OCT imaging of the skin of certain species of neotropical treefrog, in an attempt to isolate the location of the pigment pterorhodin within the skin. Tree frogs with skin containing the pigment pterorhodin are known to survive amphibian fungal diseases better than other frog species and it is believed that the pigment may confer these advantages to the frog.

Chapter 7 gives details of a clinical study carried out at Salford Royal Hospital. The study involved measuring skin thickness and blood flow in patients with scleroderma, and healthy controls. The imaging techniques used were OCT, high-frequency ultrasound, nailfold capillaroscopy, and laser Doppler imaging.

Chapter 8 gives a summary of the conclusions that can be drawn from the various studies presented in this thesis, and explores some ideas for further work.

References

[1] D. Huang, E.A. Swanson, C.P. Lin et al., *Science* **254** (5035), 1178 (1991).

[2] K. Takada, I. Yokohama, K. Chida et al., *Applied optics* **26** (9), 1603 (1987).

[3] R.C. Youngquist, S. Carr, and D.E.N. Davies, *Optics Letters* **12** (3), 158 (1987).

[4] W. Drexler, *Journal of Biomedical Optics* **9** (1), 47 (2004).

[5] M. W. Jenkins, O. Q. Chughtai, A. N. Basavanhally et al., *Journal of Biomedical Optics* **12** (3), 30505 (2007); A. V. Zvyagin, P. Blazkiewicz, and J. Vintrou, San Jose, CA, USA, 2005 (unpublished).

[6] A.K. Murray, T. L. Moore, T. A. King et al., *Arthritis Rheum.* **54** (6), 1952 (2006).

[7] A. L. Herrick, T. L. Moore, A. K. Murray et al., *Rheumatology* **49** (9), 1776 (2010).

Chapter 2

Theory and literature review

2.1 Coherence

The construction of the first functioning laser in 1960 by Theodore Maiman provided a new type of light source, with some extremely useful properties. Maiman, working at Hughes Research Laboratories in California, produced a laser with an output wavelength of 694nm operating in a pulsed mode [1]. Compared to traditional sources of light such as incandescent bulbs the laser has three main advantages. Firstly, the geometry of the device and the gain material used control the output wavelength very precisely; restricting it generally to a very narrow band of wavelengths. Secondly and again related to the device geometry, the output of a laser is easily formed into a beam with a small spatial extent. Even in semiconductor laser devices where the initial output can be highly divergent, the addition of a simple lens can form a tightly collimated beam; this is not always possible when dealing with non-laser devices. The third advantage afforded by laser devices arises from the second; the tightly collimated beam with low divergence results in the laser output being very "bright". That is, the power delivered by the laser device over a given area is relatively high, the laser is said to have a high irradiance (or intensity) output; the units of this particular property being Watt per square metre (Wm^{-2}).

The result of these improvements is a light source whose output has definable and controllable coherence. There are two types of coherence to consider: spatial and temporal coherence.

Spatial coherence is related to the “flatness” of wave fronts emitted by a light source. It is a measure of the time-averaged ability of two points on a wave front to interfere with each other. Perfectly flat, parallel wave fronts are said to have infinite spatial coherence, since interference is possible at all points due to the constant phase relationship across the wave front. Waves with finite spatial coherence exhibit a varying phase relationship across the wave front, with the result that only points across the wave front within a certain distance (or area, for 2-dimensional wave fronts) of each other are able to produce interference. This measure of finite spatial coherence is known as the coherence area, which is the area of the cross section of a beam that has a constant phase relationship.

Light with infinite spatial coherence can be produced by passing spatially incoherent light through a slit or hole smaller than the coherence area of the wave front. The typical speckle pattern produced by a laser beam incident upon a surface is a result of the spatial coherence properties of the beam.

Temporal coherence is a measure of how well the phase of an emitted light wave can be predicted at some time after emission. The coherence time, τ_c, defines the time from emission that a wave front has a predictable phase relationship with light emitted both before and after it. It is a direct result of the range of frequencies emitted by the source. This relationship between coherence time, τ_c, and source bandwidth, Δf, is defined in Equation 2.1 as

$$\tau_c \propto \frac{1}{\Delta f} \qquad (2.1).$$

That is, the coherence time of the source is inversely proportional to the bandwidth [2]. From this it is obvious that narrow bandwidth sources, such as high-quality lasers, have long coherence times, while broadband sources have short coherence times. Another way of considering the effects of temporal coherence is to consider the distance light travels during the coherence time, τ_c. This distance, known as the coherence length, l_c, is calculated by multiplying the coherence time by the speed of light, c.

$$l_c = c\tau_c \qquad (2.2).$$

The coherence length, as defined in Equation 2.2, is a fundamental property of all light sources, from lasers to filament bulbs. If Equations 2.1 and 2.2 are considered together, it can be seen that the coherence length is also inversely proportional to the source bandwidth. Optical Coherence Tomography makes use of the short coherence lengths provided by broadband light sources to produce high-resolution images using interference techniques.

2.2 Interferometry and broadband light

Optical Coherence Tomography involves using backscattered light from a sample to make time-of-flight measurements of distances and structures. The typical analogy used to describe OCT is to compare it to B-mode ultrasound imaging, replacing sound waves with light [3]. In both techniques, the waves are reflected or backscattered from discontinuities in the sample. These discontinuities are places where the speed of transmission through the medium changes; either altering the speed of sound due to material density changes, or refractive index boundaries affecting light transmission.

The major difference between ultrasound imaging and OCT (aside from the obvious one of sound versus light) is in the way that the backscatter/reflection information is recorded. In ultrasound imaging, the speed of sound, v_s, in tissue samples is around 1500 ms^{-1}, and a typical ultrasound imaging system might have a frequency, f, of 10 MHz. Thus the wavelength, λ, and therefore resolution limit of such a system is

$$\begin{aligned} v_s &= f\lambda \\ \lambda &= \frac{v_s}{f} \\ \lambda &= \frac{1500 ms^{-1}}{10 MHz} \\ \lambda &= 150 \mu m \end{aligned} \qquad (2.3).$$

As shown in Equation 2.3 the resolution of a clinical ultrasound system is >100 µm. Time-of-flight signals generated with such systems require time resolution on the order of 10-100 ns; well within the capabilities of standard electronic circuitry. This means that ultrasound systems measure *directly* the time it takes for sound waves to travel to and from a particular boundary. In comparison, the much higher speed of light, coupled with the smaller wavelengths involved (~1 µm) means that OCT would require time resolutions into the range of femtoseconds (10^{-15} second); far beyond the capabilities of current detection electronics. It should be noted that light travels approximately 30 cm in 1 ns, so if a direct measurement system were implemented using conventional electronics this would be the minimum measurable distance. Such a direct measurement technique is used for measuring defects and overall attenuation in fibre optic cables, particularly in the telecommunications industry, and is known as Optical Time Domain Reflectometry (OTDR) [4].

Since direct time-of-flight measurements are impossible with backscattered light over short (mm/sub-mm) distances, an indirect technique is the only way to proceed. Correlating backscattered light from a sample with a reference beam using interferometric techniques is one way to do this.

2.2.1 Laser light and the Michelson interferometer

The Michelson interferometer, as used in the famous Michelson-Morley test of special relativity, is the simplest form of interferometer. It involves splitting the output of a light source into two, usually perpendicular, beams. This is done using a beamsplitter, which can be as simple as a thin glass plate; although half-silvered mirrors are more often used in free space systems to control the amount of light in each beam. A schematic diagram of this is shown in Figure 2.1, below.

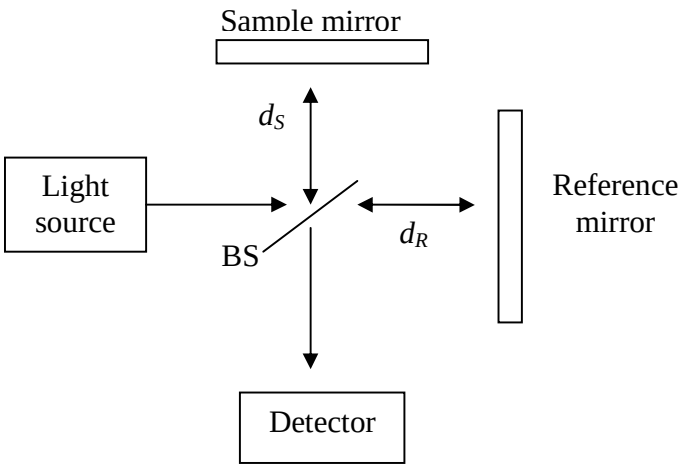

Figure 2.1. Schematic diagram of a Michelson interferometer. The distances from the beamsplitter (labelled BS) to the sample and reference mirrors are d_S and d_R respectively.

After the beams are split, they are each incident on a mirror, labelled *sample* and *reference*. After reflection from their respective mirrors, the beams are re-combined at the beamsplitter, producing an interference pattern that travels to the detector. The distances from the beamsplitter to the sample and reference mirrors are d_S and d_R, respectively. In the case were the light source produces a single wavelength of light (i.e. it is monochromatic) the electric field components from each arm, E_S and E_R, incident on the detector can be written as:

$$E_S = A_S \exp\left[-i\left(2d_S - \omega t\right)\right] \text{ and } E_R = A_R \exp\left[-i\left(2d_R - \omega t\right)\right] \qquad (2.4).$$

In Equation 2.4, ω is the frequency of the monochromatic light source, time is denoted as t, and A_S and A_R are the amplitudes of the electric field in each of the beams. The current produced by the detector, I, is proportional to the squared sum of the phasors in Equation 2.4 and can be written as:

$$I = K\left[\frac{|A_S|^2}{2} + \frac{|A_R|^2}{2} + real\left(E_S E_R^*\right)\right] \qquad (2.5).$$

The constant, K, in equation 2.4 incorporates various terms, including the electronic charge, photon energy, and detector quantum efficiency. The terms involving the amplitudes, A_s and A_R, are also constant for a given light source and system configuration. The only term which varies is the final one, which can be expanded and simplified to:

$$real\left(E_S E_R^*\right) = A_S A_R \cos\left(\frac{4\pi\Delta d}{\lambda}\right) \qquad (2.6).$$

The output of the detector therefore varies as a (co-)sinusoidal function of the difference in path lengths between the sample and reference arms, Δd. The $4\pi/\lambda$ term in Equation 2.6 is actually made up of two parts: $2\pi/\lambda$ is the propagation constant for both reference and sample beams in free-space, while the extra factor of 2 comes from the fact that the beams traverse the distance from beamsplitter to mirror twice (via the return journey).

The result of the above relationships is that, if the reference mirror is smoothly scanned in the direction of beam propagation, the detector output will vary sinusoidally, with a period of $\lambda/2$. However, this only allows relative distances to be measured, in terms of whether the two beams produce constructive interference (0, 2π, 4π etc. relative phase shift) or destructive intereference (π, 3π, 5π etc.relative phase shift). Of course, all of the above is predicated on using perfectly monochromatic light. To enable absolute measurement of distances using interferometry, the results of using polychromatic, or broadband light sources needs to be considered.

2.2.2 Broadband light and the Michelson interferometer

When broadband light is introduced into the Michelson interferometer a similar treatment to that used in section 2.2.1 can be implemented. As mentioned previously, broadband light can also be defined as low-coherence light with a coherence length, l_C; that is light which has a definable phase relationship over only a small distance. The theoretical monochromatic source considered previously would have an infinite coherence length.

To calculate the variation in detector output due to the numerous frequency components present in a partially-coherent, broadband source, the cross-spectral term (Equation 2.6) must be integrated over the range of frequencies present. The electric field components E_S and E_R must now be considered as varying as a function of frequency. In a similar fashion to Equation 2.5 the detector current, I, can be written as:

$$I \propto real\left[\int_{-\infty}^{\infty} \frac{1}{2\pi} E_S(\omega) E_R^*(\omega) d\omega\right] \qquad (2.7),$$

where the electric field components, $E_S(\omega)$ and $E_R(\omega)$, are defined respectively as:

$$\begin{aligned} E_S(\omega) &= A_S(\omega)\exp[-i(2p_S(\omega)d_S - \omega t)] \\ E_R(\omega) &= A_R(\omega)\exp[-i(2p_R(\omega)d_R - \omega t)] \end{aligned} \qquad (2.8).$$

In Equation 2.8 the factors $p_S(\omega)$ and $p_R(\omega)$ are the propagation constants for light in the sample and reference arms, as a function of optical frequency. By combining Equations 2.7 and 2.8 we get:

$$I \propto real\left[\int_{-\infty}^{\infty} \frac{1}{2\pi} S(\omega)\exp[-i\Delta\phi(\omega)d\omega]\right] \qquad (2.9)$$

where:

$$\begin{aligned} S(\omega) &= A_S(\omega)A_R^*(\omega) \\ \Delta\phi(\omega) &= 2p_S(\omega)d_S - 2p_R(\omega)d_R \end{aligned} \qquad (2.10).$$

The term $S(\omega)$ is the power spectrum of the light source, since both arms of the interferometer contain the same spectral information. The term $\Delta\varphi(\omega)$ is the phase difference for each frequency component incident on the detector.

The propagation constants, p_S and p_R, are again equal, since there is no difference between the sample and reference arms, an can be re-named p. If the light source has a

spectrum $S(\omega-\omega_0)$, the phase difference $\Delta\varphi(\omega)$ from Equation 2.10 can be re-written using a 1st-order Taylor expansion to be:

$$\Delta\phi(\omega) = p(\omega_0)(2\Delta d) + p'(\omega_0)(\omega-\omega_0)(2\Delta d) \qquad (2.11).$$

In Equation 2.11 the light source central frequency is denoted as ω_0. Equation 2.11 shows again that only the differences in the lengths of the two beam paths affect the phase mismatch at the detector.

The integral in Equation 2.9 can now be re-written as:

$$I \propto real\left\{\exp\left[-i\omega_0\Delta\tau_p\right]\int_{-\infty}^{\infty}\frac{1}{2\pi}S(\omega-\omega_0)\exp\left[-i(\omega-\omega_0)\Delta\tau_g\right]d(\omega-\omega_0)\right\} \qquad (2.12),$$

with $\Delta\tau_p$ being the phase delay difference, and $\Delta\tau_g$ being the group delay difference. These delay differences can be shown to be equal to $2\Delta d$ divided by either the phase or group velocity. Equation 2.12 is related to the Wiener-Khinchin theorem, stating that the inverse Fourier transform of the power spectrum is equal to the autocorrelation function [5]. The photocurrent produced when using partially coherent (broadband) light in a Michelson interferometer has an oscillating component, with frequency ω_0 equal to the central frequency of the source. The photocurrent also has an envelope, defined as the inverse Fourier transform of the source spectrum.

If the light source used has a Gaussian spectral output, it can be shown that the photocurrent envelope also has a Gaussian shape with a width inversely proportional to the spectral bandwidth. Interference fringes produced by the oscillating term in Equation 2.12 are only visible when the group delay, $\Delta\tau_g$, is within the Gaussian envelope, i.e. the reference and sample arms are matched in length. If the width of the Gaussian current envelope is 2σ, then:

$$-\sigma < \Delta\tau_g < \sigma \qquad (2.13)$$

The full-width at half-maximum (FWHM), Δd, of this Gaussian envelope in terms of source central wavelength, λ_0, and bandwidth, $\Delta\lambda$, can then be written as:

$$\Delta d = \frac{2\ln 2}{\pi}\left(\frac{\lambda_0^2}{\Delta\lambda}\right) \qquad (2.14).$$

Equation 2.14 defines the axial resolution of an interferometer system using a broadband light source with a Gaussian spectrum.

All of the above provides a method of absolute measurement of on-axis position using light. This is because, for polychromatic light sources, interference fringes are only visible when the two arms of the interferometer are equal in length to within the resolution limit defined in Equation 2.14.

It is a relatively small step to make from seeing interference fringes produced from two mirrors only when the path lengths of an interferometer are matched to within a certain distance, to producing depth profiles of backscattering/reflecting samples. If the "sample" mirror in Figure 2.1 is replaced with an actual sample (e.g. tissue) consisting of several boundaries we have the situation as shown in Figure 2.2.

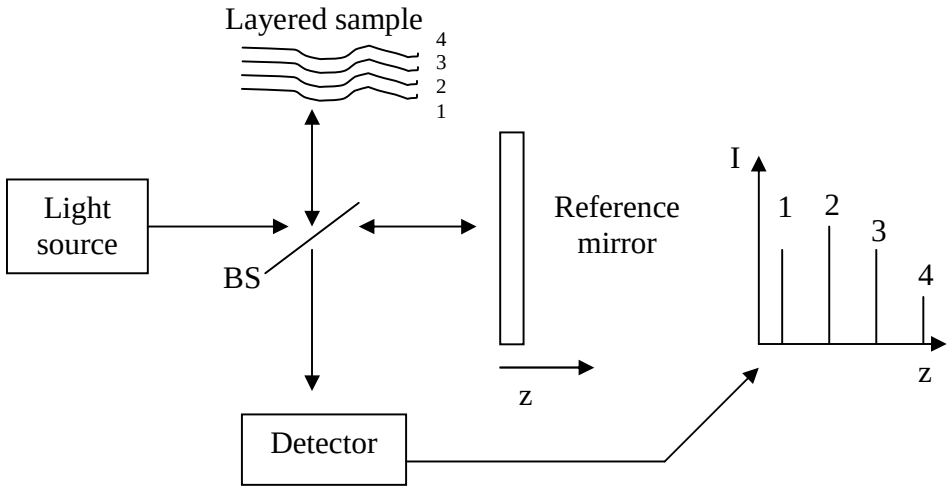

Figure 2.2. Schematic of Michelson interferometer with layered sample and scanning reference arm showing detector output.

In Figure 2.2, instead of a perfectly reflecting mirror in the sample arm of the interferometer, there is now a sample consisting of several layers numbered 1 to 4. At the boundary to each layer a small fraction of the incident light will be scattered or reflected due to the discontinuity in the refractive index. The sample can be considered as being made up of a stack of poorly reflecting mirrors. If one of the layers happens to be positioned at the point where the sample and reference arms are equal in length, an interference signal will be visible. If the reference mirror is scanned in the axial (z) direction, an interference signal will be produced whenever the path length to the mirror is equal to that to one of the layers in the sample. By simply moving the reference mirror axially a depth profile of the sample can be obtained, as shown in the example graph in Figure 2.2. The intensity, *I*, of the interference signal, or more correctly, the amplitude of the interference envelope, will depend on the strength of the reflection/scatter from a particular boundary.

2.3 Early developments in Optical Coherence Tomography

So far it has been shown how using broadband light in conjunction with interferometric techniques can allow measurement of reflections and backscatter from layers within a sample. This idea was first put to use in a technique called Optical Coherence-Domain Reflectometry, a natural progression from the aforementioned OTDR technique. OCDR, also known as low-coherence reflectometry, was first described in 1987, and was used to find reflection sites in miniature optical assemblies [6]. An 830 nm short-coherence length laser diode operating below threshold was used as the light source to give an axial resolution of 10 µm.

Optical Coherence Tomography itself was first described in a 1991 paper in the Journal *Science* [7]. The paper describes taking the idea of producing depth profiles from a layered sample from the OCDR technique and extending it to produce two-dimensional

cross-sectional images in biological tissue. As in OCDR, the depth profile produced from the interference signal is recorded at a sample site. The imaging beam is then moved to an adjacent sample site and the depth profile recorded again. In this way by sequentially depth scanning and then moving the imaging location, a 2D image can be constructed, as shown in Figure 2.3.

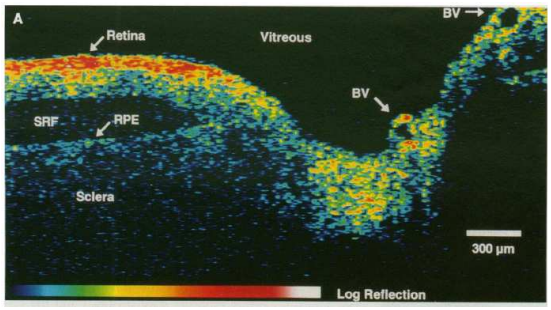

Figure 2.3. First reported OCT image of the human retina (*in vitro*). Taken from [7].

Figure 2.3 (on the previous page) shows one of the first reported OCT images of the human retina, *in vitro*. The system used to produce the image consisted of an 830 nm superluminescent diode (SLD) coupled into a fibre-optic Michelson interferometer. The reference arm scanning was performed by a mirror controlled by a stepper motor. The axial resolution of the system is claimed as 17 µm in air, while the lateral resolution, limited only by focusing optics and lateral positioning, is claimed as 9 µm. It should be noted that the parts of the human eye imaged are mostly transparent when compared with other bodily tissues. This made them ideal candidates in early OCT imaging [8] (and earlier, similar work [9]), since specular reflections will be visible, even with low input optical power, due to low bulk tissue scattering.

These first descriptions of the OCT technique set most of the standards and components for subsequent development. The use of SLD light sources, fibre-optic components for interferometer construction, and simple mechanical reference arm scanning devices form the basis of most early OCT development systems. Before considering the theory and development of the various system components, some discussion of the limitations inherent to OCT is needed.

2.4 Optical loss and sources of noise in OCT

The techniques of interferometry are at the heart of all OCT systems. As previously described, the basic idea of splitting an optical input into two beams, directing them towards a sample and a reference reflector, and then recombining to produce a path-length-dependent interference signal, is fundamental. Unfortunately this process has inherent losses associated with it, with much of the input optical power being wasted. These various loss processes, together with the effects of sources of noise, explain why OCT imaging is limited in all but the most transparent of samples.

Again if the Michelson interferometer is considered, the loss mechanisms can be described, as seen in Figure 2.4.

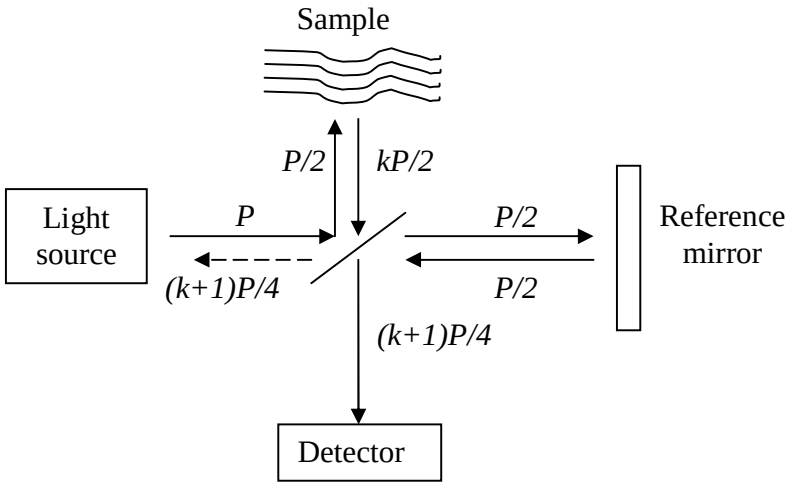

Figure 2.4. Schematic of a Michelson interferometer, showing the power loss pathway.

Figure 2.4 shows a light source inputting an optical power, *P*, to a Michelson interferometer. As usual, this is split into two arms of equal power (a 50:50 split ratio), *P/2*. One arm is incident upon a reference mirror and returned to the beam splitter; this can be considered as an almost lossless process since mirrors of very high reflectivity (>99.9%) are routinely available. The other arm is directed towards a sample, with reflections and back-scattering occurring at various locations into the sample. A large

portion of the light incident upon the sample will be lost due to processes such as absorption and multiple scattering. These are discussed later in this chapter. For simplicity, the power, *P/2*, incident on the sample can be said to be reduced by a factor, *k*, whose value lies somewhere between zero and one. The power returning from the sample is therefore *kP/2*.

Light returning from the two arms of the interferometer interferes at the beamsplitter, but at the same time both returning beams are split in the same 50:50 ratio, as before. Half of the returning optical power from each arm ends up being directed back towards the light source, where it is lost. The power directed towards the detector has contributions *P/4* from the reference arm and *kP/4* from the sample arm, giving a total of *(k+1)P/4*. This is the same as the amount lost towards the light source. The same amount, *(k+1)P/4*, is lost by being sent back toward the light source.

Since typically less than 1% of the optical power directed at scattering samples is returned, the sample loss factor, *k*, is usually close to zero. This results in the power directed towards the detector, *(k+1)P/4*, tending towards *P/4* as the sample loss factor, *k*, approaches zero. The result of this is that almost 75% of the input optical power is not detected in the typical Michelson interferometer [10].

It seems, therefore that there are two major sources of optical loss in a basic OCT system: losses in the sample under test, and losses due to the interferometer design effectively "throwing away" some part of the incident optical power.

2.4.1 Light scattering in tissue

In the previous considerations of the OCT imaging process the sample under test has always been considered to behave like a perfect mirror or series of mirrors. This allows certain assumptions about the nature of the light returning from the sample to be made. These assumptions include the preservation of coherence within the imaging beam, and knowledge of the optical power available for imaging at different depths. In relatively

transparent tissues the simple idea that light propagating through the tissue undergoes only a time delay, and weakly reflects from the layers within the sample is a reasonable description [11]. For strongly-scattering samples other effects have to be considered.

Most tissues consist of a range of materials such as collagen and elastin, along with structures such as blood vessels and various cells. These can have sizes in ranges from the nanometre-scale to the millimetre-scale and are arranged in a disordered, inhomogeneous fashion. This range of sizes and material types can cause light incident upon the tissue to scatter in several ways, and at various angles, dependent upon the particular scattering structure in question [12]. Figure 2.5 shows the nature of several different scattering interactions that can occur in dense tissues.

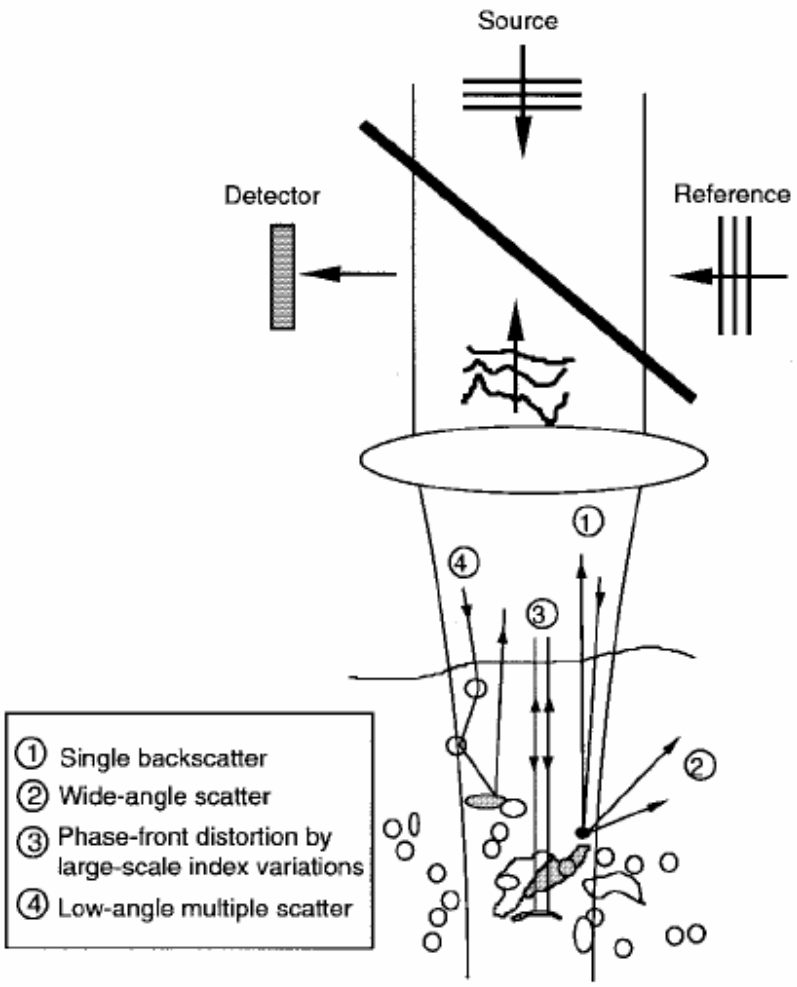

Figure 2.5. Types of scattering interaction in dense tissue. Modified from [13].

Figure 2.5 details 4 distinct types of interaction for light within a scattering tissue sample. The event labelled “1” describes the simplest interaction whereby light experiences a single backscattering event when incident upon some structure within the tissue. This event type results in no change to the coherence of the light and can be considered in the same way as if the light were incident upon a mirror. The wide-angle scatter event, labelled “2” in Figure 2.5, results in the light involved being lost from the system completely. The interactions labelled “3” and “4” have a more subtle effect on the imaging process. Phase-front distortion (“3”) is induced in light that passes through a sample region with a different refractive index. This causes a change in the propagation delay, resulting in sample features appearing at incorrect depth locations within an image.

Low-angle multiple scatters (“4”) occur when light is forward scattered after an interaction, allowing it to undergo further scattering events. Each scattering event causes the light to follow a disjointed path. If the light is eventually backscattered and exits the sample it will have travelled a significantly longer path than if it had undergone a single back scattering event. This results in a gradual loss of coherence, and degrades image quality. The scenarios “3” and “4” in Figure 2.5 are important in explaining some of the sources of noise in OCT images. The photons of light involved are not lost from the imaging system, but the temporal and coherence properties are disturbed, preventing them from contributing to the image information content.

2.4.2 Noise in OCT imaging

So far, it has been shown that basic OCT imaging is very wasteful in terms of the ratio of optical power input to useful optical signal output. Light is lost to various scattering processes within the sample under test, and some of the light that is not lost adds only noise to the output.

Once the optical signal is incident upon a photodetector, the description of noise on the signal can be split into 3 broad groups. These are relative intensity noise, thermal noise, and shot noise [5]. OCT uses the principle of heterodyne detection; that is the mixing of a signal with a reference oscillator producing a “beat” frequency component whose amplitude is proportional to that of the signal. Heterodyne detection allows high detection sensitivity, approaching the shot-noise limit. Shot noise is related to the random nature of the photon absorption/electron emission process within a photodetector. The average rate of electron emission defines the photocurrent, and this scales as the square of the incident optical power. Since incident light arrives in discrete quanta (photons), and the electron emission occurs at some random time following this, the photocurrent will have some natural variability in time known as shot noise. The shot noise power, N_{shot}, is proportional to the elemental charge, e, and the square root of the photocurrent power, $<i>^2$, as shown in equation 2.15.

$$N_{shot} \propto e\sqrt{\langle i \rangle^2} \qquad (2.15).$$

Relative intensity noise, N_{RIN}, is produced by fluctuations in light source output power or by changes in optical power induced by other components in the system. It is proportional to the average photocurrent power, $<i>^2$, and the elemental charge, e, multiplied by some experimentally-determined noise factor, f, as shown in Equation 2.16.

$$N_{RIN} \propto fe\langle i \rangle^2 \qquad (2.16).$$

Thermal noise is simply related to the exchange of energy with the surrounding environment at some temperature, T. This occurs only in resistive elements in all electronic circuits. In OCT systems this is added to the signal when it undergoes amplification. The thermal noise, N_{therm}, is related to the temperature, Boltzmann's constant, k, and resistance, R, as shown in Equation 2.17.

$$N_{therm} = 2kTR \qquad (2.17).$$

The 3 noise components discussed above can be added together and re-written in terms of an output voltage, V, to give Equation 2.18.

$$N_{sum} = eVR + efV^2 + 2kTR \qquad (2.18).$$

In Equation 2.18 $V=<i>R$, where R is the value of the gain resistor in the amplifier; while the experimentally-determined noise factor, f, has units of $(\text{amperes})^{-1}$, i.e. the reciprocal of current.

It can be shown that, by combining the photocurrent components from noise sources with those from the useful signal, the shot-noise-limited, signal-to-noise ratio (SNR) can be written as:

$$SNR = \frac{\eta}{h\upsilon}\left(\frac{Power_{sample}}{2NEB}\right) \qquad (2.19).$$

In Equation 2.19 hv is the photon energy, η is the detector quantum efficiency, and NEB is the noise-equivalent bandwidth [5].

In order to ensure that the detection is shot noise limited, the shot noise must dominate over the other noise components. So, considering just the thermal noise from Equation 2.18:

$$\begin{aligned} eVR &> 2kTR \\ V &> \frac{2kT}{e} \end{aligned} \qquad (2.20).$$

Equation 2.20 sets a minimum voltage, produced by the reference arm optical power, needed to reach the shot noise limit. This is approximately 50mV for a temperature of 300K. This means that providing the DC output produced from the reference arm is greater than 50mV, the shot noise will dominate over the thermal noise. If the relative intensity noise is now considered in a similar way:

$$\begin{aligned} eVR &> efV^2 \\ R &> fV \end{aligned} \qquad (2.21).$$

Equation 2.21 sets a condition on the value of the gain resistor, R, in the amplifier needed to produce shot-noise limited performance. In real-world systems the value of R is set for other reasons, so the reference arm voltage, V, is usually tuned (attenuated) to produce the best possible performance.

A full, in-depth discussion of noise and noise-limited performance in OCT systems is available in Chapter 2 of reference [5].

2.5 Fourier-domain OCT versus time-domain OCT

2.5.1 Time-domain OCT

So far, the theoretical systems considered for OCT imaging have all been what are known as “time-domain” OCT (TD-OCT) systems. This relates to the way in which a depth profile, or “A-scan” is obtained from a sample. The name “A-scan” is derived from Amplitude scan - a term used in ultrasound imaging to denote depth measurements taken at a single surface location. In a TD-OCT system, similar to the schematic depicted previously in Figure 2.2, the scattering/reflecting layers cause an interference signal to be produced only when the reference arm path length is equal to the path length to the relevant layer. Although the light source is illuminating the whole depth of the sample at all times, only a small portion of it is being used at any one time. As the reference mirror is moved, causing the path length to be scanned, the interferometric depth profile appears at the detector output as a function of time. This type of system has been investigated extensively [12], [14], and used to study tissues ranging from the human eye [15], to bovine arteries [16]. There have been many methods developed for scanning through the reference path length, and these are discussed later in this chapter.

2.5.2 Fourier-domain OCT

An alternative method of measuring the backscatter signal from a sample is known as Fourier-domain OCT (FD-OCT). As shown previously in section 2.2.2, the auto correlation function and the light source power spectrum form a Fourier pair. It is possible to extract the sample depth profile by simply measuring the spectral output from the interferometer, without needing any depth scan in the reference arm.

There are several different implementations of FD-OCT, including “Spectral Radar”, and “Swept-source OCT (SS-OCT)”. The common element between these methods is that a sample is illuminated with broadband light, and then the resulting interference signal is

captured as a function of wavelength. The captured signal is then Fourier-transformed to give the sample depth profile. A schematic diagram of a “Spectral Radar” system is shown in Figure 2.6.

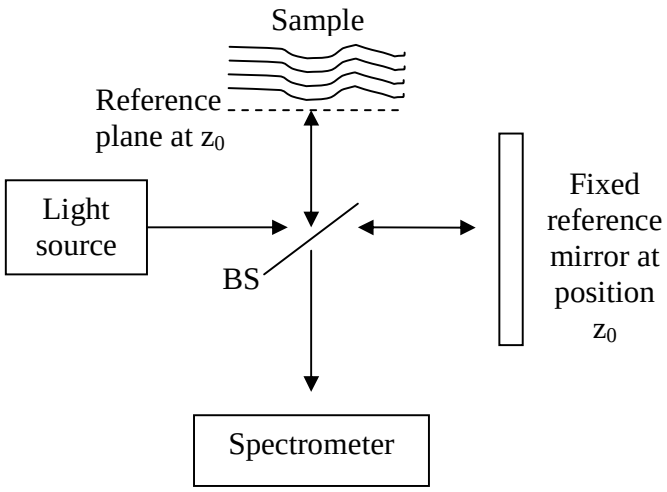

Figure 2.6. Schematic diagram of a "Spectral Radar" FD-OCT system.

The schematic diagram in Figure 2.6 shows a typical Michelson interferometer being illuminated with a broadband light source. One arm of the interferometer is directed towards a sample, while the other is terminated with a fixed retro-reflecting mirror. The light from the two arms re-combines at the beam splitter (BS in Figure 2.6) before entering a spectrometer. The spectrometer essentially consists of a dispersive element, such as a prism or diffraction grating, followed by a detector or array of detectors. This produces an interference signal as a function of wavelength, λ, or wavenumber, $k(=2\pi/\lambda)$. This interference signal, $I(k)$, is made up of 3 terms [5], as shown in Equation 2.22.

$$I(k) = S(k)\left(1 + \int_{-\infty}^{\infty} a(z)\cos(2knz)dz + AC\right) \qquad (2.22)$$

In Equation 2.22 $S(k)$ is the source spectrum, n is the refractive index of the sample, while $a(z)$ is the amplitude of each wavelength component as a function of depth (z). There are three components to the interference signal produced from a “Spectral Radar” system: a constant offset, an integral term incorporating the depth, z, of a scattering site

encoded as the frequency of the cosine, *2nz*, and an autocorrelation (AC) term related to interference of all wavelength components. It is straightforward to see that a Fourier transform of the interference signal, *I(k)* will give *a(z)*, the sample depth profile.

As mentioned, another type of FD-OCT system is known as Swept-Source OCT (SS-OCT). In this configuration a specific type of light source, known as a swept-source laser is used; the output of this repeatedly scans back and forth through a range of wavelengths as a function of time. This provides a spectrally varying *input* to the OCT system, removing the need for dispersive elements in the output stage. A single photodetector can be used to record the interference signal, which can then be Fourier-transformed to produce the sample depth profile. A complete depth profile can be recorded every time the swept source completes one scan through the full spectral range. Sweeping rates of tens of kilohertz are routinely available [17], while systems with rates of 370 kHz have been produced [18]. An SS-OCT system is further discussed and used in Chapters 5, 6 and 7.

2.5.3 FD-OCT versus TD-OCT: a comparison

Although both TD-OCT and FD-OCT methods have been successfully used to produce images in scattering media, there are pros and cons to both methods depending on the particular imaging situation.

Firstly, consider how efficiently light incident upon a sample is used in the two competing methodologies. In both situations the entire depth of the sample is illuminated during the imaging time. However, in TD-OCT only a small fraction of the light returning from the sample is used to produce the interference signal. Light returning from scattering events at depths other than those that are path length-matched with the position of the reference mirror is ignored, and does not contribute to the interference signal. In FD-OCT systems light returning from all depths within a sample is captured at the same time. This results in FD-OCT having a greater dynamic range than TD-OCT; that is, a larger ratio of the maximum to minimum power measurable by the system. The dynamic

range improvement available in going from TD-OCT to FD-OCT is a product of the shot-noise limited detection used. The greater number of photons available during the detection time in FD-OCT results in increases in dynamic range of 20 – 30 dB [19] theoretically, and at least 14 dB in real systems [5]. The signal-to-noise ratio (SNR) is also improved, by "several hundredfold" [20].

A second advantage that FD-OCT has over TD-OCT is the ability to compensate for an irregularly-shaped light source spectrum. In all of the previous considerations, the source spectrum has been assumed to be Gaussian in shape, since this shape produces an interference envelope of minimum width. In real-world systems it is difficult to produce sources with perfect Gaussian characteristics; using sources with non-smooth spectra produces side lobes and broadening of the auto correlation function. This results in an overall reduction in system resolution. In FD-OCT the source spectrum can be recorded as a reference, and then the interference photocurrent, $I(k)$, can be divided by the spectrum, $S(k)$.

Disadvantages of FD-OCT include increased sample vibration sensitivity and technical difficulties/costs associated with constructing suitable spectrometers. Photo-diode arrays, particularly devices made from materials other than silicon, are extremely expensive. This can limit the use of the "Spectral Radar" FD-OCT technique to wavelengths less than 1100 nm, where silicon detectors are most sensitive.

2.5.4 Calculating "Spectral Radar" depth range

In TD-OCT systems the imaging depth within a sample is limited by the scattering nature of the sample and also the range of motion available in the reference arm. The range in "Spectral Radar" systems is limited again by the sample scattering properties, but now also the resolution of the spectrometer used [21]. The interference signal consists of cosine fringes, with the highest frequency components coming from the deepest region of the sample. At the maximum depth, the sample frequency of the detector and electronics

must be at least twice that of the cosine fringes. Referring back to Figure 2.6 it can be shown that the depth scan range, Δz, measured from the reference plane at position z_0, is:

$$\Delta z = \frac{1}{4n}\left(\frac{\lambda^2}{\Delta\lambda}\right) \qquad (2.23).$$

In Equation 2.23 (taken from Chapter 12 of reference [5]) the terms λ^2 and $\Delta\lambda$ are the incident wavelength and spectrometer resolution (bandwidth), respectively, while n is the refractive index of the sample. Typical values for Δz, are of the order of a few millimetres.

2.6 OCT system design considerations

When designing an OCT imaging system it is essential to consider all the various aspects of the system in order to achieve the desired imaging capabilities. For example, if imaging static samples, slow reference arm scanning, low incident optical powers and relatively long exposure times may be all that is required to achieve satisfactory images. However, if the samples to be imaged are subject to movement artefacts (e.g. *in vivo* tissue), faster imaging and higher optical powers may be required.

2.6.1 Reference arm scanning methods in TD-OCT

TD-OCT is more widely used than FD-OCT [22] due to its relative simplicity, although it is not capable of reaching the high depth scan rates achieved by FD-OCT. For most practical applications a superluminescent diode, coupled into a Michelson interferometer with some form of direct, mechanical path length scanning in the reference arm, is all that is required. There have been many different methods of reference arm scanning utilised for TD-OCT. These all work on the principle of repeatedly and reproducibly adjusting the optical path length in the reference arm.

A commonly used method for optical path length scanning is a motorized, stage-mounted mirror as discussed previously (e.g. [7]). These tend to be extremely slow at scanning, capable of a maximum rate of perhaps 100 depth scans per second. A second commonly-used reference arm scanning technique involves a piezo-electric devices that stretch optical fibres in the reference arm [23], causing changes in the refractive index and therefore the light travel time. The inherent problem with this method, however, is that the stresses imposed on the fibre can induce undesirable birefringence and polarization-altering effects [24], although it is capable of several hundred depth scans per second. Fourier Domain "Rapid Scanning Optical Delay" (RSOD) lines (e.g. [25]), that use a rotationally scanning galvanometer together with a diffraction grating to induce a phase ramp in the frequency domain, resulting in a group delay in the time domain, are a third common method. These have the advantage over the other types in terms of speed, since, generally speaking, rotational motion can be modulated at much higher frequencies than linear motion. Depth scan rates of several tens of kilohertz are easily attainable. This last technique for reference arm scanning is discussed in more detail in Chapter 3.

An important consideration in all depth scanning systems used for imaging is the duty cycle. This is the portion of the scan that has a high enough linearity to produce equally spaced pixels in depth. Techniques where the mechanical motion is sinusoidal often have low duty cycles, since more dwell time is spent at the extremes of the scan than at the centre.

2.6.2 Light sources

There are many different types of light source that can be used in OCT imaging. In order to choose a light source for an OCT application there are three parameters that need to be investigated to confirm that a particular source is suitable; central wavelength, bandwidth and output power.

The central wavelength is chosen based on the properties of the sample or item to be imaged. For example, in human skin imaging 1300 nm is the preferred wavelength to use since the tissue has an absorption minimum around this wavelength.

References

[1] T. H. Maiman, *Nature* **187** (4736), 493 (1960).

[2] E. Hecht and A. Zajac, *Optics*, 1 ed. (Addison-Wesley Publishing Co., 1974).

[3] J. G. Fujimoto, *Proceedings of SPIE--the international society for optical engineering* **3749**, 402 (1999).

[4] M. K. Barnoski and S. M. Jensen, *Applied Optics* **15** (9), 2112 (1976).

[5] B.E. Bouma and G.J. Tearney eds., *Handbook of Optical Coherence Tomography*, 1 ed. (Marcel Dekker, Inc., 2002).

[6] K. Takada, I. Yokohama, K. Chida et al., *Applied optics* **26** (9), 1603 (1987).

[7] D. Huang, E.A. Swanson, C.P. Lin et al., *Science* **254** (5035), 1178 (1991).

[8] E. A. Swanson, J. A. Izatt, M. R. Hee et al., *Optics Letters* **18** (21), 1864 (1993).

[9] A. F. Fercher, K. Mengedoht, and W. Werner, *Optics Letters* **13** (3), 186 (1988).

[10] A. M. Rollins and J. A. Izatt, *Optics Letters* **24** (21), 1484 (1999).

[11] Yingtian Pan, Reginald Birngruber, Jürgen Rosperich et al., *Appl. Opt.* **34** (28), 6564 (1995).

[12] J. M. Schmitt, A. Knuttel, M. Yadlowsky et al., *Physics in Medicine and Biology* **39** (10), 1705 (1994).

[13] J. M. Schmitt, *IEEE Journal of Selected Topics in Quantum Electronics* **5** (4), 1205 (1999).

[14] E. Lankenau, J. Welzel, R. Birngruber et al., San Jose, CA, USA, 1997 (unpublished).

[15] A. F. Fercher, C. K. Hitzenberger, G. Kamp et al., *Optics Communications* **117**, 43 (1995).

[16] X. Clivaz, F. Marquis-Weible, R. P. Salathe et al., *Optics Letters* **17** (1), 4 (1992).

[17] R. Huber, M. Wojtkowski, J. G. Fujimoto et al., *Optics Express* **13** (26) (2005).

[18] Robert Huber, Desmond C. Adler, and James G. Fujimoto, *Opt. Lett.* **31** (20), 2975 (2006).

[19] M. A. Choma, M. V. Sarunic, C. Yang et al., *Optics Express* **11** (18), 2183 (2003).

[20] J. F. de Boer, B. Cense, B. H. Park et al., *Optics Letters* **28** (21), 2067 (2003).

[21] Michael A. Bail, Gerd Haeusler, Juergen M. Herrmann et al., *Photon Propagation in Tissues II* **2925**, 298 (1996).

[22] P. H. Tomlins and R. K. Wang, *Journal of Physics D (Applied Physics)* **38** (15), 2519 (2005).

[23] Y. Takahashi, M. Iwaya, Y. Watanabe et al., *Japanese Journal of Applied Physics* **45** (10A), 7975 (2006).

[24] G.J. Tearney, B.E. Bouma, S. A. Boppart et al., *Optics Letters* **21** (17), 1408 (1996).

[25] G. Song and S.L. Jacques, *Proceedings of SPIE--the international society for optical engineering* **4916**, 259 (2002).

Chapter 3

An OCT system for skin imaging

3.1 Introduction

This chapter firstly discusses a basic system that was configured in order to test components and make initial measurements. This was then converted into the final system that will be used to image skin. The basic system is described and then the differences between the basic and final version of the systems are discussed. The goal for the final system is for it to be capable of imaging both structural and Doppler information in vivo.

The initial work involves the testing of various system components including the building of an optical fibre-based interferometer, and characterisation of a superluminescent diode (SLD) light source. The autocorrelation of the light source was measured and the coherence length calculated from the FWHM of the autocorrelation envelope function. Also, the output spectrum of the source was measured using a scanning spectrometer, allowing the coherence length to be measured using a second method. The source stability was then tested by measuring output power and spectra over long time periods, and under varying drive current conditions.

The system was then modified from the "test" version into the more complete final version. The interferometer used is fibre-based and is of a modified Mach-Zehnder configuration, incorporating optical circulators and unequal splitting ratios to maximise the amount of light delivered to the sample. The reference arm consists of a rapid scanning optical delay (RSOD) line, utilising a resonantly scanning, galvanometer-mounted mirror and a diffraction grating to produce path length variation. This

configuration allows dispersion to be independently compensated for, as well as allowing some control of the frequency and bandwidth of the OCT signal. The galvanometer scans at approximately 8 kHz, allowing 16,000 A-scans per second to be measured if bi-directional scanning is used. A dual-balanced photodetector pair is used at the output of the interferometer to record the interference signal.

The sample arm is coupled into a hand-held probe which contains a fibre collimator, 2-axis lateral scanning galvanometers, and a final focusing lens. The path lengths in the two arms of the interferometer are matched at the lens focus by means of adjustable components in the RSOD.

The RSOD galvanometer and associated electronics produce synchronization and clock signals for use with data acquisition (DAQ) devices. There are 512 clock pulses provided for every depth scan, with the frequency of these varying to account for the sinusoidal nature of the scanning motion. A National Instruments DAQ, programmed using LabVIEW software, uses the synchronization signal (~8kHz) to produce a voltage ramp to drive the lateral-scanning galvanometers in order to produce 2-dimensional images. The LabVIEW software also produces a frame synchronization signal every 256 depth scans (~30 Hz), which is used to trigger a high-speed, 16-bit Alazartech DAQ. This device actually captures the image data, and is programmed using custom software written in Visual Basic. A custom power supply and control unit were also constructed to provide all components with power, and to control the scanning amplitude of the resonant galvanometer.

Other components tested include: a fibre-based Wavelength Division Multiplexer, which allows a visible beam to be injected into the sample arm for aiming; and an electro-optic modulator (EOM) which will be used in future to capture Doppler OCT data from the interference signal.

Initial images have been produced “on the bench” using the system and these are presented.

3.2 Basic system overview

Before constructing an OCT system for medical imaging, some understanding of the limitations and design issues associated with the various components involved is necessary. To this end a basic "pre-prototype" TD-OCT setup was designed and constructed for testing purposes. It should be noted that some of the components (SLD, detectors, beam splitters, etc.) used in this pre-prototype system will be re-used in the construction of the final prototype system.

3.2.1 Optimized Mach-Zehnder interferometer

Although many OCT systems use a Michelson interferometer due to its simplicity, improvements in signal-to-noise ratio can be gained by using other optimized designs. The system used here is based around a Mach-Zehnder interferometer design described by Rollins and Izatt [1]; seen here in Figure 3.1.

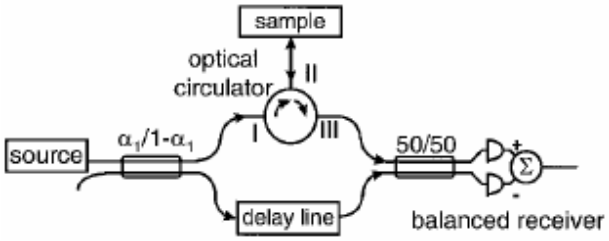

Figure 3.1. An optimized Mach-Zehnder interferometer design for OCT. The unequal splitting ratio at the first beamsplitter, along with dual, heterodyne detection, provide a boost in SNR of approximately 8dB compared with a basic Michelson system. Adapted from Figure 2 Ai in [1].

For calibration purposes the "sample" in Figure 3.1 was replaced with a back-reflecting mirror in order to maximize the return signal. The delay line in the reference arm was constructed exactly as the sample arm, using an optical circulator and mirror. The system is almost entirely fibre-based, except for a small section in each arm (e.g. the "sample"

end of leg II of the circulator), where the light from the fibre is collimated and directed towards a mirror. Since constructive interference only occurs when light traveling in both interferometer arms incurs the same time delay, this air gap proves to be useful in compensating for unequal lengths of fibre.

The mirrors in both "sample" and reference arms were mounted on 3-axis translation stages (Thorlabs Nanomax303). The stage in the reference arm is driven in the axial direction by a stepper motor, controlled using software written in LabVIEW (National Instruments). The stage has a total travel of 4 mm at a minimum speed of 0.04 mm/s (maximum speed 2 mm/s), allowing fine adjustments in path length over a range of 4 mm. The motor-controlled stage is mounted on top of a manual, single-axis translation stage (Edmund Optics P/N: 56-796) with 25 cm of travel, providing rough adjustments in path length.

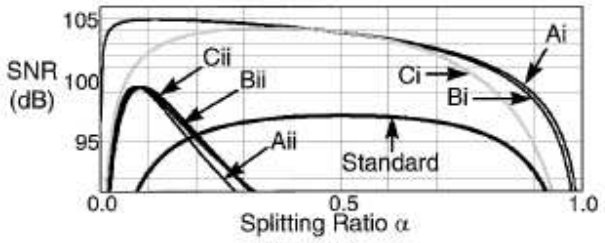

Figure 3.2. SNR as a function of splitting ratio α. The optimized Mach-Zehnder interferometer (curve Ai) has best performance when α=0.12. The improvement in SNR over the Michelson interferometer (curve labelled "Standard") can be seen. Adapted from Figure 3 in [1].

The two beam splitters are both fibre-based items (Newport F-CPL-F22131 and F-CPL-F22135). One has a balanced (50:50) splitting ratio, while the other is chosen with a ratio of 90:10. The 90:10 beam splitter has a splitting ratio of 0.1, the closest commercially available option to the optimum value of 0.12 [1]. The advantage of this set-up in terms of SNR can be clearly seen in Figure 3.2 (curve labelled "Ai").

Optical circulators are a relatively new family of optical components based on magneto-optic materials. The non-reciprocal nature of these materials can be used to produce

components that only transmit light in one direction [refB]. The two circulators used here are 3 port, fibre-connected items (Newport F-CIR-13-P-FA). Light is only transmitted in the direction of the arrows (See Figure 3.1), with light going from port 1 to 2, and then from port 2 to port 3.

3.2.2 The low coherence light source

There are many different possibilities when it comes to choosing a light source suitable for use in an OCT system. One of the most common and readily available options is the Super-Luminescent Diode (SLD). These can be obtained in a variety of bandwidth/centre wavelength combinations with reasonable output power. They also have approximately Gaussian spectra which minimizes ghost images caused by side lobes [2]. Superluminescence or Amplified Spontaneous Emission (ASE) is the optical amplification of spontaneous photons by stimulated emission within a gain medium.

The light source used here is a SLD (Covega 1104-1259) with a nominal centre wavelength of 1295 nm and a FWHM spectral width of 65 nm. The device is fibre-pigtailed, and mounted on a temperature-controlled heat sink to minimize output variations due to environmental changes. Using the above specifications (λ_0 = 1295 nm, $\Delta\lambda$ = 60 nm) in conjunction with Equation 2.14, it can be shown that,

$$\Delta d \approx 12\mu m \qquad (3.1)$$

i.e. the coherence length of this SLD is approximately 12 μm. In OCT systems, axial resolution is limited only by the coherence length of the light source and hence, the axial resolution of the system, in air at least, should be around 12 μm.

The SLD is supplied with a control unit allowing parameters such as the diode drive current and the temperature control window to be adjusted. The SLD can be driven in

either “constant current” or “constant power” mode. In the first case the drive current to the SLD remains constant, but the light intensity will fluctuate in response to temperature changes, etc. In constant power mode the optical power output remains constant but the drive current will vary to compensate for environmental changes [3].

3.2.3 The balanced photo-detector

In choosing the optimized Mach-Zehnder interferometer it is obvious that a dual balanced photo-detector is required for the system. Dual, balanced detection uses two photo-detectors to reduce noise in a system. The heterodyne outputs from the detectors are added together while excess photon noise can be largely removed. Such detectors are readily available commercially, although expensive at the near-infrared wavelengths used here.

The detector chosen for the system is the Thorlabs PDB120C-AC 75 MHz fixed-gain, balanced amplified photo-detector. This consists of two matched InGaAs photodiodes and a low noise, high speed amplifier. An output voltage is produced that is proportional to the difference between the currents induced in the photodiodes. The detector can be used in the wavelength range 800 to 1700 nm [4].

The output from the detector was connected to a PC for data recording via a LabVIEW interface and DAQ card.

3.3 Finding the zero point

With the system set up as described in Section 3.2, the next stage of the investigation was to find the zero point of the system. The zero point is simply the position to which the reference arm mirror must be moved in order to see constructive interference with light

from the mirror in the “sample” arm. At this point the optical path lengths in both arms of the interferometer are the same.

3.3.1 Measuring the interferometer arms

In order to find the zero point and see the auto-correlation function the interferometer arms need to be measured so that the approximate position for the reference mirror can be determined. This was done by measuring every length of fibre in each arm of the interferometer and summing the various lengths. The fact that some portions of the system are traveled twice by the light was also taken into account.

When the total length of each arm is known, the approximate zero point can be calculated as follows. The reference arm mirror is placed at such a position that the air gap between it and the end of the fibre compensates for the relative shortness of the reference arm fibres (the reference arm fibre components are chosen such that it is always shorter than the “sample” arm).

The air gap can be calculated by knowing the length difference between the two fibre arms, and compensating for the difference in refractive index between air and glass (fibre, n_{glass}=1.47). Using this method the calculated required spacing between mirror and collimator was 11.3 cm.

3.3.2 The zero point

The calculated spacing of ~11.3 cm between mirror and collimator was set using the manual single-axis stage; the motor driven stage is then used to fine-tune the positioning. The auto-correlation function at the zero point was then recorded. This was done by programming the motorized stage to repetitively travel back and forth using a software routine written in LabVIEW. The output from the detector pair was connected to an oscilloscope, with the trigger level set slightly above the noise level. As the mirror passes through the zero point, the spike in output voltage triggers the oscilloscope which records an image of the auto-correlation function. One such image can be seen in Figure 3.3.

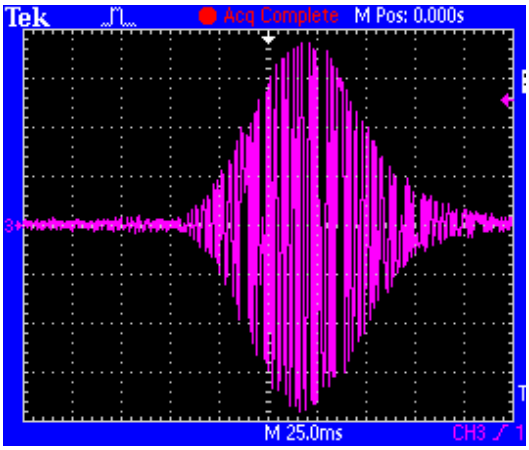

Figure 3.3. The auto-correlation function recorded with an oscilloscope. The vertical axis is voltage (1V per division) and the horizontal axis is time with each square representing 25 ms. The stage was moving at 0.2 mm/s to create this image.

The width of the pulse in Figure 3.3 is dependent on the speed at which the mirror travels through the zero point. The FWHM of the pulse is approximately 60 ms, when the stage is moving at a constant speed of 0.2 mm/s. Combining these two figures gives the width of the auto-correlation function and hence, the coherence length of the light source.
Here this was found to be (Equation 3.2):

$$l_c = vt_{FWHM}$$
$$l_c = 0.2\times10^{-3}\times60\times10^{-3}m \qquad (3.2)$$
$$l_c = 12\mu m$$

In Equation 3.2 v is the stage velocity and t_{FWHM} is the temporal FWHM of the pulse on the oscilloscope. This confirms the coherence length specification of the SLD, shown here to be 12 μm.

3.4 Characterizing the SLD using the auto-correlation function

The auto-correlation function visible at the zero point provides a method of measuring the coherence length of the SLD. The variability of the SLD output parameters under various control and environmental factors would be useful to quantify, in order that consistency be maintained when eventually using the system for imaging. To this end it was decided to use the auto-correlation function to monitor the effect that SLD drive current has on the coherence length, as well as monitoring the time stability of the coherence length under the influence of environmental temperature change.

3.4.1 Coherence length as a function of SLD drive current

In OCT, higher intensity light allows greater penetration into tissue and therefore reveals more detail and information from a sample. Higher output intensities are provided by driving the SLD with more current. It is useful to know how this affects the coherence length of the light, to ensure that axial resolution is not compromised.

As mentioned previously, the SLD is connected to a control unit that is used to set the drive current (in "constant current" mode), or the monitored output power (in "constant power" mode). The current can be set to any value between 0 and 500 mA.

The current was adjusted until just above the threshold value in constant current mode (approx. 80 mA). It was then increased in 10 mA steps up to 500 mA. At each stage the auto-correlation function was displayed and the FWHM (in time) was recorded. Post-processing converted these time measurements into coherence lengths, as previously demonstrated (see Equation 3.2). Figure 3.4 shows a plot of these results.

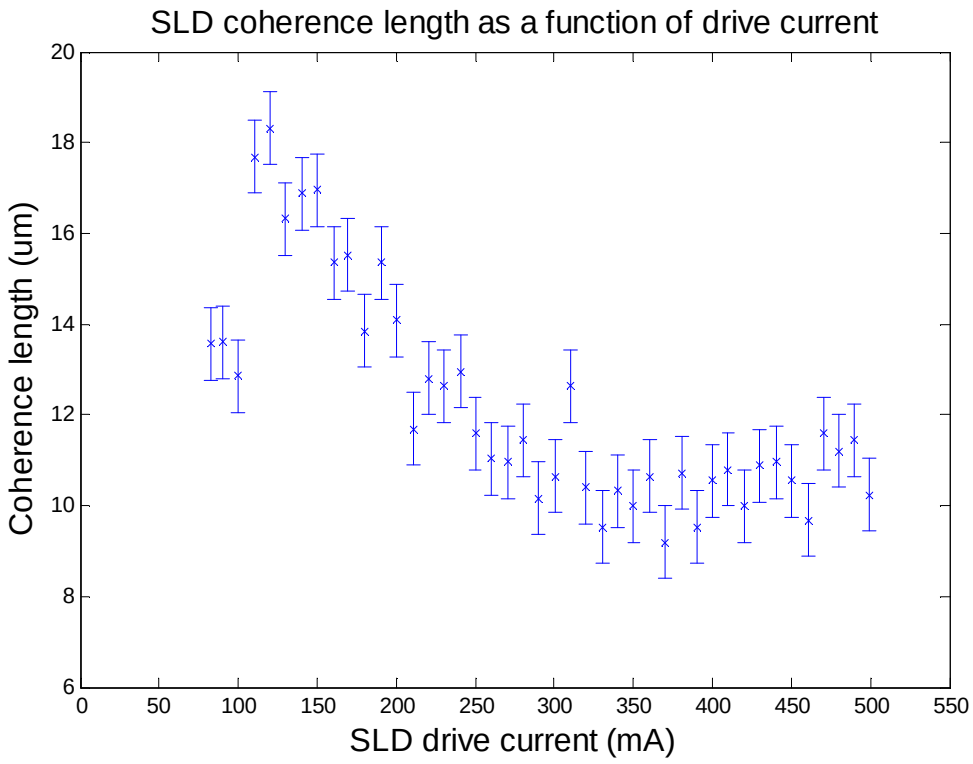

Figure 3.4. A graph of SLD coherence length as a function of diode drive current. Error bars (±0.8 μm) are estimated from the error in measuring the FWHM of the auto-correlation function using the oscilloscope.

The graph in Figure 3.4 shows that coherence length decreases fairly linearly from above threshold to around 250 or 300 mA. The coherence length then remains relatively unaffected by further increases in current, settling at between 10 and 12 μm. This is a positive result because the highest drive currents, and consequent high output powers,

give the shortest coherence length and hence the highest axial resolution. This means that high axial resolution and large penetration depths can be achieved together.

3.4.2 Time stability of SLD coherence length

The time stability of the SLD coherence length is important in producing consistent, reproducible images. For example, it is useful to know whether the SLD needs to be allowed to settle after switch on, or if it can be left on for long periods of time without significant instability occurring due to environmental changes, such as temperature.

The SLD drive current was fixed at a value of 450 mA. The coherence length was then determined from the auto-correlation function at varying intervals of approximately 30 seconds for 10 minutes. The same 10 minute process was then repeated 90 minutes later. The results are shown in Figure 3.5.

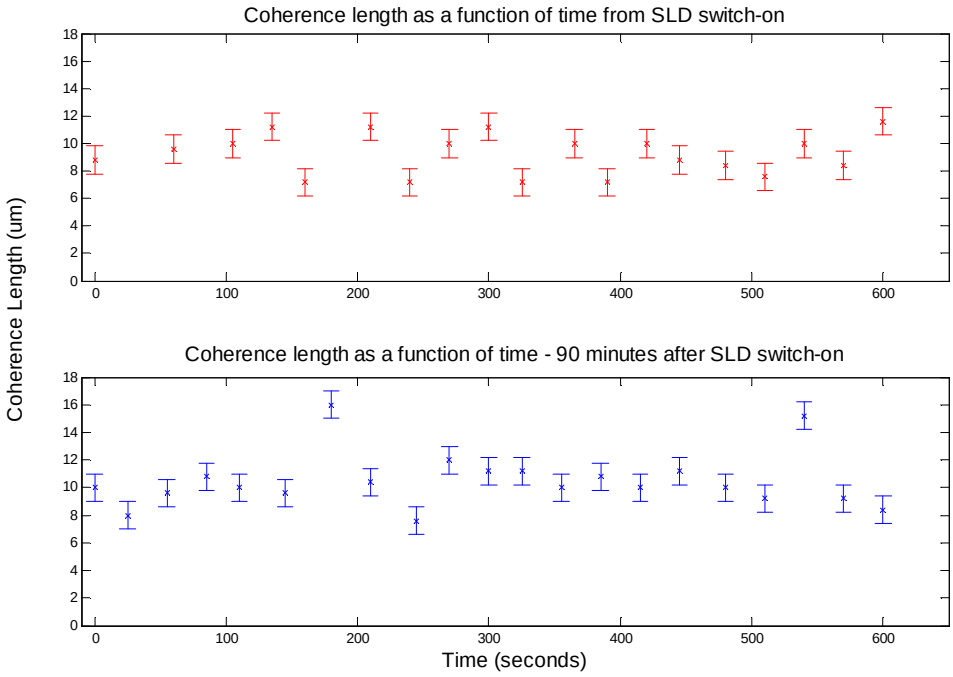

Figure 3.5. A Graph of SLD coherence length as a function of time after switch on. The upper plot (red) is the first 10 minutes after switch on while the lower (blue) is a 10 minute period, 90 minutes after switch on.

The results shown in Figure 3.5 show that the coherence length remains fairly constant over both short (first 10 minutes) and long (90 minutes from power up) time periods. The seemingly erroneous points in the lower plot (at approx. 200 seconds and 550 seconds) are due to incorrect triggering of the oscilloscope causing the auto correlation function to be incompletely recorded. A time-stable coherence length is a positive result as it means that an OCT system using this SLD can be used soon after switch on, and for long time periods, without fear of inconsistency caused by a wildly fluctuating coherence length.

3.4.3 Further SLD characterization using spectral analysis

In order to fully characterize the SLD it is necessary to analyse some other parameters of the output light. The SLD spectrum can reveal details about the bandwidth and peak wavelength of the output light, as well as accessing the overall spectral shape. It was decided to record how the spectrum of the SLD reacted to changes in diode drive current, as well as how it changed due to environmental factors over time.

Spectra were measured using a 0.5 m length grating spectrometer (Acton Research Spectra Pro 500i, 300 lines/mm, 1200 nm blaze) coupled to a high-speed, amplified InGaAs photodiode (Thorlabs PDA255). The output from the SLD was collimated and directed to the input slit of the spectrometer. The input and output slits were then optimized for resolution and sensitivity. Spectra were recorded by computer at 1 nm resolution in the range 1200 to 1400 nm. This width was deemed wide enough to encompass the entire spectrum from the SLD after a series of test runs.

3.4.4 Spectra vs. SLD drive current

Spectra were recorded as a function of SLD drive current, in 25 mA steps between 0 and 500 mA. The resulting plot is shown in Figure 3.6. The red line on the plot tracks the peak (centre) wavelength of each spectrum, showing a gradual decrease in centre wavelength as the current is increased, from above 1310 nm at low current down to 1295 nm at maximum current. This is in line with the manufacturers specifications for the SLD. It can also be seen from Figure 3.6 that the FWHM bandwidth of the spectral peak increases linearly with increasing drive current. The increase is expected but its linear nature is interesting to note. When using the SLD for imaging, it will be necessary to always work at a single drive current to make sure that bandwidth, and therefore system resolution, are constant.

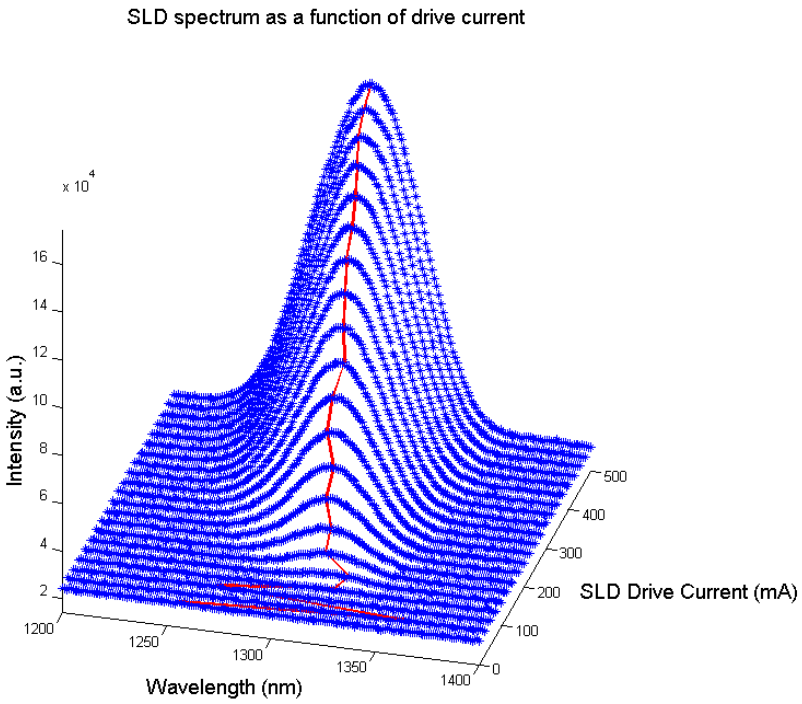

Figure 3.6. A 3-dimensional plot of SLD spectra (intensity vs. wavelength) against diode drive current. The red line connects the peak wavelength from each individual spectrum.

3.4.5 Spectral Time Stability

The time stability of the SLD can also be determined by observing its spectral output over time. Fluctuations in bandwidth or peak wavelength can be observed, along with any variations in intensity caused by environmental heating or cooling.

Spectra were recorded every 15 minutes for more than 12 hours. The resulting plot is shown in Figure 3.7. The spectra in Figure 3.7 are extremely stable over the long time period shown. No fluctuations in bandwidth or peak wavelength can be seen, although there are some small variations in intensity, probably caused by room temperature fluctuations.

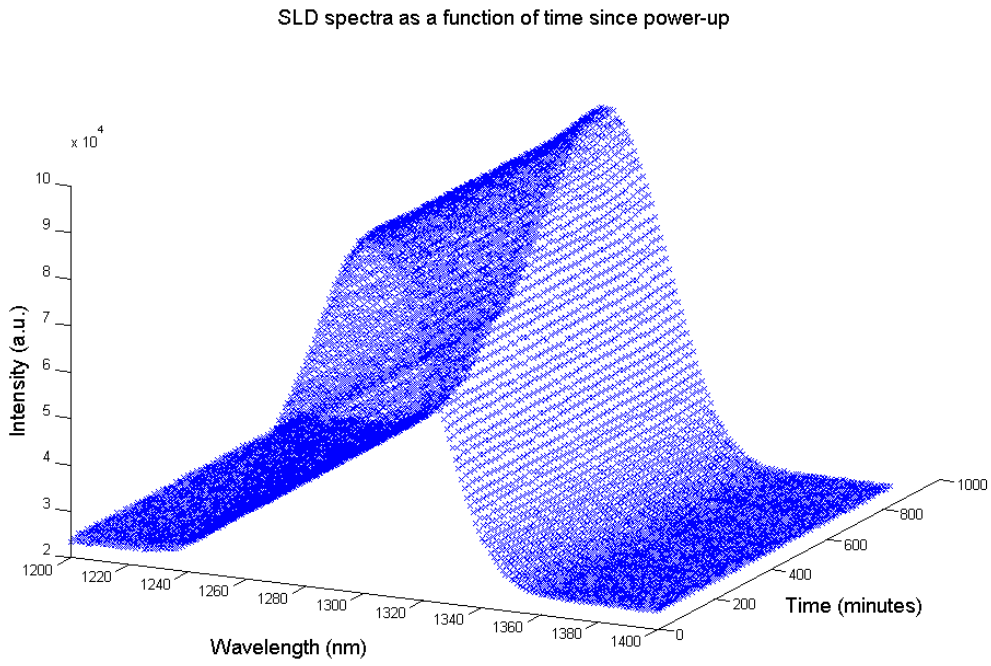

Figure 3.7. A 3-dimensional plot of SLD spectra (intensity vs. wavelength) as a function of time.

3.5 One-dimensional depth profiles

The next step to take, after studying the SLD, was to use the system to acquire some 1-dimensional depth profiles of simple optical systems. This can be said to be a "proof of concept" type experiment, in that it produces a cross-sectional image through a sample, albeit only in 1 dimension.

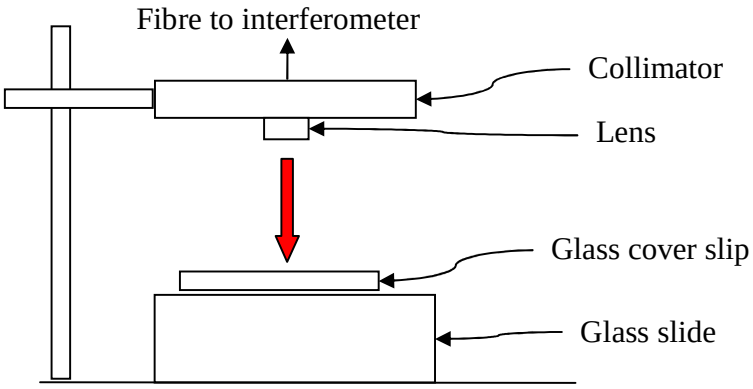

Figure 3.8. Diagram showing the experimental setup of the sample arm used for acquiring OCT depth profiles.

The sample arm of the Mach-Zehnder interferometer was assembled as shown in Figure 3.8. The sample used is simply a thin glass coverslip on top of a thicker glass slide. The idea is that this will present several interfaces of changing refractive index to the beam, with some light from each being reflected back to the interferometer to create interference. The reflection co-efficient of glass is approximately 4% so the signal levels encountered will be much smaller than for the mirrors used previously.

The method of recording an image is very similar to the way in which the auto-correlation function was recorded previously. The motorized stage in the reference arm is set in motion, moving back and forth repetitively along its axis. As it passes through the point at which the optical path length in the reference arm is equal to the position of the first interface, the oscilloscope is triggered and records the signal. Setting the appropriate time period for the trigger allows the entire sequence of interfaces to be recorded.

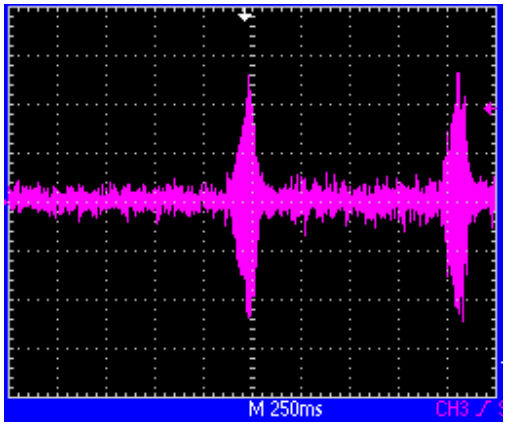

Figure 3.9. An oscilloscope image showing the interference pattern generated by reflections from the air/glass interfaces of a glass cover slip. The vertical axis is voltage (500 mV per division) and the horizontal axis is time (250 ms per division.) The translation stage was moving at 0.2 mm/s to generate this image.

Initially just the coverslip boundaries were recorded, an example image is shown in Figure 3.9. The time delay between the two peaks can be used to calculate the thickness of the coverslip. With the reference arm scanning at 0.2 mm/s, and accounting for the refractive index of glass (~1.47), the thickness of the coverslip is calculated to be approximately 140 μm.

With some tweaking of the alignment between the collimated beam and the glass surfaces it was possible to resolve the coverslip *and* the top surface of the glass slide. This is shown in Figure 3.10, overleaf.

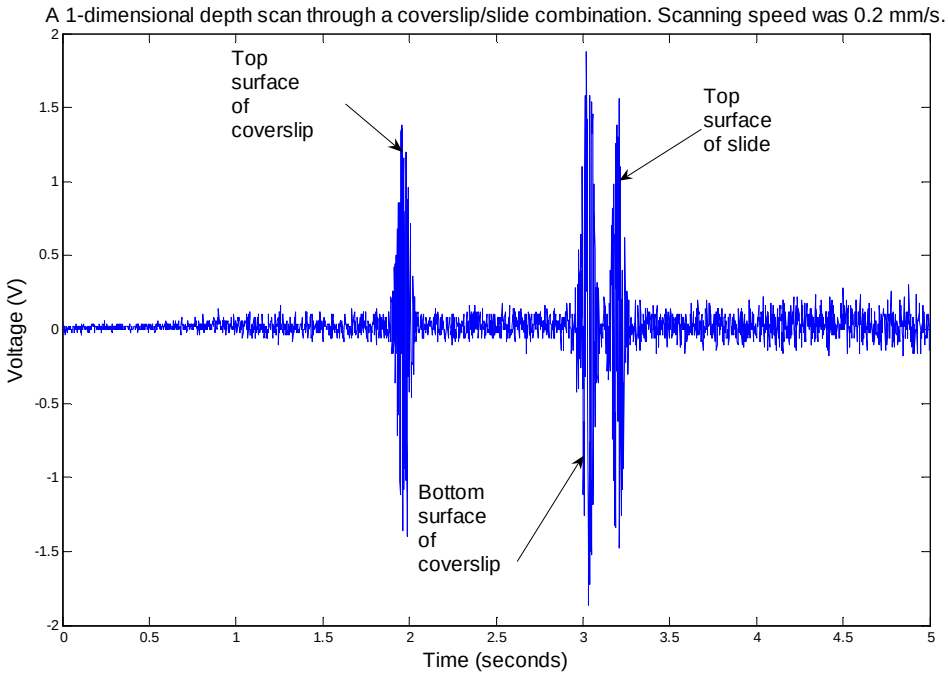

Figure 3.10. Graph showing the 1-dimensional depth scan of the coverslip/slide combination. The translation stage was again moving at 0.2 mm/s to acquire this image.

The thickness of the coverslip is again shown to be approximately 140±12 μm; this agrees well with the micrometer-measured value of 150 μm. The second, lower surface of the glass slide is not resolved here because the stage could not move into the region were it would be expected without alignment issues due to a mechanical problem with the motorized stage.

These various one-dimensional profiles demonstrate the proof-of-concept of OCT imaging systems.

3.6 Final system

The final system design builds on the test system used in characterising the SLD and the other components. It uses the same Mach-Zehnder interferometer design, and the same SLD light source. It differs primarily in the ability to produce two-dimensional images at a fast rate, whereas before data collection was slow and only one-dimensional. This is achieved by replacing the linear motorized scanner in the reference arm with a grating-based Rapid Scanning Optical Delay (RSOD) line. Figure 3.11 overleaf shows the final system design in schematic form.

The subsequent sections will then describe in some detail each component or sub-system and the reasons that particular design choices were made.

Figure 3.11 details the interferometer and RSOD design, as well as showing how the optical system interfaces to the electronic and software systems via the use of various logic and timing signals.

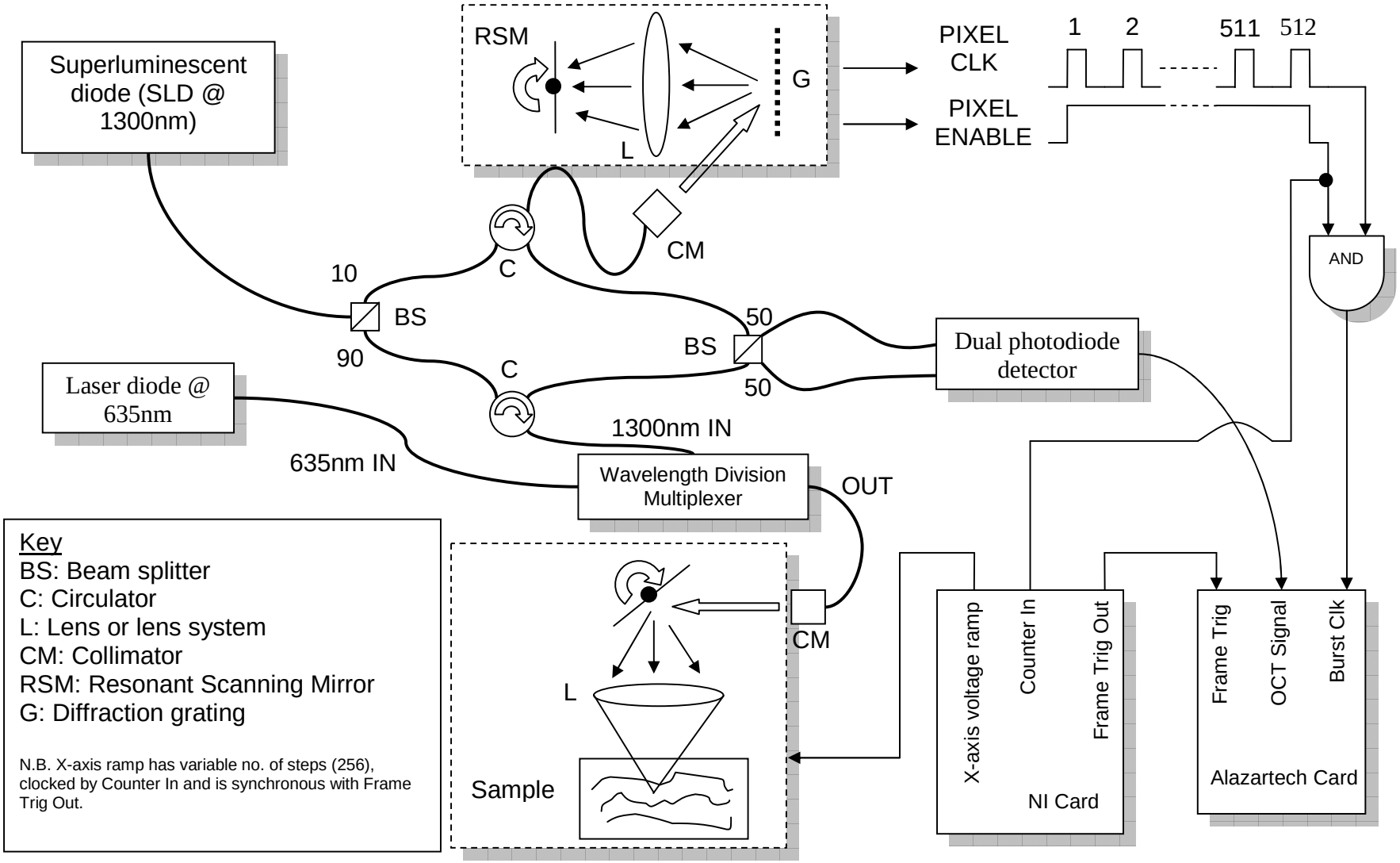

Figure 3.11. OCT system diagram showing optical and digital connections. Excluded items include: PSU/amplitude controller for RSM, EOM for Doppler OCT, and miscellaneous electronics. Thicker lines denote optical fibre connections.

3.6.1 Light source

The light source to be used in the final system is the same as used during the testing phase. The only addition to this part of the system is a Wavelength Division Multiplexer (WDM) allowing a visible laser diode to be injected into the system alongside the main (IR) imaging beam. The WDM was designed for use at 1300 nm and 630 nm; this latter wavelength would provide a red aiming beam so that the system operator could determine precisely where on a sample the image was being recorded. Unfortunately, following extensive testing, the WDM had to be removed from the system as it was discovered to be a major source of optical power loss for the 1300 nm source.

As shown in Figure 3.12, the WDM is positioned in the sample arm following the circulator. It can only be used in this position since the circulators do not transmit any light below 1150 nm. However, this positioning results in light returning from the sample having to pass through the WDM a second time; resulting in major losses due to lack of bi-directional coupling. On removal, the WDM was replaced by a length of optical fibre of the same path length.

3.6.2 Fibres

The optical fibre components used in the final system are generally the same as those used in the testing system. They all use SMF-28 type optical fibre, which is particularly suited for use at wavelengths around 1300 nm. This fibre type has a core diameter of approximately 9 µm and a cladding diameter of 125 µm.

It should be noted that the interferometer uses a fibre beamsplitter with an unequal 90:10 splitting ratio. The 90% portion is directed toward the sample in order to maximize any possible back-scattered signal that may be present.

3.6.3 Rapid scanning optical delay line

The major modification of the basic system was the replacement of the linear scanning mechanism in the reference arm, with a Rapid Scanning Optical Delay (RSOD) line to ensure high frame rates.

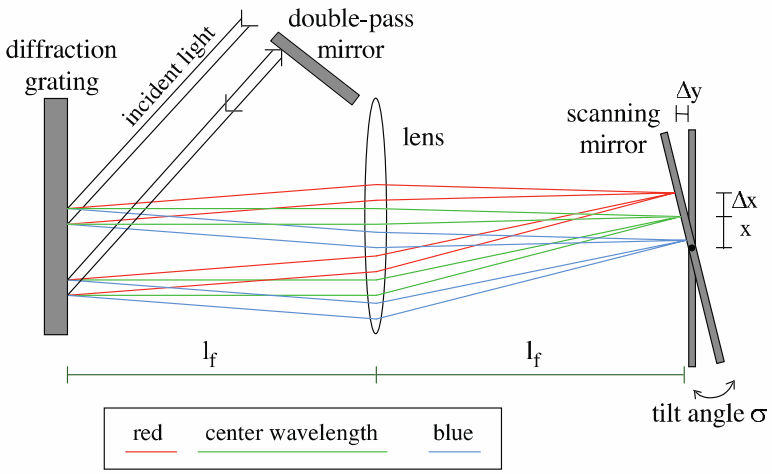

Figure 3.12. Schematic diagram of the rapid scanning optical delay line [5].

In Figure 3.12, light from the interferometer is collimated onto a grating where it is then spectrally dispersed. This results in a phase ramp as a function of wavelength since some wavelengths travel a longer path to the rapid scanning mirror (depending on its position). The scanning mirror returns the various wavelengths back onto the grating where a second, inverted phase ramp occurs such that all wavelengths have now been delayed by an equal amount. The light then hits the double pass mirror and undergoes the same process a second time before returning to the rest of the system. Since video rate 2-dimensional imaging is required, the system must be capable of producing approximately 30 image frames every second. With OCT images typically incorporating 256 depth scan pixels, the delay line must be capable of almost 8000 depth scans per second. The fast-scanning mirror must therefore

operate at a frequency of at least 8 kHz. For this reason a GSI Resonant Optical Scanner capable of a fixed, 8 kHz scan rate was used [6].

The resonant counter-rotating scanning (CRS) galvanometer scans at an actual sinusoidal frequency of 7910 Hz. A pixel clock output is provided which linearizes spot placement throughout the scan field by accounting for the sinusoidal motion of the mirror. This is only active in the most linear portion of the scan. For each half-period (i.e. a full sweep of the mirror in one direction) the pixel clock is active 66% of the time. This is equivalent to 88% of the scan amplitude as shown in Figure 3.13.

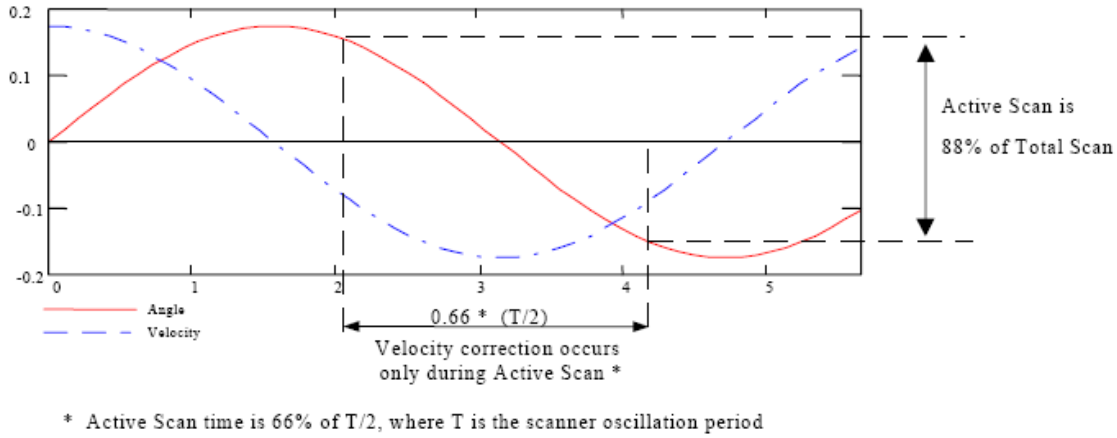

Figure 3.13. Graph showing the relationship between scan angle, mirror velocity and pixel clock output for the CRS scanner. Taken from the GSI Lumonics Counter Rotation Scanner User Manual.

3.6.4 Lateral scanning mechanism and imaging

A lateral scanning mechanism provides *x*- and *y*-axis scanning in conjunction with the *z* (depth) scanning provided by the reference arm. For two dimensional scanning (e.g. *x* and *z*), the lateral scanner only needs to operate at the frame rate, i.e. 30 Hz.

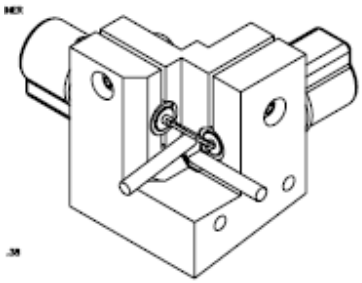

Figure 3.14. Schematic drawing of the mount for the lateral scanning galvanometers. Taken from [6].

A two-axis, galvanometer-based, moving magnet optical scanner system from GSI is used. Each axis can be driven by any waveform, to frequencies greater than 3500 Hz [6]. The mounting arrangement for these is shown in Figure 3.14. The galvanometers, along with a suitable lens and fibre connection have been designed into a hand-held probe (Figure 3.15)

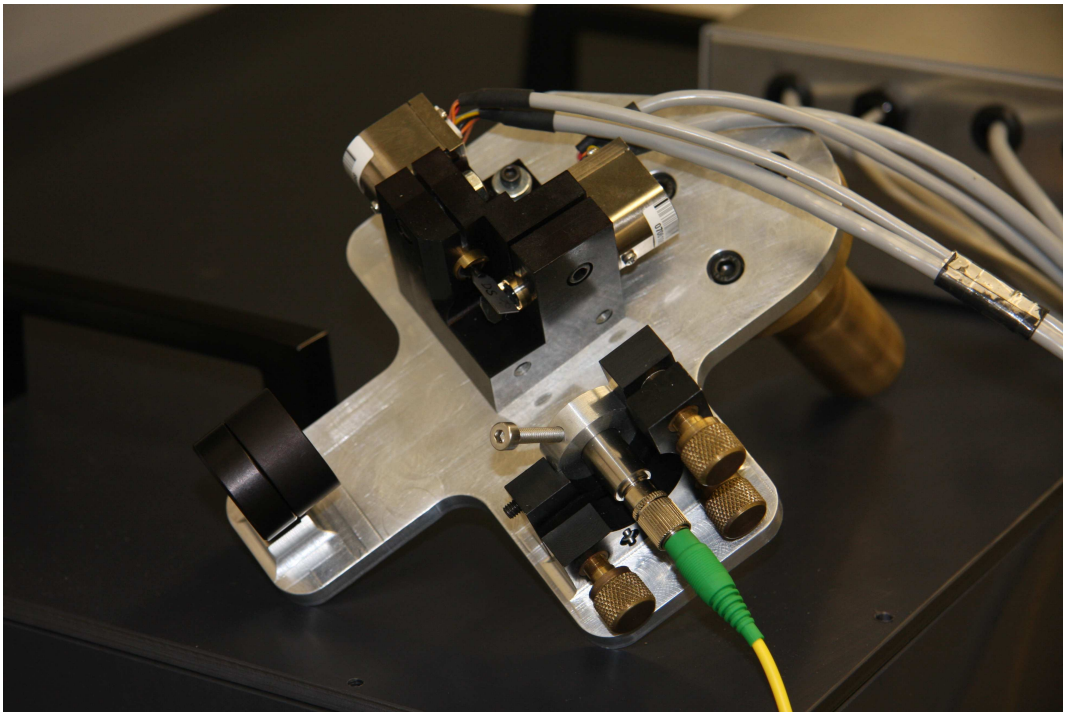

Figure 3.15. Photograph showing the hand-held probe, including lens (bottom left), fibre collimator (bottom right) and scanning galvanometers (centre).

Various suitable lenses have been trialled as a confocal microscope objective. These set the surface pixel size (lateral resolution) of an image while, hopefully maintaining a large enough depth of focus (Rayleigh range) to clearly image the whole depth scan.

The two galvanometers provide lateral scanning over two orthogonal axes (*x* and *y*), giving the system full 3D imaging capabilities.

3.6.5 Detector

The same detector was used in the final system as has previously been described in section 3.2.3.

3.6.6 Sequence of events for obtaining an image

This section aims to describe the step-by-step process needed to control the various OCT system components. The components involved are a fixed-frequency, galvanometer-mounted scanning mirror (the CRS, or Counter Rotation Scanner) that provides depth scanning capabilities into a sample, and 2 identical, independently-controllable galvanometer mounted mirrors for lateral (surface) scanning in 2 dimensions *(x* and *y*). The available inputs and outputs from these components are described in the following sections.

3.6.7 Depth scan acquisition

The sequence of events required to obtain a single depth scan is as follows:

- A “start scan” signal is given from software that turns on the CRS scanner.
- When the mirror reaches the position at the start of the linear region the pixel enable output goes high, indicating that pixel clock data is now valid. The pixel clock provides a timing pulse for each pixel location.

- The pixel clock signal triggers the computer to record the detector output at each pixel location (512 points in total). As shown in Figure 3.12, the linear region of the scan lasts for 66% of each half period, equating to approximately 44 μs. 512 pixels will be recorded in this time at varying frequencies up to 15 MHz.
- When the mirror reaches the end of the linear region the pixel enable signal goes low, triggering the computer to stop recording the detector output.

3.6.8 Two-dimensional image acquisition

To produce a two-dimensional image a second axis (e.g. *x)* is used. This is incorporated into the sequence described previously by using the time period in which the pixel clock is inactive between depth scans to move the *x*-axis mirror to the site of the next depth scan. The imaging sequence now runs as follows:

- The *x*-axis mirror is moved to the position of the first depth scan.
- The CRS scanner starts to perform the first depth scan (pixel enable is high).
- When the CRS scanner is traversing the linear region of mirror motion, the pixel clock is active and 512 clock pulses are provided to time the recording of image pixels.
- As the CRS scanner reaches the end of the linear scanning region the pixel enable signal goes low and detector output is no longer recorded.
- The pixel enable low signal triggers the *x*-axis mirror to move the imaging point to the next depth scan location. This must happen before the pixel enable signal goes high.
- The CRS scanner changes direction while the *x*-axis mirror is moving and proceeds in the reverse direction. When the CRS mirror again reaches the linear scanning region, the pixel enable signal goes high and the pixel clock provides timing pulses for the recording of depth pixels.

- This process is repeated for as many depth scans (*x* locations) as are necessary to form an image.

The *x*-axis galvanometer is controlled using the "command waveform" and "servo enable" inputs. If lateral resolution is to be roughly equal to depth resolution (~10 μm) then the *x*-axis mirror needs to move the imaging point a distance of 10 μm in approximately 20 μs. When 512 pixels have been recorded from a depth scan the *x*-axis mirror can be triggered (by the pixel enable signal going low) to move the required distance before the next depth scan starts.

One obvious thing to note here is that the depth scans are recorded in alternating directions, i.e. top to bottom followed by bottom to top etc. This needs to be accounted for when performing Fourier transforms and assembling the image from the individual depth scans.

3.6.9 Three-dimensional images

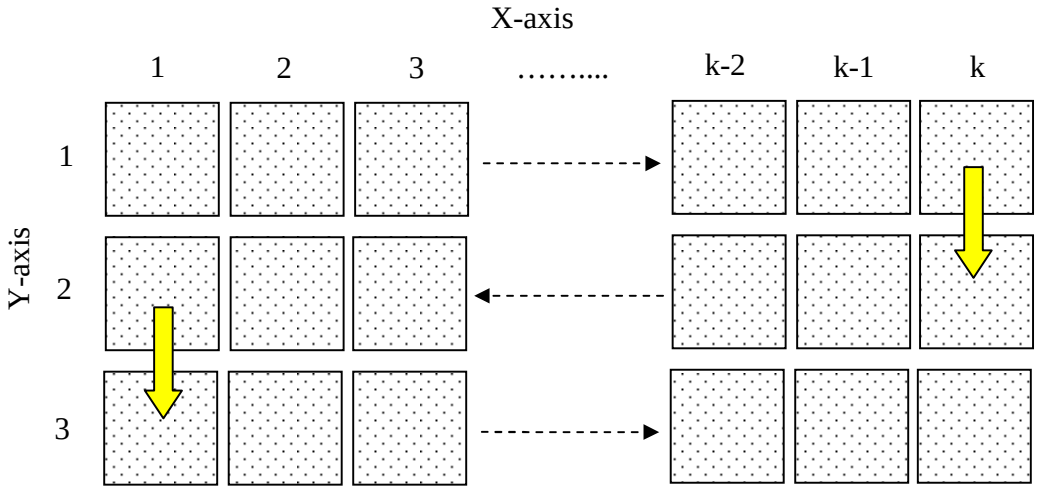

Figure 3.16. Diagram showing the raster scanning technique to be used in forming a 3D image. Each red square represents one depth scan location consisting of 512 pixels. The images are scanned from 1 to k along the x-axis before stepping down to y-axis row 2 and scanning backwards from k to 1.

Future acquisition of 3 dimensional images will require a simple extension to 2D image capture. The number of *x*-axis locations is set to some number, *k*. After *k* depth scans have been performed, as described for 2D images, the pixel enable low signal from the CRS scanner is used to trigger the *y*-axis mirror to move to the next line of the image. This is shown in Figure 3.16. This requires some method of counting the number of *x* locations that have been scanned in order to determine when the pixel enable low signal causes *y*-axis motion rather than the usual *x*-axis motion. The *y*-axis galvanometer is controlled via its "command waveform" and "servo enable" inputs.

3.6.10 Resolution control and imaging parameters

The depth *(z* axis) resolution of the system is fixed by physical constraints of the system. There can only be 512 depth pixels timed by the pixel clock and the distance over which they are recorded is controlled by physical components of the system. Resolution in the lateral *(x* and *y*) directions is completely adjustable; the distance the mirrors move for each step, and the number of pixel locations in each direction, being the deciding factors. Ideally, these would be adjustable from software, and will be once imaging calibration has taken place. For example, a high frame rate might be required to image moving objects within a sample. In this case (for a 2D image) the number of *x* pixels would be reduced to achieve the desired frame rate. The distance between *x* mirror steps is a separately controllable parameter governing the final size of the image. Labview GUI controls to adjust the number of pixels recorded in both lateral directions are required together with an estimate (and real-time readout) of the frame rate. The image dimensions are also adjustable; controlled via the number of pixels and the step size between pixel locations. For example, for a 4 mm-wide image at 256 pixels, the galvanometer step-size would be set to approximately 15 μm.

For an image made up of two dimensions; namely depth and one lateral dimension, it would in future be useful to be able to select which lateral axis *(x* or *y*) is to be

used. This will enable samples/specimens to be imaged in two planes without mechanical manipulation. Two dimensional OCT imaging is analogous to B-mode (Brightness mode) ultrasound imaging were the pixel brightness in an image is determined by the amplitude of the returning signal.

3.6.11 Post-capture data processing

The control and positioning of the various mirror components is only one part of the imaging process. The post-capture data processing sequence also needs to be correctly implemented.

Raw data is going to be arriving at the computer in "packets" of 512 pixels. Each packet can be considered as a separate entity as far as the data processing procedure is concerned. The data in these packets is in the time domain for spatial data. The system is going to eventually produce Doppler images of flow and so some phase resolving is required along with the amplitude provided by the FFT. The Hilbert transform can provide the solution to this problem because it can provide the phase of a signal as its complex argument. The amplitude can then be produced by analytic continuation, as shown in Figure 3.17.

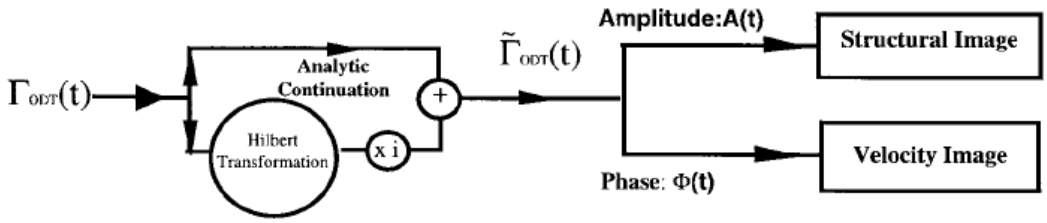

Figure 3.17. Image reconstruction algorithm for phase-resolved ODT. Taken from Figure 9 in [7].

Other post-capture features, such as various image enhancement techniques should also be considered. These include:

- Adjustable threshold levels. These allow the low-end intensity level in an image to be set, below which all pixels are displayed as black.
- Intensity scaling. Pixel intensities are usually represented on a logarithmic scale.
- For velocity (phase) images: false colouring would be appropriate to represent flow rates and direction.
- Some method of measuring the distance between 2 points on an image would be useful.
- For a selected pixel, readout of the flow rate at the point would be useful.

The system displays two-dimensional images as it receives them, so that the display is updated in "real time". A displayed image also needs to be able to be saved to file at any point. Three-dimensional images will probably just be recorded straight to file as the system will not be able to maintain a very high frame rate (<1 fps).

3.6.12 System software

The imaging portion of the system software was written for this project by Dr. Med Benyezzar of the Photon Science Institute, University of Manchester. This software acts as a slave to the Labview program written to use the various timing signals provided by the system electronics. It uses an Alazartech fast DAQ card to capture the frame data and then stream it to a display. A flow diagram detailing the methodology of the program is shown in Figure 3.19.

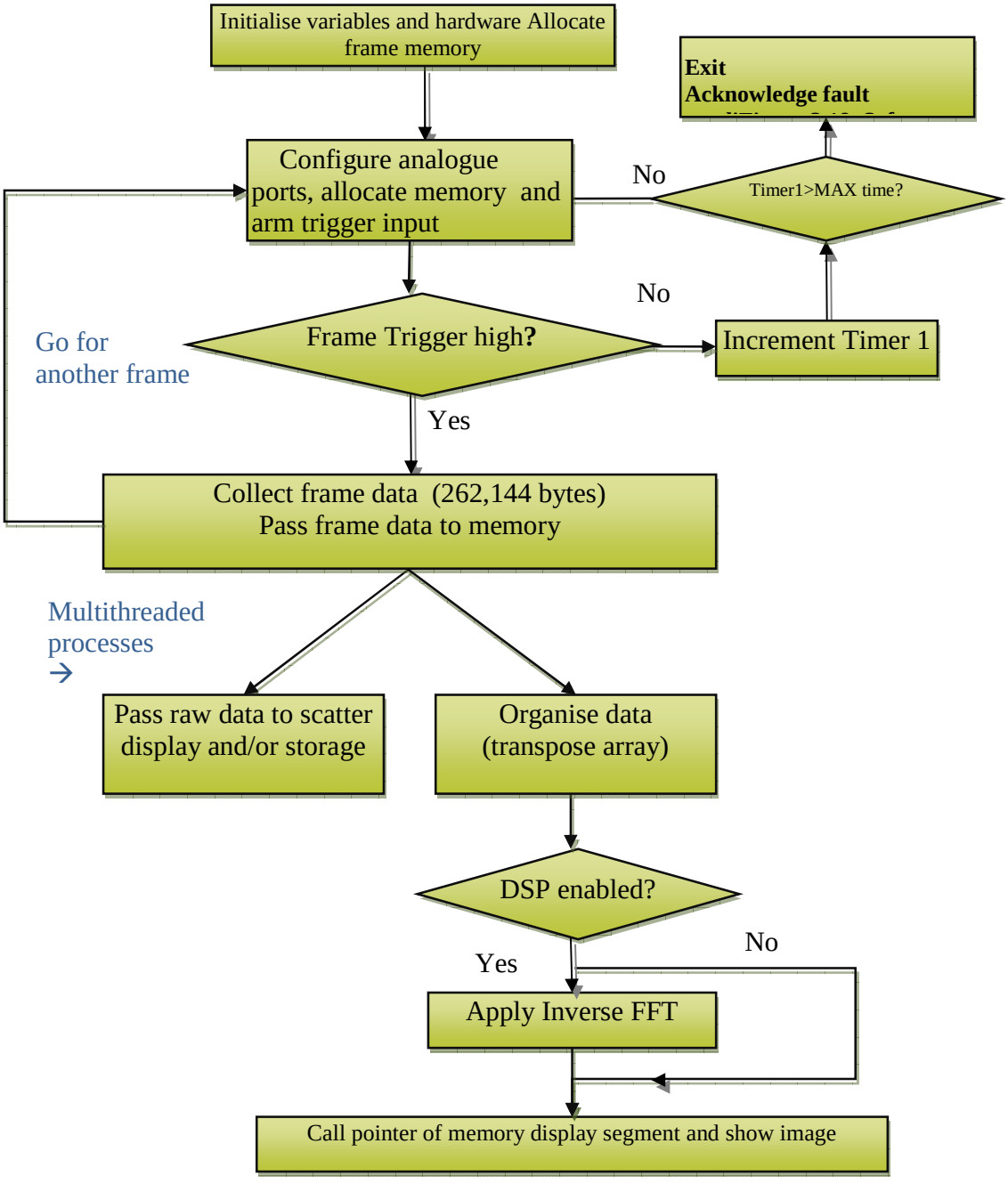

Figure 3.19. Flow chart describing the high-speed portion of the OCT system software.

3.6.13 System electronics

The CRS mirror is controlled by 2 circuit boards; one providing power and amplitude control while the other deals with timing and pixel separation issues.

The *x-y* scanners are controlled by 2 circuit boards (one per axis) that provide power and scan waveform information. Unlike the CRS mirror, the *x-y* galvanometers do not move resonantly and so can be programmed to move with various different waveforms or with discrete control steps.

The electronics for the CRS mirror and the *x-y* galvanometers are mounted in two separate enclosures. Each enclosure has connections for input of power and command signals and for output of various monitoring signals. Connections to the appropriate mirror/galvanometer combination are also provided.

A triple-output, 350W power supply is used with the system. This has been mounted in a custom enclosure; connection details and diagrams are described in section 3.6.15.

3.6.14 System overview

The various components making up the scanning electronics are connected together in the following way. The power supply unit (PSU) provides ±15 V DC and +5 V DC to both the CRS and the XY electronics. A 0-5 V DC variable signal and 2 TTL logic signals are also provided to the CRS system from the PSU for amplitude control purposes. All other inputs and outputs from both sets of electronics are connected to the computer via a 10 MSamples/s data acquisition card. A schematic diagram of the entire system is shown in Figure 3.20 below.

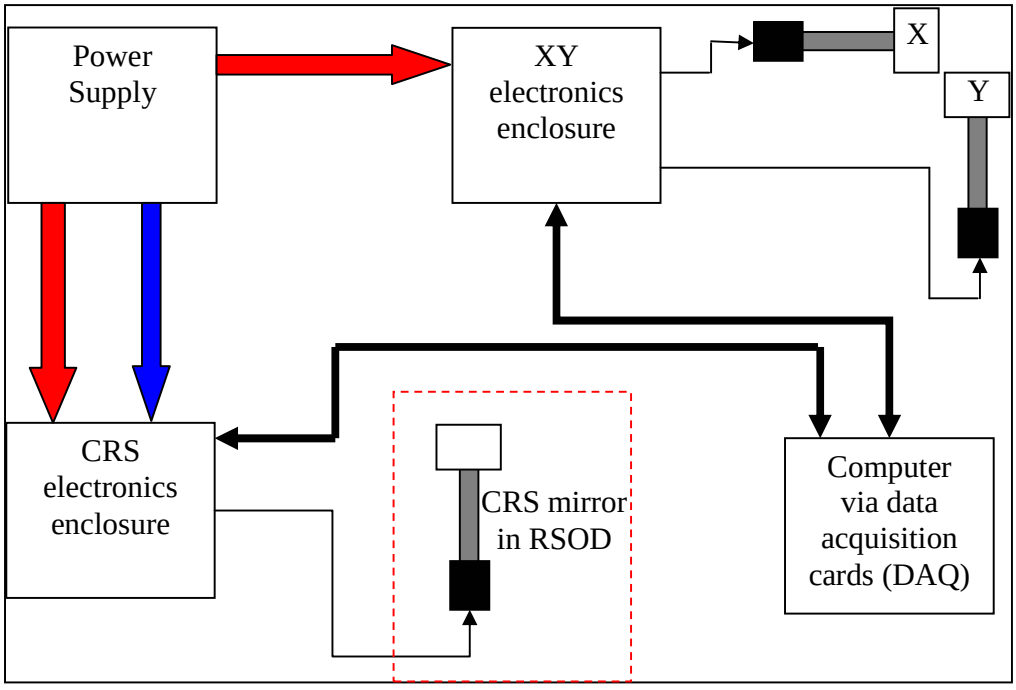

Figure 3.20. Schematic diagram of the OCT scanning system electronics, showing connections between major system components. The red arrows indicate ±15 V d.c. & +5 V d.c. supply lines while the blue arrow indicates amplitude control signal connections.

There now follows a brief description of each of the components shown in Figure 3.20.

3.6.15 Power supply (PSU)

The power supply is manufactured by Vicor (http://www.vicr.com) and has part number VI-RU022-EYVV. It is a switched mode unit from the Vicor FlatPAC range. A single mains (230 V A.C.) input consisting of live, neutral and earth connections is required. The PSU provides three separate outputs of 5 V, 15 V and 15 V. These are rated at 50 W, 150 W and 150 W respectively, meaning that each one of these outputs is capable of delivering a current of 10 A. Although the electronics to be powered using this unit don't require anywhere near the power output it is capable of, the PSU was chosen as it was the cheapest available that had the required combination of voltage outputs.

The PSU enclosure has appropriate sockets that allow it to provide power to other components in the system. These are mostly just straight through connections providing combinations of 5 V or 15 V, but there is also a potentiometer-controlled variable 5 V output along with two switch-controlled logic outputs which control the oscillation amplitude of the CRS mirror.

The PSU provides power to the two-axis (*x*-*y*) lateral scanning mirrors at the sample beam delivery point as well as to the resonant scanning (CRS) mirror and associated electronics in the rapid scanning optical delay line.

The PSU is a 3-up (triple output) version of the FlatPAC series by Vicor (http://www.vicr.com) Outputs 1 and 2 are linked together to create a dual-rail supply of ±15 V. The centre-tap of this dual-rail supply is designated as 0 V and is common with the 0 V connection from the 5 V output.

The 240 V AC input to the PSU is connected via a switch and fuse built into the housing. The switch has a built-in neon lamp indicating the on or off condition. The FlatPAC unit has screw terminal connections for the three standard 240 V AC

inputs; Live, Neutral and Earth. Both the PSU Earth input and the (metal) chassis are connected to the mains input Earth lead. All wiring for the power supply has been carried out in accordance with appropriate health and safety guidelines. Mains wiring is of the three-core, Brown-Blue-Green/Yellow (Live, Neutral, Earth) type. DC-side wiring is also colour-coded using a Red-White-Black scheme. Red is used to indicate positive voltages (+5 V or +15 V), white indicates ground (0 V) while black wiring is used to conduct negative voltages (-15 V). All DC wiring is of the multi-core (stranded) type comprising of 24 0.2 mm conductors in a PVC sheath.

The DC terminals of the FlatPAC PSU are #10-32 studs supplied with appropriate nuts and washers. Insulated eyelet crimp terminals are use throughout for connecting wire to the PSU DC outputs. All solder joins between chassis sockets and wire are insulated with heat-shrink sleeving. The wiring diagram for the PSU is shown in Figure 3.21 , on the next page.

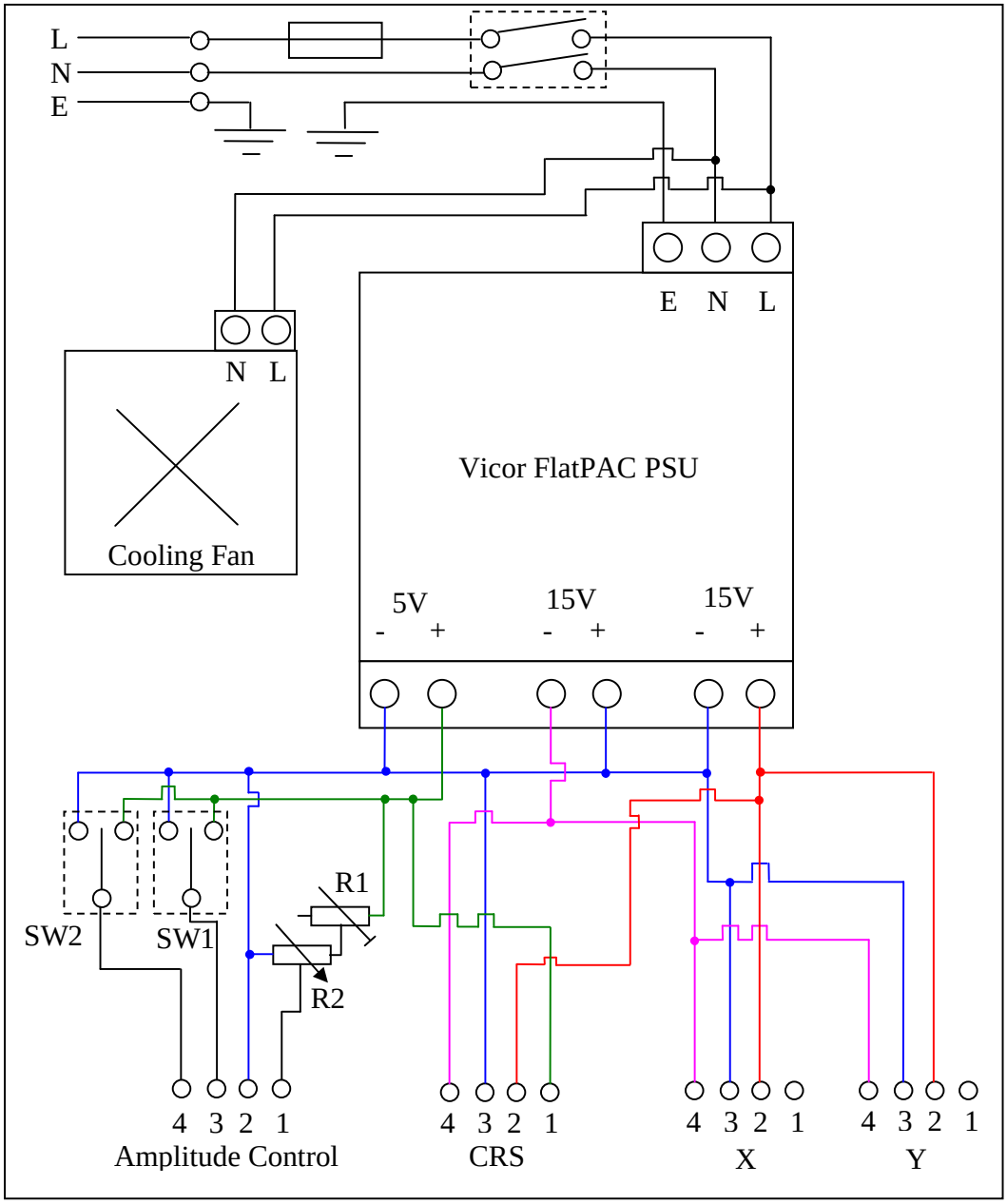

Figure 3.21. The wiring diagram for the power supply. Mains supply connections are shown at the top, including connections to a mains-powered cooling fan. DC connections are shown at the bottom, colour-coded for clarity. Red lines are +15 V, blue lines are 0 V, pink lines are -15 V and green lines are +5 V. Black lines on the DC side indicate that the voltage is variable/adjustable. Pin 1 on the *x* and *y* connectors is unconnected.

Choosing the right value fuse is crucial in ensuring that electronics (and users) are adequately protected against short circuits and faults. The Vicor FlatPAC unit used here is marked as having a current draw of 4.3 A from a 240 V (mains) supply. The

mains-rated cooling fan also connected has a nominal current draw of 0.125 A giving a total maximum current draw of 4.425 A for the unit. A 5 A fuse has therefore been fitted to both the 3-pin mains plug and to the 20 mm fuse holder built in to the unit itself.

At maximum power, 350 W needs to be dissipated as heat by the PSU. The FlatPAC unit has an integral heat sink for this purpose. The Vicor Design Guide & Application Manual has extremely detailed instructions on how best to provide a suitable thermal environment for the power supply. Thermal curves for the FlatPAC series are also provided, as shown in Figure 3.22.

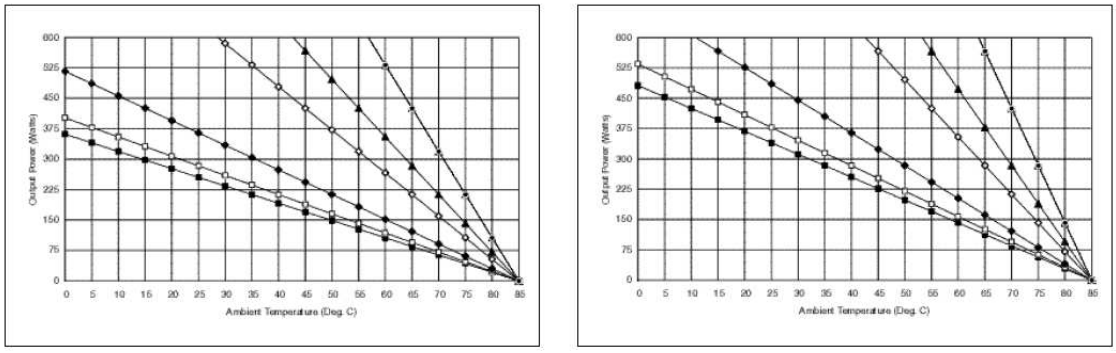

Figure 3.22. Thermal curves for the Vicor FlatPAC series. Graphs are output power (*y*-axis) versus ambient temperature (*x*-axis). The various curves are for varying air flow conditions, starting with free air H & V (two flattest lines), then 200 LFM (linear feet per minute) air flow and then rising in steps of 200 LFM from there. Graph on the left is for 5 V outputs, graph on the right is for 12-48 V outputs.

The curves in Figure 3.22 show give the maximum ambient temperature for which a particular output power can be maintained, given the air flow conditions. They show that, for free air (i.e. no fan or air movement other than convection) the maximum ambient temperature for which 350 W can be maintained is around 15-20°C. From elsewhere in the design guide, this condition would also result in the temperature of the heat sink reaching 85°C! For these reasons the cooling fan shown in the wiring diagram (Figure 3.21) was added. The airflow characteristics of the fan are unknown but it should easily be able to allow the PSU to operate in ambient

temperatures of 40-50°C. This provides a reasonable safety margin above "normal" room temperature operation. The fan is mounted above the main heat sink on the power supply and will suck air out of the case. Vents in the side panels provide inward flow for cool air.

3.6.16 Amplitude control

The amplitude control output of the PSU is used to set the oscillation amplitude of the resonant scanning mirror. The oscillation amplitude can be varied continuously by adjusting the ZOOM voltage between 0 and 5 V; maximum amplitude is achieved at 5 V. Further control is possible by applying logic signals to the SEL0 and SEL1 CRS inputs. The combination of the SEL0 and SEL1 signals creates a 2-bit signal that can reduce the oscillation amplitude by factors of 0.75, 0.5 and 0.25.

The ZOOM voltage is controlled by the potentiometer R2, in combination with the preset potentiometer R1. This preset potentiometer sets the maximum possible output voltage, allowing adjustment for power supply inaccuracies and also a safety margin, as a ZOOM voltage greater than 5 V may damage the resonant mirror. R2 then provides complete variation between 0 V and the ceiling set by R1. The SEL0 and SEL1 signals are controlled by the switches SW1 and SW2 respectively.

3.6.17 PAT testing

The unit was PAT tested on 16/1/2008 by Paul Spiteri in the Electronics Workshop, School of Physics & Astronomy. The PAT test certificate is valid for 3 years from the test date.

3.6.18 x-y electronics

The electronics controlling *x* and y axis scanning are MiniSAX II servo controllers, manufactured by GSI (http://www.gs-scanners.com). The arrangements for both *x* and *y* axes are identical; they are 2 copies of the same system. The MiniSAX II consists of a single circuit board mounted on a large heat sink. It has two input connectors; one for power and one for control signals. Two output connectors connect the MiniSAX II to the VM500 galvanometer-mounted mirror.

The *x-y* electronics enclosure contains two MiniSAX II boards, one for each axis. The power/control inputs enter the case via two sockets per axis. Connection to the galvanometer is by the supplied cables, two per axis. These exit the enclosure through a cable clamp/grommet arrangement.

3.6.19 CRS electronics

The control electronics for the CRS mirror are mounted in a similar enclosure to the *x-y* electronics. The electronics consist of 2 circuit boards; a "driver" board and a board called the "pixel clock". These boards connect electrically via a 14 pin ribbon cable. The driver board has one 16 pin input connector for power and control signals, and one output connector to connect to the pre-moulded cable of the CRS mirror. The pixel clock board has a single 24 pin connector for transmission of the pixel clock timing signals.

The enclosure has 3 connectors, allowing power and control signals to be separated. The pre-molded CRS cable exits the box through a clamp/grommet arrangement similar to the *x-y* enclosure.

3.6.20 Data acquisition cards (DAQs)

There are two DAQ cards used in the system. One (high speed) is used to record the OCT signal coming from the detector, while the other (lower speed) is used to control the *x*-*y* scanners and various other I/Os.

The lower speed DAQ is a National Instruments (http://www.ni.com) unit, specifically the PCI-6115. This is coupled with a connection board (BNC 2110) which allows BNC connections to 4 analog input channels and 2 analog output channels, all of which can be either pseudo-differential or grounded. There are also various TTL logic outputs available; connection to these is via spring-loaded insertion terminals. This DAQ is capable of 10 million samples per second for each analog input channel with 12-bit resolution.

The high speed DAQ is made by Alazartech. It has two high-speed (at least 100 million samples per second) inputs. This card is clocked using the pixel clock output from the CRS electronics.

3.6.21 Frame trigger & ramp generation

The following routine is programmed in NI Labview to respond to various timing signals provided by the system electronics. See also. Frame Trigger Generation

The Pixel Enable signal is connected to the NI card at a counter/timer input, CTR0.
The counter is set-up so that it generates a high output, CTRout0, (logic 1, +5 V) for N (= 256) 'ticks' of the input, CTR0. A 'tick' is defined as a falling edge on CTR0.
N can be adjusted by the user, and it defines the frame width (256 in our case).
The counter output, CTRout0, is the Frame Sync, or Frame Trigger signal. This is connected as the trigger for the Alazar card.

Ramp Generation occurs as follows: The ramp is pre-defined as N (=256) steps between voltages V_1 and V_2. The Pixel Enable signal, input on CTR0, is used as a clock for the ramp analogue output. On each falling edge of the clock the ramp steps to the next value in the sequence, output on Aout0. The trigger for this output is the Frame Trigger signal (rising edge), available from CTRout0.

In this way the ramp stays at each level for the capture of just 1 A-scan/line, and only moves during the period when no data is being recorded.

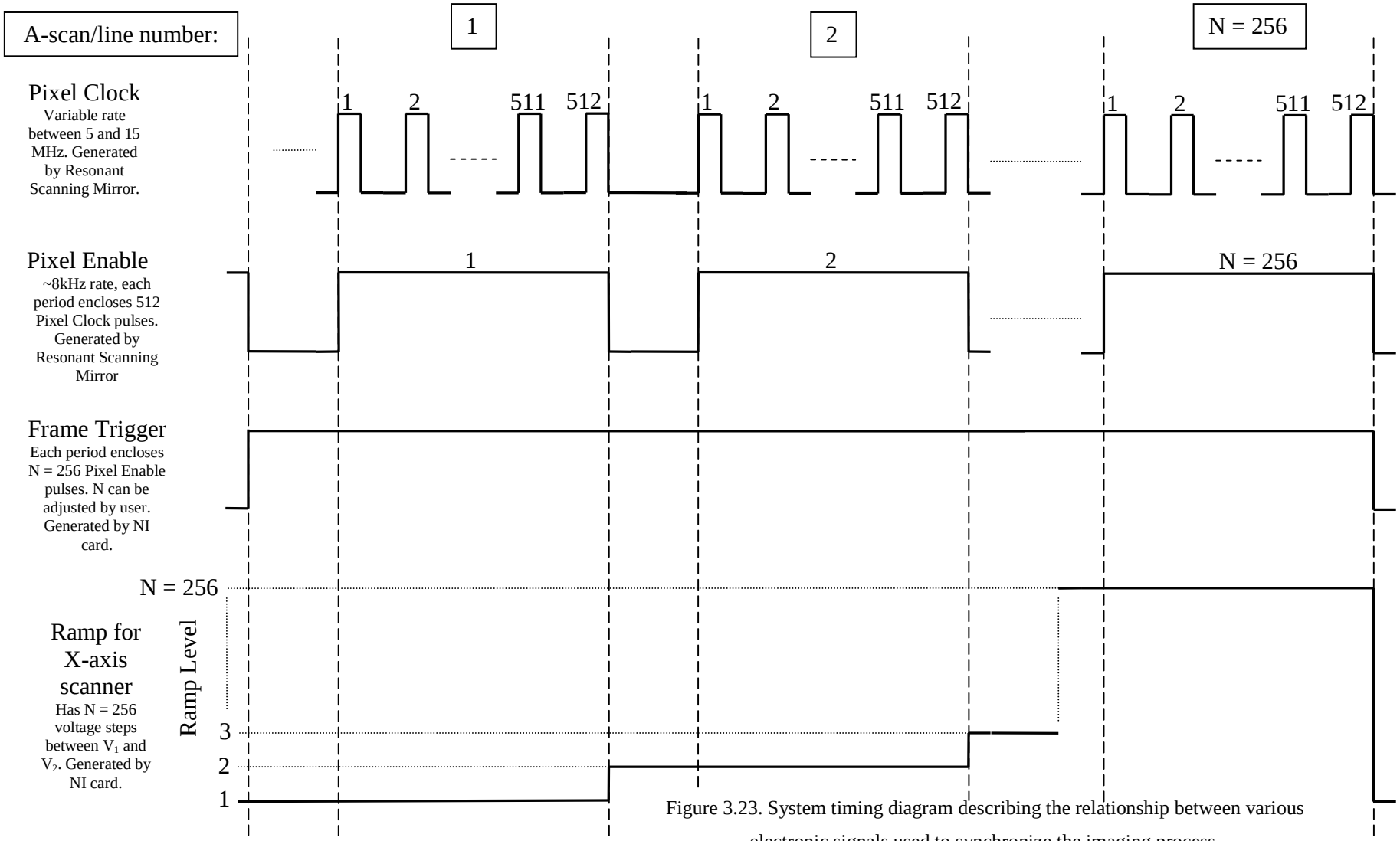

Figure 3.23. System timing diagram describing the relationship between various electronic signals used to synchronize the imaging process.

3.7 System photographs

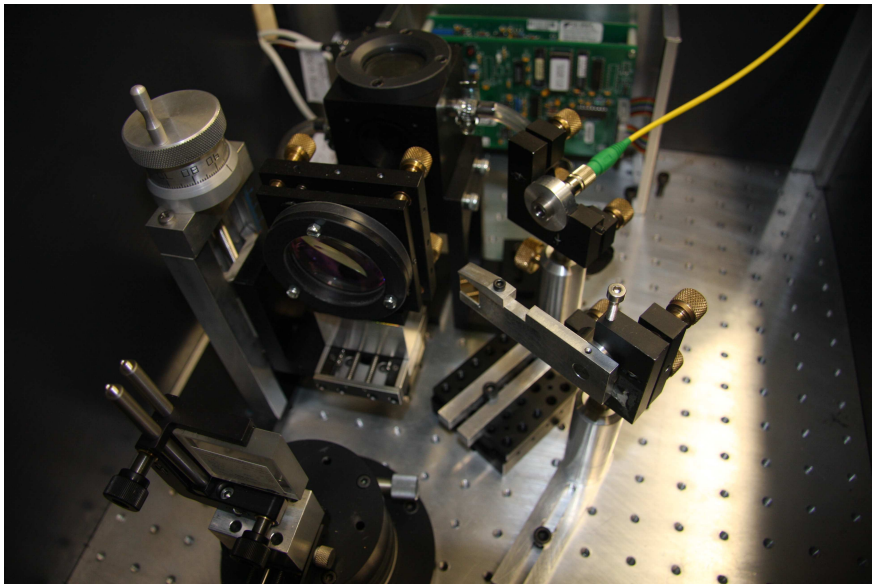

Figure 3.24. Photograph showing the optical components within the RSOD.

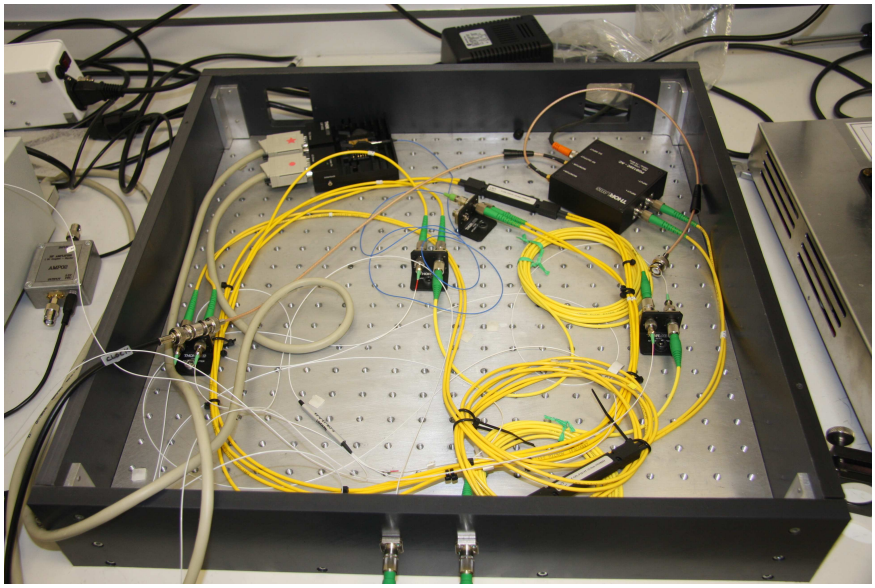

Figure 3.25. Photograph showing the fibre-based interferometer, along with detector and SLD.

Figure 3.26. Photograph of the OCT system PSU.

3.8 Preliminary OCT system images

After the OCT imaging system had been built as previously described some preliminary imaging tests were done in an attempt to assess initial performance.

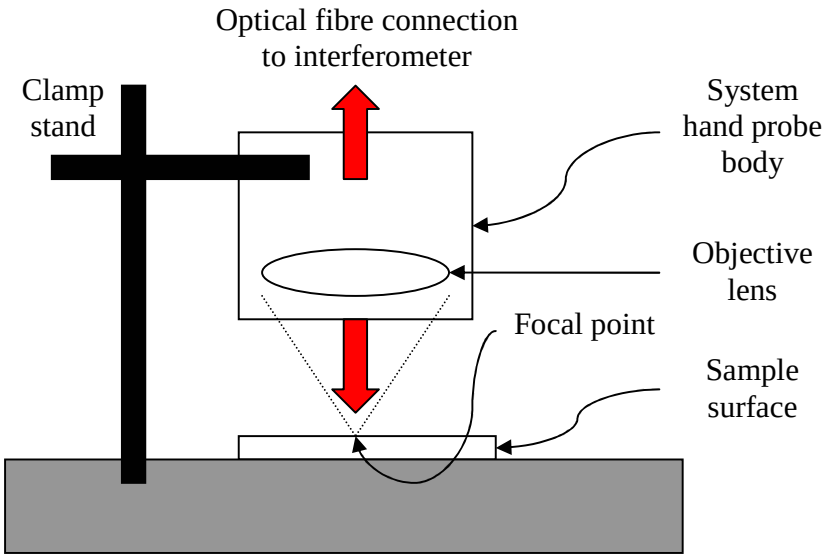

Figure 3.27. Diagram showing the experimental set-up used in acquiring preliminary images from the OCT system.

Figure 3.28 shows the experimental configuration used to capture some initial test images. The hand piece previously described in section 3.6.4 (and shown in the photograph in Figure 3.15) was mounted securely on a clamp stand such that the imaging plane was horizontal and parallel with the optical table. The objective lens had a focal length of 75 mm and was 25.4 mm in diameter. Imaging was performed with lateral scanning over a distance of approximately 0.5 mm for all samples. Images were captured from reflective surfaces such as glass, acrylic or mirror surfaces to maximize the amount of light returning to the detector during the testing phase. An example of the sort of images initially recorded is shown in Figure 3.28.

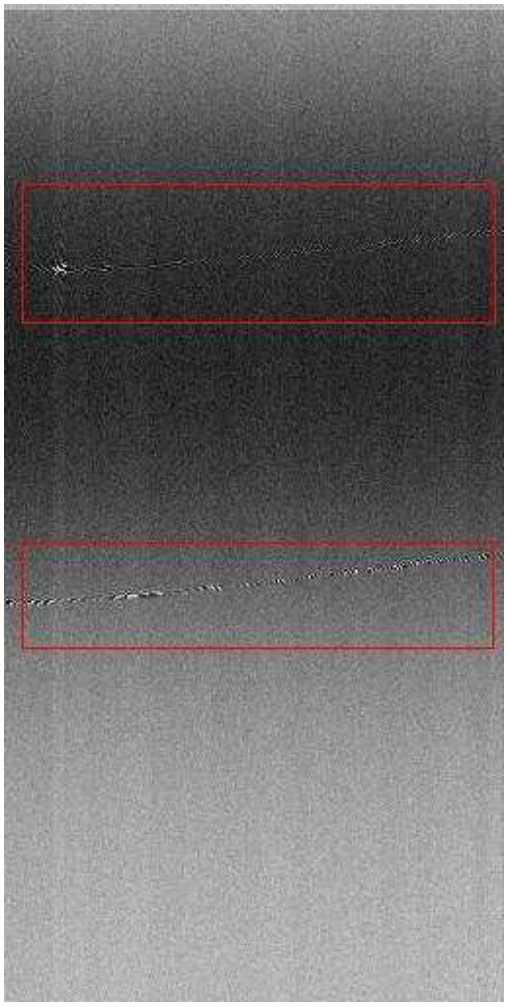

Figure 3.28. Cross-sectional OCT image of a 1 mm thick transparent acrylic slide. The image is 512 pixels vertically by 256 pixels horizontally, with approximate physical dimensions of 3 mm (h) by 0.5 mm (w). The highlighted red areas show the signal received from the upper and lower surfaces of the slide.

As can be seen from the image in Figure 3.28, the interference signal was fairly weak. The black-and-white banded appearance of the two surfaces is a result of the software displaying the “raw” interferogram, as opposed to the envelope of the signal. This produces a rapidly alternating positive (white) and negative (black) effect rather than the single intensity level that might be expected from such a surface.

In an attempt to improve the image, a simple high frequency cut-off filter (an RC circuit) was placed in-line between the photodetector and the DAQ card in the PC. The corner frequency of the circuit was empirically adjusted until the black-and-white banding just disappeared, meaning that the higher frequency modulations of the interferogram were being filtered, but the envelope at each image "feature" was being preserved. A second image, showing the effect of the filter, is shown in Figure 3.29.

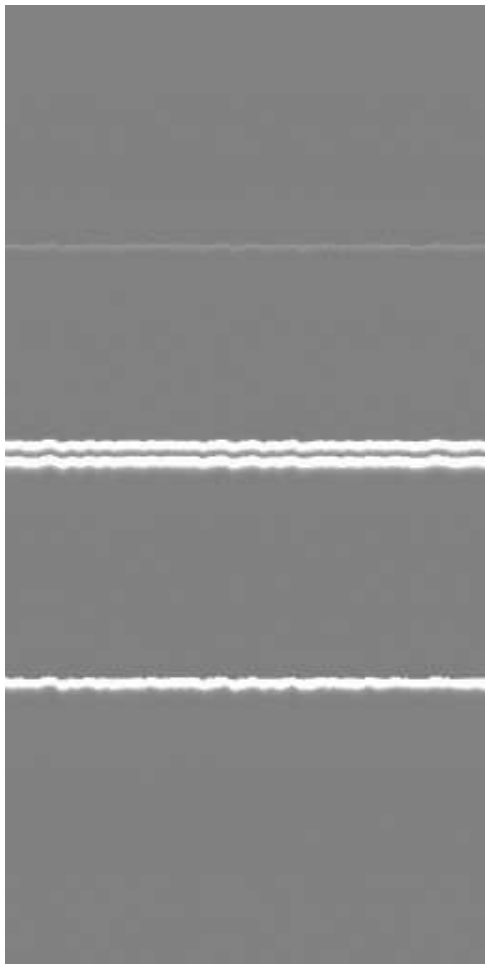

Figure 3.29. Cross-sectional OCT image of two 1 mm thick transparent acrylic slides stacked one on top of the other. The image is 512 pixels vertically by 256 pixels horizontally, with approximate physical dimensions of 3 mm (h) by 0.5 mm (w).

A side effect of the high-frequency cut-off filter, as applied in Figure 3.29, is that much of the background noise is removed resulting in the smoother overall appearance of the grey background.

From measurement of the line thicknesses at the slide boundaries in Figure 3.29, the vertical resolving ability of the system can be determined. The lines are between 5 and 10 pixels thick, which, when translated into distances at approximately 6 µm per pixel, yields slide boundaries of between 30 µm and 60 µm thickness. These boundaries would be expected to be thinner than the resolution limits of the system, so this result suggests some broadening is occurring. This could be a result of several factors, including the effect of the high-frequency cut-off filter described above, or the misalignment of lens focal point and the depth location at which interference occurs. Further work, including a replacement objective lens, is planned to rectify these issues.

3.9 Conclusions

A fast OCT system has been built incorporating an RSOD, SLD light source, and mostly fibre construction. Although still being tested, the system should be capable of video-rate imaging at depth resolutions of approx. 12 µm.

Initial images demonstrate the basic success of the system, but lack the quality and precision required to fully explore the systems capabilities at this time.

3.10 Further work

The OCT system as described does not fulfil the criteria asked of it. In its current state it cannot produce high-quality images in tissue, and it does not allow access to any functional data that can be extracted from OCT signals. The first issue is

therefore to bring the system up to working order. This requires several points to be addressed. Firstly, a high-quality achromatic lens has been obtained with a high numerical aperture. This will allow distortion-free imaging, with more light concentrated where required. Since this lens has been acquired the system requires re-aligning, to take into account the change in focal length and hence path length. The second issue is to ensure that the system is working to its full potential. The geometry of the RSOD is complex, and precision alignment is necessary in order to achieve efficient, low-loss imaging. This requires careful, methodical alignment and optimisation.

Once good-quality structural imaging is achieved, the functional OCT information can then be extracted. The ultimate goal of this system is to image blood flow in vivo in human skin tissue. The components are already available to do this in that there is a fibre-coupled electro-optic modulator (EOM) ready to be used within the system. This has already been characterised to work out switching and phase-control parameters. This device will be used to modulate the interference signal at a high frequency of around 1 MHz. Any Doppler shifts induced by moving scatterers within a sample will cause a frequency shift in the modulations, which can be easily detected.

Ultimately, further clinical studies are planned using this OCT system to image patients in vivo. To prepare for this, imaging of phantoms, and other items will be performed in order to calibrate the system and understand its capabilities.

References

[1] A. M. Rollins and J. A. Izatt, *Optics Letters* **24** (21), 1484 (1999).

[2] Y. Zhang, M. Sato, and N. Tanno, Beijing, China, 2000 (unpublished).

[3] *Laser diode combi controller ITC502 - Operation manual*. (Thorlabs, Inc., 2005).

[4] *PDB100 Series Balanced Amplified Photodetectors*. (Thorlabs, Inc., 2005).

[5] A. M. Rollins, M. D. Kulkarni, S. Yazdanfar et al., *Optics Express* **3** (6) (1998).

[6] *CRS scanners - manual*. (GSI Lumonics, 2006).

[7] Chen Zhongping, Zhao Yonghua, S. M. Srinivas et al., *IEEE Journal of Selected Topics in Quantum Electronics* **5** (4), 1134 (1999).

Chapter 4

A supercontinuum light source for OCT

4.1 Introduction

There are four major selection criteria to be considered when selecting a suitable light source for OCT. These are central wavelength, spectral bandwidth, output power and stability. Axial resolution in OCT imaging is primarily governed by the pairing of source central wavelength and spectral bandwidth. This relationship was described previously in Equation 2.14, where the FWHM of the source spectrum is assumed to be a Gaussian distribution [1]. The choice of central wavelength in OCT-suitable light sources is usually limited by the so-called ‘therapeutic window’; the spectral region within which the absorption of tissue components is relatively low. This area spans from the red end of the visible spectrum (~600nm) and stretches into the near IR, up to around 1600nm [2]. Fortunately, there are many light sources available in this spectral region so efforts have concentrated on improving sources by increasing spectral bandwidth, in order that axial resolution may be improved.

4.1.1 High bandwidth sources used in OCT

The most common illumination source used in OCT systems to date is the superluminescent diode (SLD). These are relatively cheap, compact devices, available with central wavelengths ranging from circa 800nm to around 1.6µm, and bandwidths of up to 80-100 nm for devices emitting around 1.3µm. Typical axial resolutions of 10µm are easily attainable at output powers of several tens of milliwatts.

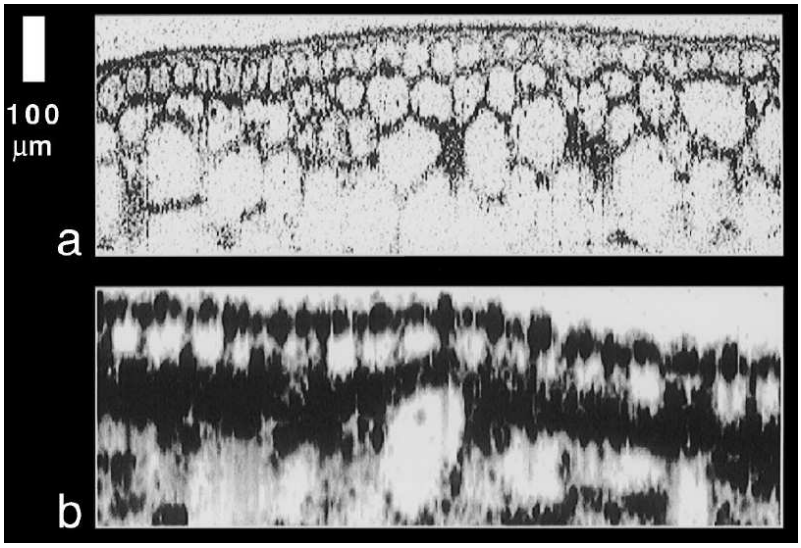

Figure 4.1. A comparison of OCT images produced using a Ti:Al2O3 source (a), and those produced using a standard superluminescent diode (b). Modified from Figure 3 in [3].

While the range of output powers and central wavelengths from SLDs is acceptable, the relatively narrow bandwidths limit imaging performance. Different types of source have been investigated to achieve imaging parameters greater than those provided by SLDs. Mode-locked solid-state lasers are capable of producing high average output power femto-second pulses, resulting in bandwidths measured in hundreds of nanometres. For example: Kerr lens mode-locked (KLM) Ti:Al_2O_3 sources have been used for OCT with impressive results. The output of a Ti:Al_2O_3 source has a central wavelength of around 800nm. Bouma et al. [3] produced a device with an output power of 400mW and a spectral FWHM of 145nm resulting in an axial resolution of 1.9µm in air. Figure 4.1

shows a comparison between an OCT image produced using a Ti:Al_2O_3 source and one produced using a fairly standard, for the time, SLD source. Further improvements in using such high bandwidth sources for OCT have yielded impressive results. A system constructed using a Ti:Al_2O_3 source with a bandwidth of 350nm centred at 800nm yielded images with an axial resolution of just 1µm, allowing the structure inside cells to become resolvable [4].

4.1.2 The importance of source power and stability

The major factor affecting penetration depth and imaging speed in OCT is source output power. Higher powers allow single-scattering events from greater depths to become detectable, and also allow higher imaging speed by lowering the necessary pixel dwell time for adequate detection.

The 'stability' of an optical source, in this description, encompasses two factors: optical noise due to amplitude modulation (i.e. noise inherent within the source), and also the portability/simplicity of the source. The first of these stems from the fact that no real-world light source produces light at a precise constant power. Fluctuations can result from, for example, instability of a current supply used to power a semiconductor-based source such as an SLD. These fluctuations result in changes in the detected amplitude of any interference pattern produced i.e. amplitude noise. This reduces the ability of an OCT system to detect weak signals. The second factor mentioned here is related to the suitability of a particular source for the intended application. Many OCT systems are designed with clinical applications in mind and, as such, they must be robust and of a practical size. Optical sources like the Ti:Al_2O_3 type mentioned previously are large, complex machines and are therefore confined to the laboratory, while SLDs are physically small and operationally stable and so much more suited to the clinical environment despite their inferior optical specifications.

The criteria mentioned previously must all be considered when assessing the usefulness of any novel optical source for OCT imaging.

4.2 Supercontinuum optical sources in optical fibre

When a pump beam is severely spectrally broadened due to nonlinear processes a supercontinuum is said to be formed, consisting of a spectrum spanning many hundreds of nanometres in wavelength with no gaps or discontinuities. Supercontinua have been generated for several decades by pumping various media with short pulse-length laser light. Optical fibres have proved to be particularly suitable for the generation of spectral supercontinua. Some modern supercontinuum optical sources rely on the optical properties of a particular type of optical fibre called photonic crystal fibre (PCF). PCF is also known as “holey fibre” or “microstructured fibre” in the literature. It consists of a small central core of silica glass surrounded by a periodic array of refractive index discontinuities, such as air holes (hence “holey fibre”) or different glass types. The spacing of the array of holes is of the order of a couple of micrometres.

The interesting properties of PCF regarding supercontinuum generation are that it is highly non-linear, can transmit a large range of wavelengths with low losses, and, unlike standard single-mode fibres, can be constructed with a customized zero dispersion wavelength, allowing more efficient pumping. The non-linearity of PCF means that the second-order refractive index causes self phase modulation of the pump beam which can effectively counteract group velocity dispersion in the opposite sense. The balance between these two factors allows for supercontinuum generation.

4.3 A commercial supercontinuum source for OCT

Supercontinuum sources using PCF as the generating medium have been used in OCT systems previously, allowing axial resolutions of 2.5 µm [5] and >5 µm [6] to be achieved. Commercial sources of a similar type are, at the time of writing, starting to appear on the market from companies including NKT Photonics (formerly Koheras) and Fianium.

4.3.1 The Koheras SuperK Compact

An example of a commercially available supercontinuum source is the SuperK series from Koheras (now NKT Photonics) shown in Figure 4.2 below. These are a family of sources ranging from the Compact, capable of nanosecond pulses at kilohertz repetition rates with greater than 100 mW output power, to the Extreme which has an output power of greater than 4 W delivered by 5 picosecond pulses at 80 MHz [7]. The SuperK Compact source was trialled as a possible replacement/enhancement for an existing SLD source in our OCT system.

Figure 4.2. An image of the SuperK Compact from Koheras/NKT Photonics showing turn-key operation and fibre output. Modified image from SuperK Compact product data sheet [8].

An image of the SuperK Compact from Koheras/NKT Photonics showing turn-key operation and fibre output. Modified image from product data sheet.

4.3.2 Specifications

The Koheras SuperK Compact (hereafter referred to as "the Compact") is a self-contained, bench-top source producing a white light supercontinuum output. The specifications of the unit are summarised in Table 4.1 below. As can be seen, the light output has an extremely broad spectral range, covering almost 2 µm. The output is pulsed so detection electronics would require synchronization if the Compact were to be used for imaging.

Koheras SuperK Compact – selected specifications	
Wavelength range	500 nm to 2400 nm
Total average output power	>100 mW
Pulse duration	~1 ns
Repetition rate	24 kHz (typical)
Output fibre type	Single mode
Fibre connector	FC/PC-type
Physical dimensions (HxWxD)	140x350x236 (mm)

Table 4.1. Selected specifications of the Koheras SuperK Compact taken from the product datasheet.

Selected specifications of the Koheras SuperK Compact taken from the product datasheet.

As can be seen from both the image in Figure 4.2 and Table 4.1 the output of the Compact is delivered via a single mode optical fibre terminated with an FC/PC connector, making it theoretically a drop-in replacement for the SLD device currently in use in the OCT system. Physically, the Compact is small and portable, weighing well under 10 kilograms.

4.3.3 The testing process

The Compact source was provided on loan for a trial period of only two weeks by Koheras, and consequently the range of tests performed was limited. The main objective of the trial was to measure some of the parameters that are important in OCT imaging, such as coherence length.

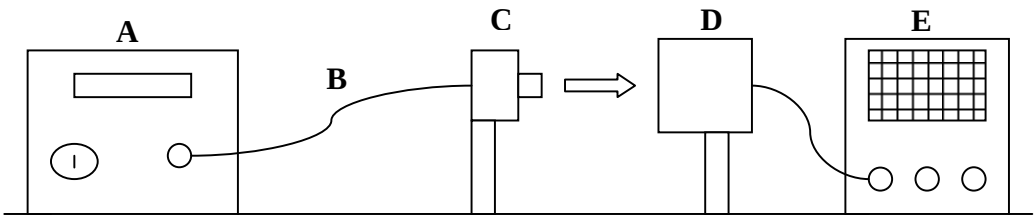

Figure 4.3. A schematic representation of the initial test set-up for the Koheras SuperK Compact source. Key: (A) SuperK Compact source, (B) single-mode optical fibre, (C) Fibre collimator, (D) Photo detector (various - see Table 4.2), and (E) oscilloscope.

After receiving and setting up the Compact, the initial test was to observe the temporal properties of the output light. This was done using the experimental configuration shown in Figure 4.3. The light from the Compact is output via the integral single-mode optical fibre and then collimated. The beam is incident upon a photodetector, the response of which is observed and captured on a digital oscilloscope. In order to observe the photodetector response to a single optical pulse, the oscilloscope is triggered via an electronic signal output from the Compact that is synchronous with the optical pulses.

The extremely wide spectral range of the Compact means that choosing a detector is difficult; one single device will not cover the entire range from 500 to 2400 nm. Several different types of photodetector were available for use in characterising the Compact, specifications are detailed in Table 4.2 below.

Photodetector specifications			
Detector	**Wavelength range**	**Rise time**	**Quantum efficiency**
Thorlabs DET110 Silicon	400 to 1100 nm	20 ns	0.646
Thorlabs PDA400 InGaAs	700 to 1800 nm	35 ns	0.760
Thorlabs DET10D Extended range InGaAs	1.2 to 2.6 µm	25 ns	0.593
Judson J12D InAs	1.0 to 3.6 µm	~2 µs	0.413
Judson J10D InSb	1.0 to 5.5 µm	35 µs	0.783

Table 4.2. Wavelength ranges and rise times of available photodiodes. Values are taken from manufacturer data sheets.

It should be noted that the detector rise times in Table 4.2 are all at least an order of magnitude too large to allow the 1-2 ns duration output pulses of the Compact to be temporally resolved. Analysing the signal due to a single pulse incident upon any of the devices in Table 4.2 will show the detector response rather than the characteristics of the pulse.

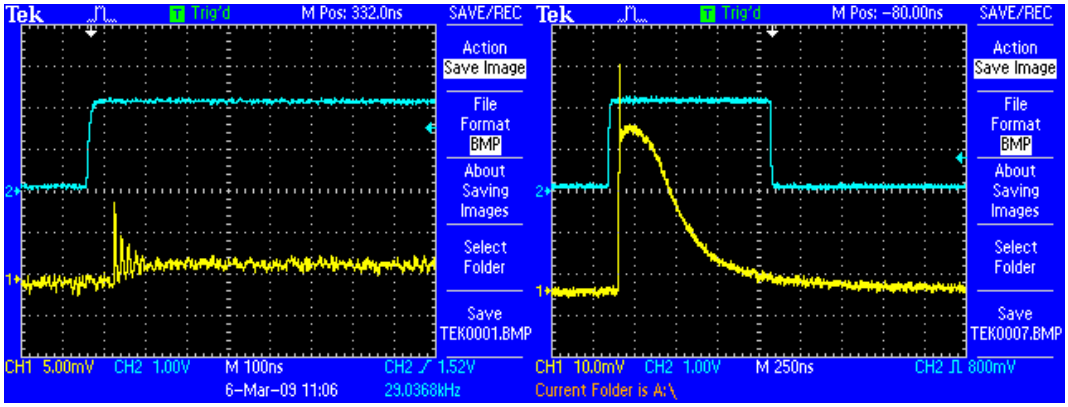

Figure 4.4. Typical responses of the Thorlabs DET110 silicon photodiode to a single optical pulse from the SuperK Compact light source (yellow traces). The capture was triggered using the synchronous TTL timing signal (blue traces). In the left image the photodiode output was 50-ohm terminated at the oscilloscope, while in the right image the output was 1M-ohm terminated. Images are screen captured from an oscilloscope.

Figure 4.4 shows the typical detector response to a single optical pulse from the Compact (yellow traces). The detector used to produce both left and right images is the same; the differences in pulse shape and temporal response are the result of altering the electrical termination of the detector at the oscilloscope and hence the RC time constant of the circuit. The RC time constant is a measure of the time required to charge a particular capacitor, *C*, to 63% of its nominal value via a resistance, *R*.

$$t \approx R \cdot C \qquad (2)$$

By default the input terminals on the oscilloscope have a resistance of 1M ohm and a capacitance of roughly 20 pF. This gives a time constant of approximately 20 µs meaning that signal variations occurring faster than this will not be accurately reproduced. The input impedance of the scope can be changed by adding a terminating resistor of appropriate value that connects the ground and signal wires. Adding a 50 ohm terminator results in a time constant of 1ns, meaning that the ability to see fast changes in the signal is limited by the response time of the photodiode. The effect of different termination resistances can be seen by comparing the left and right images in Figure 4.4.

4.3.4 Measurement of interference

Although we are unable to see the true shape of the output pulse from the Compact this does not affect the ability to measure properties of the source relating to interference, OCT and coherence. The voltage level of, for example, the peak of the pulses shown in Figure 4.4 is directly related to the intensity of light incident upon the photodiode. Adding neutral density filters to reduce the intensity at the detector causes the pulse peak to form at a lower voltage. From this it can be deduced that an interference pattern produced using the Compact will be detected by monitoring the (peak) amplitude of the pulse. The interference pattern can be scanned to produce a sequence of constructive and destructive interference fringes, resulting in the incident intensity and the detector pulse amplitude rising and falling in the expected sinusoidal fashion.

The Compact was connected to a free-space Michelson interferometer in an attempt to produce and detect an interference pattern. The resultant auto correlation should allow the coherence length of the source to be determined. Figure 4.5 (overleaf) shows a schematic of the interferometer. The fibre output from the Compact is collimated using a fibre collimator. The particular collimator used was designed for use in the near infrared part of the spectrum (1100 - 1600 nm) and so may have limited the spread of wavelengths within the interferometer.

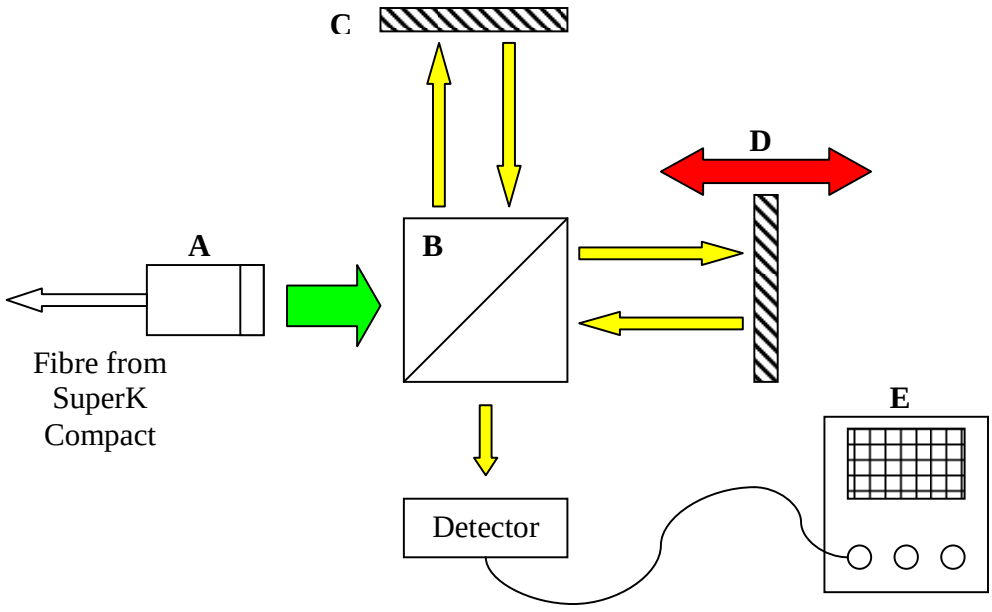

Figure 4.5. A schematic diagram of a free-space Michelson interferometer with motor-driven reference arm. Key: fibre collimator (A), cube beam splitter (B), fixed mirror (C), scanning mirror (D), oscilloscope (E).

Once collimated, the beam is centred upon one face of a cube beam splitter. The beam splits at the centre of the cube into two ‘arms’, both having approximately equal intensities. These two arms were both terminated with a mirror; one fixed in position axially, but with angular adjustment to allow beam steering, the other mounted on a motor-driven actuator to allow path length adjustments. The actuator was a PI piezo-electric device coupled to a Mercury DC motor controller, model C-860.10. This allowed the mirror (labelled ‘D’ in Figure 4.5) to be positioned axially with a precision of better than 10 nm [ref manual?]. The beam in each arm of the interferometer was reflected from

the terminating mirror and returned along its original path, the two beams recombining at the centre of the cube beam splitter. Here, the light is split again, with 50% being lost back towards the light source and 50% being directed towards the detector. A lens and neutral density filters were positioned before the detector to focus the collimated beam and reduce its intensity to avoid saturation.

The output of the detector was coupled (with appropriate termination) to a digital oscilloscope capable of recording images of waveforms and associated numerical data sets. Data files were saved to a compact flash memory card and then uploaded to a PC for analysis.

The method of capturing the interference pattern produced using the set-up in Figure 4.5 was as follows.

- The output from the detector was connected to the oscilloscope. The oscilloscope was triggered using the TTL synchronisation signal from the Compact. This allows one pulse from the Compact to be viewed at a time.
- The motor-driven mirror was moved to a position a few microns before the interference pattern was detected, determined by rough adjustments of the mirror.
- The mirror was then moved, step-by-step, through the interference pattern. At each position the pulse output was recorded as a comma separated value (CSV) file via the oscilloscope. This step scan procedure was repeated several times with different size steps ranging from 70 nm/step to 525 nm/step.
- The resulting CSV files were analysed using a MATLAB® (2006b, TheMathWorks, Natick, MA, USA) routine, described below.

The CSV files each contain data describing a single pulse from the Compact. For a particular step-size and detector combination the pulses all have essentially the same shape, with the sharp rising edge occurring at the same time point in each. The MATLAB routine uses the first CSV file in the sequence as a baseline with which to compare all others; the first CSV file will be a reasonable distance from any interference pattern and so will essentially have no intensity contribution due to interference. Once the baseline is established the routine takes the difference between a particular file and the baseline, and

then takes the average of a section during the pulse. This average value can then be considered as representative of any intensity contributions due to interference for the particular pulse. This routine is repeated for all CSV files in the scan sequence until a full set of intensity values versus scan position have been generated.

4.4 Results

The following graphs show the successful extraction of an interference signal from the CSV file sequence as described previously. The detector used in both cases was the Thorlabs PDA400 InGaAs photodetector (700-1800nm, 35ns rise time). Step sizes were set to 525nm in the first case (Figure 4.6) and 140nm in the second (Figure 4.7).

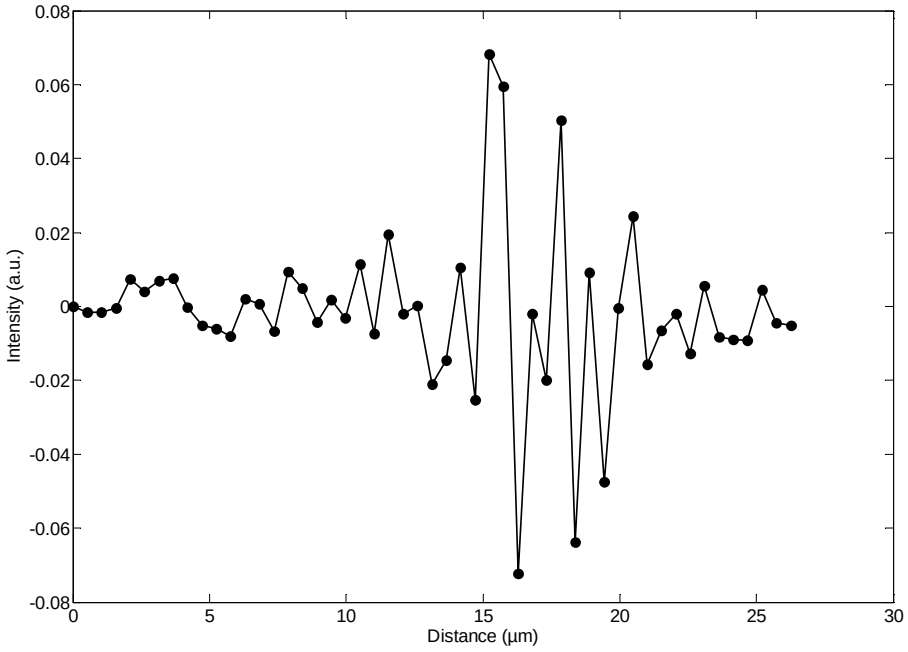

Figure 4.6. Graph showing the average intensities from 51 pulses of the Koheras SuperK Compact, versus interferometer mirror displacement as controlled by the PI piezo-electric actuator. An apparently under-sampled interferogram is visible, centred around 15 µm displacement. The displacement between pulses (step size) was 525nm.

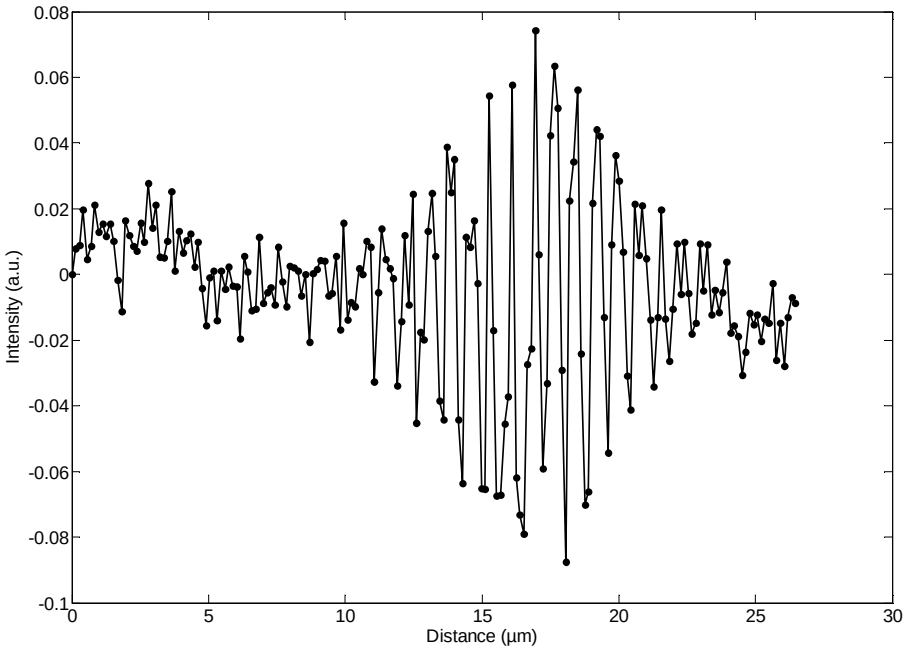

Figure 4.7. Graph showing the average intensities from 189 pulses of the Koheras SuperK Compact, versus interferometer mirror displacement as controlled by the PI piezo-electric actuator. An interferogram is clearly visible, centred around 17 µm displacement. The displacement between pulses (step size) was 140nm.

The interference signals in Figures 4.6 and 4.7 can be simply analysed to extract an estimate for the coherence length of the Compact within the confines of other experimental conditions that might restrict the available spectral bandwidth. The region of interest in both Figures occurs at distances of between 10 and 25 µm. The FWHM of the interference signal, and hence the coherence length, can be estimated in these regions by looking at the peak intensity, dividing it by two, and then finding the positions at which the interforgram reaches this intensity. This is found to be approximately 6 µm from the data shown in Figure 4.7.

The fringes observed in Figures 4.6 and 4.7 are under-sampled and severely affected by noise. The under-sampling is as a result of limited fine control over mirror positioning resulting in only a certain number of steps per unit length. The noise on the interferogram, including apparently shifting DC levels, is a result of the varying

amplitudes of the individual pulses used to construct the interferogram. The assumption that a fixed time point within the pulse maintains a constant amplitude appears to be false.

4.5 Analysis and discussion

Assuming that the photodetector (Thorlabs PDA400 InGaAs) is the main bandwidth-limiting factor in the system, then the range of useable wavelengths from the SuperK Compact is 700 to 1800 nm in the cases shown in Figures 4.6 and 4.7. This 1100nm range would theoretically allow for a coherence length of less than 2 µm, assuming a perfect Gaussian distribution of wavelengths about the central point. This can be calculated by using a central wavelength, λ, of 1250nm, and a bandwidth, $\Delta\lambda$, of 430 nm in Equation 2.14, giving a coherence length of ~1.6 µm. The bandwidth is calculated as the theoretical FWHM of a Gaussian distribution centred at 1250nm, and rising from/falling to zero at 700nm and 1800nm respectively.

The coherence length we observe is four times larger than this so we can conclude that the photodetector is not the main bandwidth-limiting factor in the system. Other optical components within the interferometer also impose some limitations. The beam-splitting cube used at the centre of the interferometer (Thorlabs BS012 10mm) is designed for use at wavelengths between 1100nm and 1600nm. This effectively both raises the central wavelength to 1350nm, and reduces the bandwidth to 170nm resulting in a longer coherence length of 4.7 µm.

Since it is known that the output intensity of the Compact as a function of wavelength is effectively flat, and is certainly not a Gaussian, this will also result in reducing the effective bandwidth available. The non-Gaussian nature of the input spectrum along with the shaping provided by optical components in the beam path will result in side lobes on the interference signal which obscure the “true” interference pattern and further add to the coherence length measured. The average power output of the Compact is also seen to fluctuate over time, resulting in significant noise on the constructed interference signal. All of the effects discussed show that the measured value for the coherence length of ~6 µm is to be expected in the described experimental situation.

An alternative method for determining the optical bandwidth provided by the Compact would have been to measure the spectrum directly using a spectrometer. This could be done directly at the output of the Compact, and also at the position of the detector, allowing the bandwidth-reducing effects of the optical set-up to be found. This was not done due to time constraints.

4.5.1 Practical issues

As well as determining the interferometric properties of the Compact light source, these experiments were also used to evaluate the practicalities of using the Compact in an OCT imaging system. The most obvious benefit of the Compact is that, since its output covers such a large spectral range, there is the possibility of using several different sections of spectrum to perform OCT-type measurements; although this would almost certainly require entirely independent sets of associated optical components/detectors etc. suited to the wavelengths in question. This was highlighted at the time of testing since only one interferometer (particularly the beamsplitter) was available and resulted in an inability to perform any measurements in the visible part of the spectrum. A second, practical point to note is that the Compact is a “turn-key” system meaning that it can be used and transported very easily with virtually no time required for set-up.

There are several areas which would make the Compact more difficult to use in an imaging scenario than, for example, a superluminescent diode. The output of the Compact is pulsed with a repetition rate of 25 kHz; resulting in significant periods of time when there is no light being emitted. If the output has pulse lengths of 1 ns at 25 kHz then the device is emitting light only 0.0025% of the time. For imaging, measurements would have to be synchronised with the Compact to ensure that signals are captured correctly. This can be done using the provided TTL synchronisation signal but it adds complications that other light sources do not. The Compact’s pulsed output also limits the rate at which data can be captured. Assuming that 1 pulse is required per pixel

to produce an image only 25,000 pixels can be captured per second; meaning that a 512 by 256 pixel image would take over 5 seconds to produce. This compares poorly with rates of 30 frames per second for most “fast” OCT imaging systems.

4.6 Conclusions

From testing and using the Koheras SuperK Compact over a short time the following conclusions can be drawn:

- The Compact is an extremely versatile light source due to the large spectral range and relative high intensity of its output. This can cause issues with other optical components however, which must be chosen wisely to suit the wavelength range required.
- In practical terms the Compact is portable and robust enough to be integrated into a portable OCT imaging system. It is a “turn-key” solution requiring minimal set-up.
- Measurements of the coherence length using a fairly standard component set yielded a value of approximately 6 µm in the near-infrared (1100-1800nm) wavelength range. This was limited mainly by the optical components involved, but also by the non-Gaussian nature of the spectral output.
- The Compact is limited to applications not requiring high-speed imaging due to its pulsed output’s relatively low repetition rate of 25 kHz. It would take several seconds to produce OCT images of a usable size. The pulsed output would also need to be synchronised with detection electronics to ensure that data would be read when light was returning from a sample.

References

[1] J. M. Schmitt, *IEEE Journal of Selected Topics in Quantum Electronics* **5** (4), 1205 (1999).

[2] B.E. Bouma and G.J. Tearney eds., *Handbook of Optical Coherence Tomography*, 1 ed. (Marcel Dekker, Inc., 2002).

[3] B. Bouma, G. J. Tearney, S. A. Boppart et al., *Optics Letters* **20** (13), 1486 (1995).

[4] W. Drexler, *Optics letters* **24** (17), 1221 (1999).

[5] I. Hartl, X. D. Li, C. Chudoba et al., *Opt. Lett.* **26** (9), 608 (2001).

[6] Pei-Lin Hsiung, Yu Chen, Tony Ko et al., *Opt. Express* **12** (22), 5287 (2004).

[7] *Koheras SuperK Extreme data sheet*. (Koheras A/S, 2008).

[8] *Koheras SuperK Compact data sheet*. (Koheras A/S, 2008).

Chapter 5

A skin and blood flow model for OCT

5.1 Introduction

The skin, and the blood flowing through it, can be used as a powerful indicator of systemic changes in diseases such as systemic sclerosis. While developing a custom OCT system (see Chapter 3) for imaging in clinical studies involving patients with such diseases, it was decided to produce a physical model, or phantom, in order to study the issues surrounding OCT imaging of skin and blood flow. This allows various imaging parameters to be studied, along with the problems associated with image analysis and interpretation.

A physical model in this case is known as a tissue phantom, since it aims to represent some (or all) of the characteristics of a particular tissue type. The aim in this case was to produce a phantom whose *optical* characteristics are closely matched with those of human skin and associated vasculature. This can then be imaged using a suitable OCT system. The phantom in this case is based around the light-scattering properties of binary mixtures; simple dilutions allow the optical properties of the liquid phantom to be fine-tuned over a wide range.

This modelling work was carried out, and completed, before the custom OCT system described in Chapter 3 was available. A commercially-available swept-source OCT system from Thorlabs (OCMP1300SS, Thorlabs, Inc.) was used in all of this work. This system is capable of producing Doppler OCT (DOCT) images of dynamic samples, as well as standard structural images of static objects. DOCT has been used in the past to

successfully study both phantoms, e.g. [1], and tissue, e.g. [2] or [3]. The Thorlabs DOCT system is described in some detail in this chapter.

5.2 The Thorlabs swept-source OCT system

5.2.1 System overview

As mentioned earlier, the OCT system used for imaging in this tissue modelling work is a commercially available unit made by Thorlabs (model number OCMP1300SS). The unit uses a swept-source laser as a broadband illumination source and operates in the Fourier domain.

Figure 5.1. A photograph of the Thorlabs swept-source OCT system; showing microscope-style sample arm with PC display and mouse/keyboard (top/second shelf), personal computer (third shelf), and swept-source laser (bottom shelf). Image taken from product manual [4].

Figure 5.1 shows a photograph of the Thorlabs swept-source OCT system (hereafter referred to as the "SS-OCT system"). The system consists of the swept-source laser, a microscope-style sample arm attachment, and a personal computer (PC). There is also a hand-held probe that can be swapped in for the microscope; although this is not shown in Figure 5.1, or used in this tissue modelling work.

The PC contains two data acquisition cards; one (high-speed) device for capturing the interference signals produced from the sample under test, and a second for control and synchronisation of the various scanning components required to produce a 2 or 3 dimensional image. Custom software provided by Thorlabs (version 2.1.7) controls all aspects of the system, from calibration and imaging parameters through to data capture and storage.

The SS-OCT system has an axial scan rate of 16 kHz (16,000 depth scans per second) allowing frame rates greater than 25 fps when 512 axial scans are used to produce one frame. The working distance for the microscope system is 50 mm and the objective lens has a x3 magnification. The swept-source laser has a central wavelength of 1325 nm with an optical bandwidth of 100 nm, resulting in a coherence length of approximately 7 µm. The system also has the capability to capture any induced Doppler shifts present in the interference signal from a sample under test. These are produced when imaging samples that have some dynamic (moving) component and are viewed as a separate image to the normal, structural information. A colour map is used to help interpret the degree of Doppler shift present.

5.2.2 The swept-source laser

A swept-source laser is a tuneable laser light source whose output wavelength is varied repetitively as a function of time; the optical output "sweeps" through a certain range of wavelengths. If an observer watches the output over one full sweep of the total wavelength range they will see all wavelength modes emitted one after the other, and it

will be as if the source has produced a broadband output over the duration of the sweep. One typical method of creating this type of light source is to use a semiconductor gain medium in conjunction with an external cavity, where a dispersive element such as a prism or diffraction grating is used to "tune" the output to a particular wavelength. A mechanical scanner, typically a resonant galvanometer or a piezo-electric device, is then used to continuously sweep through the tuneable range of the cavity. A typical example of this can be seen in Reference [5]. Another method of producing swept-source lasers is the ring cavity design incorporating Fourier-domain mode-locking (FDML) [6]. These are capable of much higher sweep rates (> 100 kHz) and work by synchronizing a tuneable filter with the round-trip flight time of light within a circular cavity.

The swept-source laser can be incorporated into an OCT system operating in the Fourier domain, with each sweep of the laser output ultimately producing one axial/depth scan. As with other Fourier domain techniques, the need for independent, mechanical, path-length scanning is eliminated. The advantages of such sources in an OCT environment are many, with the most obvious being the speed at which they are capable of scanning. Axial scan rates of many tens of kilohertz are easily achievable, yielding images of a useful size (512 by 512 pixels) at video frame rates. Extremely fast swept sources have also been produced with scan rates of 370,000 lines per second [7], allowing so-called "4-D OCT" imaging, where 3D volumes are captured at a rate of greater than 1 per second.

The Thorlabs swept-source laser provided as part of the DOCT system is an external cavity type. It uses an oscillating mirror in combination with a diffraction grating to produce the swept, pseudo-broadband output. The sweep rate is 16 kHz, producing an output with a bandwidth of 100 nm centred around 1325 nm. Optical connection to the output of the Thorlabs swept-source laser is by an FC/APC single-mode fibre. Various electrical connections for synchronization, and to provide a clock signal for data capture, are also available. These are described later in this chapter.

5.2.3 The DOCT system

The Thorlabs OCT system consists of 4 major parts: the swept-source laser, an interferometer, a personal computer with associated software and data capture devices, and the sample arm output device (either the microscope or the hand-held probe). Figure 5.2 shows a schematic diagram of the system including all major optical and electronic components.

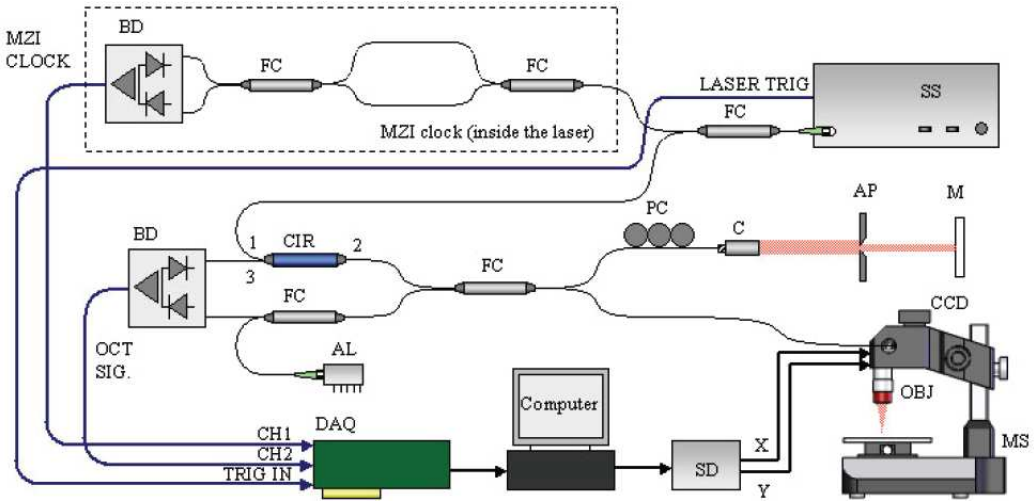

Figure 5.2. Schematic of the Thorlabs OCMP1300SS swept-source OCT/DOCT system. Key: MZI: Mach-Zehnder interferometer, SS: swept laser source, FC: fiber coupler, PC: polarization controller, CIR: circulator, AL: aiming laser, C: collimator, AP: adjustable pinhole variable attenuator, M: mirror, BD: balanced detector, DAQ: data acquisition board, SD: XY scanners driver, CCD: CCD camera, OBJ: objective, MS: microscope. This figure is taken from Thorlabs OCMP1300SS operating manual [4].

The swept-source unit contains the external cavity laser as described previously, along with a fibre-based Mach-Zehnder interferometer (MZI). This interferometer produces an electrical clock signal that is used to time the capture of individual image pixels, spacing them evenly in wavelength over the sweep of the laser output. A fibre beam splitter is used to pass approximately 0.5% of the total optical output power to the MZI in order to produce this clock signal.

Light from the swept-source laser is passed to the interferometer using an optical circulator (labelled CIR in Figure 5.2). Light coming into the circulator on port 1 exits the device on port 2, while light entering the circulator on port 2 exits via port 3. After passing through the circulator the light is split into two paths of equal power (50:50 ratio) using a fibre beam splitter; one path being a reference arm terminated in a static mirror, the other going via the microscope (including lateral scanning mechanism) to a sample under test. Light returning from both arms passes back through the fibre beam splitter and is incident on a pair of balanced detectors, producing the OCT signal. A visible laser diode for sample aiming purposes is also coupled into the interferometer.

The personal computer contains two digitiser cards. One of these (Alazartech) is an extremely fast (>100 MSamples/s, 14-bit resolution) device and is used to capture both the OCT signal from the interferometer and the MZI clock signal from the swept-source laser. The other digitiser (National Instruments) is used to drive the scanning mirrors in the microscope to provide lateral scanning for 2D (and 3D) imaging. The computer also synchronises the data acquisition process, ensuring that the laser output and the lateral scanners are at the appropriate point, in wavelength and space respectively, to correctly form images.

A microscope-style end piece is used in the sample arm for delivery of light onto the sample under test. It consists of a vertically adjustable scan head, comprising lateral scanning mirrors for imaging in both horizontal planes, and an achromatic objective lens with a focal length of 50 mm. The base of the microscope houses the interferometer and balanced photodiodes, meaning that only light from the swept-source laser is input to the microscope, along with electrical signals to control the scanning mirrors.

5.2.4 System software and DOCT imaging

The Thorlabs OCT system is provided with a software system allowing control over certain imaging parameters, including size, lateral resolution and contrast. It also allows simultaneous display of both structural OCT and Doppler OCT (DOCT) images. Static

OCT images are displayed in an 8-bit greyscale format, while DOCT images are displayed using a distinct colour map, detailed in Figure 5.3 below.

Figure 5.3. A representation of the colour map used to convert observed Doppler phase shifts into pixel values within the Thorlabs OCT system software. Static objects should appear black. The scale goes from cyan at –π radians phase shift, through blue, black, red and orange, to yellow at +π radians.

If Doppler phase shifts outside the range of ±π radians are observed, the colour map repeats; for example a phase shift of -2π radians would be displayed as black. It is therefore necessary to have some other knowledge about the behaviour of the moving parts of a sample in order to determine which parts are truly stationary and which are inducing a phase shift of integer multiples of 2π radians. The technique of converting from multiple phase-shift cycles to a velocity measurement is known as phase unwrapping.

The DOCT system software allows two important imaging parameters to be adjusted to improve Doppler OCT imaging; namely *x/z axis averaging* and *Doppler threshold*. The averaging can be applied in the depth (*z*) dimension and in the lateral (*x*) dimension independently. DOCT imaging is very susceptible to noise and external vibration; averaging over a number of pixels helps to negate these issues but reduces the spatial resolution of the DOCT image. Typically averaging is applied over 8-10 pixels to produce an acceptable image *in-vitro*. The Doppler threshold control provides a second method of noise abatement in DOCT imaging. This sets the lower level of induced phase shift at which the software will consider a data point for inclusion in the DOCT image. Pixels having a phase shift value below this threshold are displayed as stationary (black). The control effectively acts as a high-pass filter on the Doppler signal, removing much of the background noise caused by environmental vibrations.

Both Doppler and static OCT images can be saved in various formats, including bitmaps. Raw data can also be saved; either in the form of the Fourier-domain fringe signals as they come from the interferometer (as .FRG files, a proprietary format), or as the Fourier-transformed, 14-bit data before compression for display.

5.3 The tissue model

In order to create a tissue phantom for DOCT the optical properties of a material, such as scatter and absorption, need to be matched to those of the biological tissue we are attempting to model. In this case the tissues to be modelled are human skin and blood. The requirements for a suitable modelling material are that it should be readily available and that the parameters mentioned above are easily adjusted. Previous tissue modelling for OCT imaging has used various different materials including silica microspheres embedded in gelatin [8], and agar gel/intralipid mixtures [9].

Using liquids as the basis for a tissue phantom is extremely convenient as concentrations of scattering and absorbing particles are adjusted by simply diluting the mixture. One such suitable liquid is Intralipid solution; a polydisperse suspension of fat molecules, primarily soy bean oil, in water. As a bulk liquid Intralipid solution is an opaque, white solution very similar in appearance to milk. The clinical use of Intralipid solution is as an intravenous food substitute for patients who are unable to feed orally.

It has been shown that, in the wavelength range 100 – 2200 nm, a 2% (w/w) Intralipid solution is an acceptable tissue phantom for optical modelling of human skin [10]. There is only relatively limited data on specific optical properties of Intralipid solution though, particularly at the wavelengths used by the DOCT system (around 1300 nm). The mean cosine of scatter, g, has been reported as 0.7, absorption can be solely attributed to the suspending medium (water), and the scattering coefficients can be broadly assumed to be proportional to the concentration [11].

A 2% (w/w) Intralipid solution is a good optical phantom to represent human skin, but modelling blood flow within the skin needs more careful consideration.

5.3.1 Modelling blood flow

Unlike skin tissue, which is fairly homogeneous and static, blood flow consists of two components: the blood vessel in which the blood flows, and the liquid blood itself. The blood vessel can be modelled using any suitably-sized tube that is capable of carrying a liquid, and that is transparent to wavelengths around 1300 nm (realistic, since blood vessel walls are very thin). Many scientific glass manufacturers make a range of so-called "capillary tubes" with extremely small internal diameters. These are designed to be used as devices for measuring microscopic quantities of liquid in a laboratory environment. They are constructed from standard types of glass and so are suited for use in an optical phantom as blood vessels.

A range of glass capillary tubes were acquired for use in a blood flow phantom, details are in Table 5.1 below.

Glass capillary tubes	
Manufacturer	**Internal diameter (mm)**
Instrumentation Laboratory (Lexington, MA, USA)	1.4
Unknown manufacturer (acquired from colleague)	0.9
Drummond Scientific Co. (Broomall, PA, USA)	0.3
The Technical Glass Company (Haverhill, Suffolk, UK)	0.1
The Technical Glass Company (Haverhill, Suffolk, UK)	0.05

Table 5.1. Details of glass capillary tubes acquired for blood flow phantom.

Test DOCT images of substances to replicate liquid blood were performed in conjunction with the tubes detailed above. A suspension of 10 µm polystyrene microspheres in water was imaged, as well as flowing Intralipid solution. The microspheres were chosen due to

the particulate size being similar to that of red blood cells. A schematic of the imaging set-up is shown in Figure 5.4.

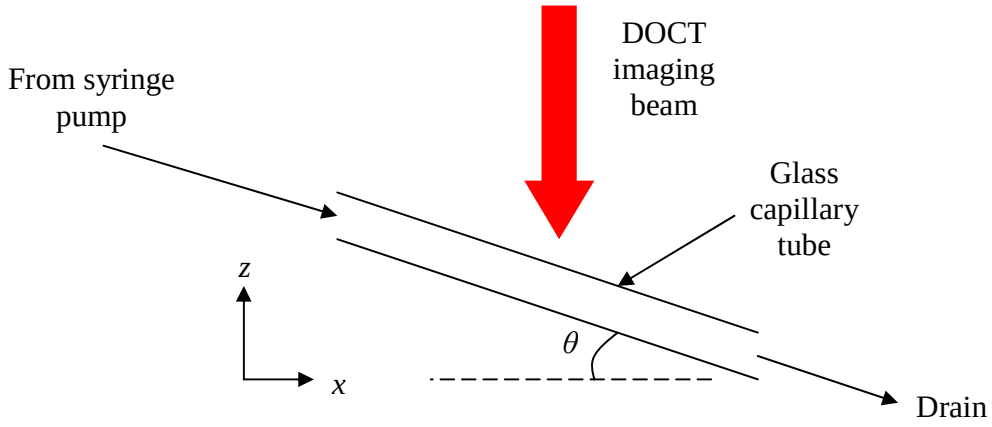

Figure 5.4. Schematic cross-sectional diagram of the flow test set-up. The angle between the glass capillary tube and the horizontal is labelled θ.

A syringe pump (model SP100i, World Precision Instruments, Inc.) was used to drive the test solutions through the tube. The syringe pump allows the flow rate to be adjusted from 0.1 ml/hour to over 200 ml/hour. The capillary tube was placed under the DOCT system microscope at an angle to the horizontal, θ, of 18°, ensuring that a component of the flow velocity is in the direction of the imaging beam. The value of 18° was used as this was the value allowed by the mechanical constraints of the set-up.

OCT and DOCT images of concentrated 10 µm microsphere solution, 50% (w/w) diluted 10 µm microsphere solution, and Intralipid solution flowing in a glass capillary tube surrounded by air, were recorded. These are shown in Figure 5.5.

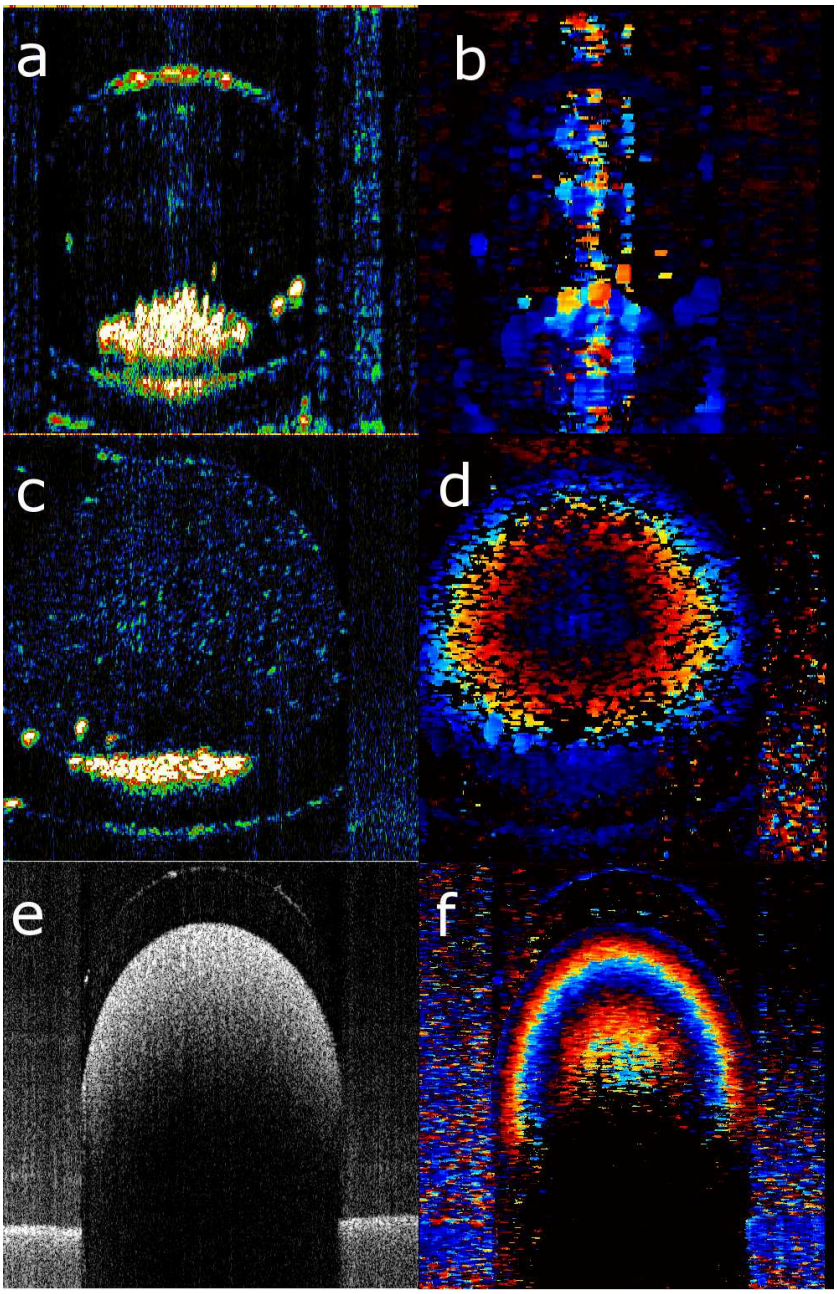

Figure 5.5. OCT and DOCT images of flow in glass capillary tubes: a) false colour OCT image of 10 µm polystyrene microspheres flowing at 10 ml/hour in a 0.3mm diameter tube, b) DOCT image of same; c) false colour OCT image of 50% diluted 10 µm polystyrene microsphere solution flowing at 10 ml/hour in a 0.3mm diameter tube, d) DOCT image of same; e) OCT image of 2% Intralipid solution flowing at 80ml/hour in a 1.4mm diameter tube, f) DOCT image of same.

For each solution tested, a range of flow rates were investigated and imaged. Flow rates from 1 ml/hour to over 100 ml/hour were imaged; these are excluded here for clarity. Assuming smooth, laminar flow, the velocity profile across the tube should be described by a parabola. The average velocity can be calculated by dividing the flow rate (after conversion from ml/hour to cubic metres per second) by the cross-sectional area of the tube. In laminar flow, the maximum velocity at the centre of the tube is twice this average velocity. For example: a 10 ml/hour flow in a 0.3mm diameter tube results in an average velocity of 4 cm/second, and therefore the velocity at the centre of the tube should be 8 cm/second.

There are a number of observations that can be made from the images in Figure 5.5. Firstly, the undiluted microsphere solution shows up some of the problems of using this as a flowing phantom material. The OCT image (Figure 5.5 a) shows a large amount of material clumped together at the bottom of the tube. This suggests that, at the relatively slow flow rates used, the microspheres do not stay in suspension and instead settle out due to gravity. This is reflected in the corresponding DOCT image (Figure 5.5 b) which gives very little useful information since there are few moving, scattering particles flowing uniformly through the tube.

The 50% (w/w) diluted microsphere solution shows some improvement. The OCT image (Figure 5.5 c) still shows a large amount of material apparently settled onto the bottom of the tube, although there appears to be some increased scatter throughout the tube cross-section. The DOCT image (Figure 5.5 d) now gives useful information regarding the flow profile of the liquid through the tube. The rings of colour suggest a radially-uniform phase shift is present, as expected if the liquid is flowing smoothly with a parabolic velocity profile.

Finally, the Intralipid solution (Figure 5.5 e) appears much more uniformly scattering than the polystyrene microsphere solutions. The corresponding DOCT image (Figure 5.5 f) shows a smooth Doppler phase map, although information is only returned up to the depth to which the light penetrates.

Although it would seem that the polystyrene microspheres should make a good blood flow phantom, there are a number of issues with them which exclude them from being used. The apparent clumping of the particulate matter even under flow conditions (which should encourage mixing) means that the concentration of the solution is unknown. This makes accurately tuning the optical properties of the solution almost impossible. Also, polystyrene microsphere solutions are extremely expensive; a small volume of 5 ml costs more than £100. This is due to the precision with which the spheres themselves are manufactured. These two issues taken together prevent the microsphere solutions being used in the tissue phantom.

Intralipid is a suitable alternative for a blood flow phantom, although it is not ideal. As mentioned earlier, there is little information on the optical properties of Intralipid in the wavelength range around 1300 nm; although it appears that a higher concentration than the 2% (w/w) required to model skin will be necessary in order to increase the scattering co-efficient towards that of blood (μ_s = 150 mm^{-1} at 850 nm) [12].

5.3.2 The skin and blood flow model

The final skin and blood flow model has been designed to use liquids as the tissue phantom components. Skin is represented using a 2% (w/w) Intralipid solution, and blood is represented using a second, more concentrated Intralipid solution. These were created by diluting Intralipid 20% (Fresenius Kabi AB) with distilled water to the appropriate concentration.

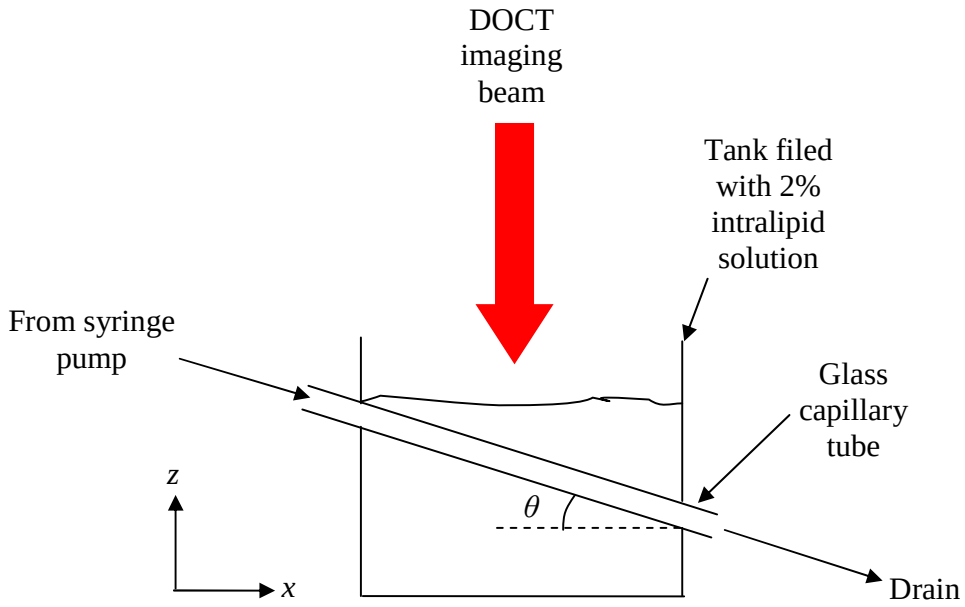

Figure 5.6. Schematic cross-section of the final tissue phantom. The angle θ is 18°.

Figure 5.6 shows a schematic cross-section of the final tissue phantom. As in the flow test set-up, the capillary tube runs at an angle of 18° to the horizontal. This ensures that there is a component of the flow velocity in the direction of the imaging beam. The tank used to hold the bulk liquid is a small plastic cube, approximately 3cm on each side, with one open face. The open face was oriented upwards and two holes were drilled in opposing sides of the tank to accommodate the capillary tube. The capillary tube was then fixed in place with epoxy resin and the tank was tested to see if it was watertight. Flexible hoses were used to connect the input from the syringe pump and the output to the drain. After filling the tank with 2% (w/w) Intralipid solution and setting the blood phantom flowing through the capillary tube, DOCT images can be recorded. By manoeuvring the imaging beam to different locations along the *x*-axis it is possible to image the tube at different depths in the bulk solution. Images of flow were recorded at flow rates ranging from 0 to 150 ml/hour and at depths of between 0 and 2 mm in 0.2mm steps for all capillary tube sizes.

5.4 Selected DOCT images of the tissue phantom

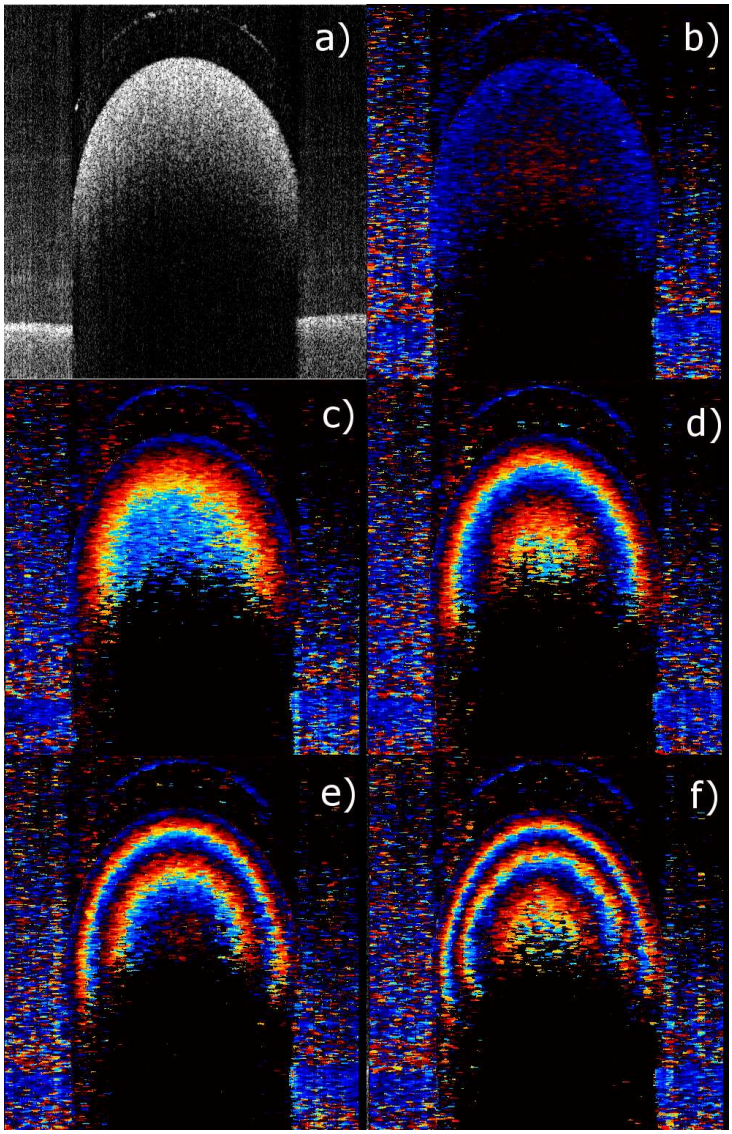

Figure 5.7. OCT/DOCT images of Intralipid solution flowing through a 1.4mm internal diameter capillary tube. The tank in the tissue phantom is not filled, so the tube is surrounded by air. Key: a) OCT image of the tube, b) to f) are DOCT images of the tube at flow rates of 10 ml/hour, 50 ml/hour, 80 ml/hour, 100 ml/hour, and 140 ml/hour respectively. All images are 3 mm by 3 mm, and 512 by 512 pixels.

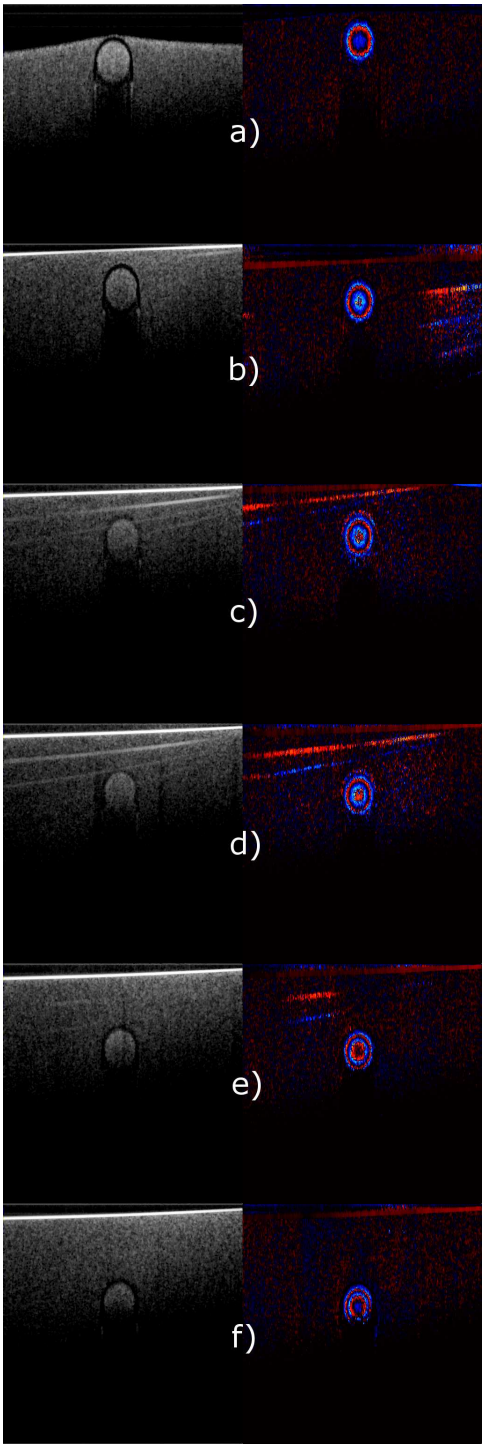

Figure 5.8. OCT (left) and DOCT (right) images of an 8 ml/hour flow of 2% (w/w) Intralipid solution in a 0.3mm internal diameter tube at varying depths. Depths are a) 0 mm, b) 0.2 mm, c) 0.4 mm, d) 0.6 mm, e) 0.8 mm, and f) 1 mm.

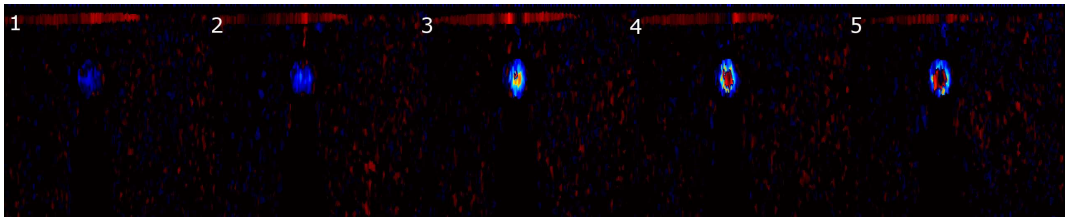

Figure 5.9. A sequence of five images, taken 10 seconds apart, showing a flow of 2.3 ml/hour being established in a 100 μm internal diameter capillary tube. The tube is suspended approximately 0.15 mm below the surface of a 2% (w/w) Intralipid solution. Images are 1 mm by 1 mm.

The images shown in Figures 5.7, 5.8 and 5.9 have been selected as representative of the various measurements available when using the liquid-based tissue phantom. These can then be analysed in order to test the DOCT system imaging capabilities relating to the tissue phantom.

5.5 Velocity profile extraction

For DOCT images that appear to display a clear Doppler profile, it is possible to extract a velocity profile from the image data. This was done using a custom MATLAB (The Mathworks, Inc.) routine, and was performed as described below.

Each DOCT cross-sectional image is loaded into the MATLAB environment, where a 10 pixel wide slice running vertically down through the centre of the tube is extracted. The RGB values of the pixels in this image slice are converted to phase shifts using the colour map in Figure 5.3. In images containing several cycles of the colour map, e.g. Figure 5.7 e), this results in a sinusoidal pattern of phase shifts. These are then cumulatively added to form a phase shift profile relative to the zero phase shifts at the edge of the tube.

These 10 phase shift profiles (from the 10 pixel wide strip) are averaged to produce a smoothed phase shift profile across the centre of the tube. If we make the assumption, as stated earlier, that the flow in the tubes is laminar, then we expect the velocity profile to be parabolic across the tube. The maximum velocity in the centre of the tube is twice the

average velocity calculated from the tube dimensions and flow rate. The phase shift profile is proportional to the velocity profile and so a simple scale factor can be used to convert from one to the other. The phase shift profile is converted to a velocity profile by multiplying all values by twice the average velocity, and then dividing by the relative phase-shift present at the centre of the tube.

This velocity profile extraction procedure is only possible in relatively large diameter capillary tubes, since in small tubes of less than a few hundred microns across the Doppler signal averaging limits the number of available pixels across the diameter of the tube.

5.5.1 Results

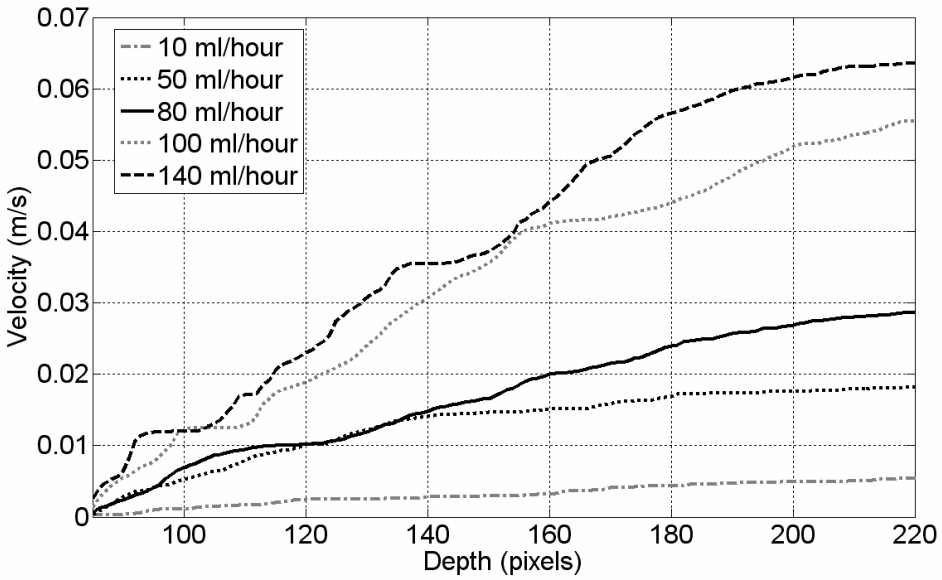

Figure 5.10. Velocity profiles extracted from the DOCT images in Figure 5.7. On the *x*-axis scale 1 pixel is equal to 7 µm.

5.6 Discussion of images and results

5.6.1 Images

Although the images in Figure 5.7 were recorded without the “skin” present in the tissue phantom, they highlight the DOCT system capability of capturing Doppler shift information from moving scattering media. As the flow is increased from 10 ml/hour up to 140 ml/hour the repeating cycles of $\pm\pi$ radians phase shift can clearly be seen building up in a ring-like pattern. The pattern is what would be expected in laminar (smooth) flow through a tube; the distance from the tube wall is what governs the flow speed. The large diameter (1.4mm) tube allows a large number of pixels to be included within the tube cross-section, resulting in a smooth velocity profile.

The images in Figure 5.8 involve all parameters in imaging the tissue phantom. The images are recorded at a constant flow rate of 8 ml/hour, which in the 0.3mm diameter tube used corresponds to an average velocity of just over 3 cm/second. Images of the tube submerged in 2% Intralipid solution to various depths are shown. As the tube gets deeper into the surrounding liquid, the static OCT image becomes less clear, and at 1 mm deep the tube is no longer fully resolved. Scattering from the surrounding medium reduces the amount of light reaching the “blood” flowing in the tube. This weakened signal can also be scattered on the return trip, further reducing the image quality at these depths. The DOCT images are perhaps less affected by the depth issue, although the Doppler signals are significantly weaker in this case anyway.

Figure 5.9 shows a time-lapse sequence of DOCT images of a flow of 2.3 ml/hour being established in a 0.1 mm diameter tube. The tube is submerged 0.15 mm into the tissue phantom. Although these tubes are closer to the size of blood vessels within the skin, they proved difficult to work with. Due to the extremely small cross sectional areas involved the tubes act like a flow restrictor on the syringe pump at flow rates significantly above the minimum possible, meaning that it would take several minutes for a constant flow

rate to become established within the tube. It is also likely that this results in the flow in the tubes being turbulent. However, DOCT images of flow are shown to be possible within these small tubes; changes in flow velocity are observed (as the flow is established), even if velocity profiles are unobtainable. The small number of pixels available within the tube cross-section further hampers the possible velocity measurements.

5.6.2 Velocity profiles

Figure 5.10 shows velocity profiles extracted from the DOCT images in Figure 5.7. These are approximately parabolic in shape, as expected for laminar flow, although a fit is not shown here for clarity. These show the information that can be extracted from a DOCT image of flow in a tube, although it is unlikely that such profiles could be as easily extracted from blood vessels *in vivo*. The large diameter of the capillary tubes used maximises the number of pixels available, resulting in the fairly smooth curves shown. The absence of a scattering medium surrounding the tube also undoubtedly helps the system to capture the Doppler signal.

5.7 Conclusions

A liquid-based skin and blood flow model for use in DOCT imaging has been designed and tested. Liquid-based media have an advantage over other tissue phantoms in that optical properties can be easily tuned by diluting the sample. Glass capillary tubes in conjunction with a syringe pump have been used to simulate blood flow through the phantom.

OCT and DOCT images were recorded at a range of flow rates and submersion depths, in various sizes of capillary tube. These images show the capabilities of DOCT to simultaneously image static and dynamic sample elements. Flow in the tissue phantom was observed in 0.1 mm tubes using the DOCT system, and changes in the flow as it was

established were also visible. Velocity profiles were extracted from DOCT images of flow in some of the larger tubes.

The purpose of constructing and imaging this tissue phantom was to learn about the factors affecting OCT and DOCT imaging of skin, and blood flow in small vessels within the skin. The model shows that it is possible to make quantitative measures of flow using DOCT imaging, but also demonstrates the difficulties encountered in imaging small vessels at non-trivial depths. The model employed here is a simplistic one regarding modelling blood flow. In vivo, blood flows in a pulsed fashion and there are other factors affecting the flow such as the elastic nature of vessel walls. This simplistic model merely aided the testing of the capabilities of OCT to image flow.

The work in this chapter was presented at the BiOS conference, part of Photonics West 2009 in San Jose, CA, USA. It was subsequently published as part of the conference proceedings [13].

The author would like to acknowledge the help of Nicolas Bensaid with some of the initial testing of the flow model design.

References

[1] R.K. Wang, *Advanced Biomedical and Clinical Diagnostic Systems II* **5330**, 208 (2004).

[2] J. A. Izatt, M. D. Kulkami, S. Yazdanfar et al., *Optics Letters* **22** (18), 1439 (1997).

[3] H. Li, B. A. Standish, A. Mariampillai et al., *Lasers Surg Med* **38** (8), 754 (2006).

[4] *Thorlabs swept source OCT system - operating manual*. (Thorlabs Inc., 2007).

[5] R. Huber, M. Wojtkowski, J. G. Fujimoto et al., *Optics Express* **13** (26) (2005).

[6] R. Huber, K. Taira, M. Wojtkowski et al., *Proceedings of SPIE--the international society for optical engineering* **5861**, PDA3 (2005).

[7] Robert Huber, Desmond C. Adler, and James G. Fujimoto, *Opt. Lett.* **31** (20), 2975 (2006).

[8] Kirk W. Gossage, Cynthia M. Smith, Elizabeth M. Kanter et al., *Advanced Biomedical and Clinical Diagnostic Systems II* **5318**, 140 (2004).

[9] T. Storen, A. Royset, L.O. Svaasand et al., *Journal of Biomedical Optics* **11** (1), 14017 (2006).

[10] T. L. Troy and S. N. Thennadil, *Journal of Biomedical Optics* **6** (2), 167 (2001).

[11] I. Driver, J. W. Feather, P. R. King et al., *Physics in Medicine & Biology* **34** (12), 1927 (1989).

[12] B.E. Bouma and G.J. Tearney eds., *Handbook of Optical Coherence Tomography*, 1 ed. (Marcel Dekker, Inc., 2002).

[13] Graham Dinsdale, Nicolas Bensaid, Andrea K. Murray et al., *Optical Coherence Tomography and Coherence Domain Optical Methods in Biomedicine XIII* **7168**, 71682G (2009).

Chapter 6

OCT imaging of neo-tropical tree frogs

6.1 An introduction to tree frog skin

It is well known that, other than a few notable exceptions, frogs have skin whose colour tends towards the green-brown area of the spectrum. That is, pigments within the frog skin reflect light in the visible part of the spectrum, with a peak somewhere between 500 and 600 nm. However, there are a few select species of neo-tropical tree frog whose skin has some additional optical properties that are of some interest.

These neo-tropical tree frogs (hereafter referred to simply as “tree frogs”) are mainly found in areas of rain forest in Central and South America, although some are also found in similar environments in parts of Australia. As the name suggests, tree frogs live on the leaves and branches of the trees that make up the rain forest. Tree frogs, like all amphibians, are cold-blooded and so rely on heat from external sources to regulate body temperature; they have been observed to bask in the sunlight available to them at the top of the rain forest canopy, and then to move into shade before they overheat and de-hydrate.

In 1973 Bagnara et al [1] discovered a new pigment extracted from the skin of the tree frog species *Agalychnis dacnicolor*. This was linked to an observed colour change phenomenon in this species whereby some frogs under typical daylight conditions will turn brown. Masking of the skin (i.e. shading it from illumination) caused it to return to the “normal” green appearance [2]. The conclusion that either the discovered pigment, or some other aspect of the skin, shows a photosensitive response means that the optical properties of the skin are adjusted based on illumination conditions. The new pigment

was ultimately identified as pterorhodin [3] and is also found in other species of tree frog of the *Phyllomedusinae* family. Figure 6.1 shows a mating pair of red-eyed tree frogs, whose skin contains the pterorhodin pigment.

Figure 6.1. Photograph of a mating pair of red-eyed tree frogs (*Agalychnis Calcarifer*). The female is the larger of the two animals. Image courtesy of Dr. Mark Dickinson.

Investigations into the optical properties bestowed on the frog skin by the pigment pterorhodin reveal that, in comparison to non-pterorhodin-containing species, the skin reflects very strongly in the near-infrared [4]. There are several possible advantages that this gives to the frogs that have the pterorhodin pigment. Firstly, it may improve the optical camouflage of the frogs, since the leaves of the trees and plants that the frogs live on also reflect strongly in the same wavelength ranges. However, it is not clear which predators the frog is camouflaging itself from, since there aren't any with NIR vision capabilities.

Secondly, the fact that the species with pterorhodin strongly reflect light in the NIR, coupled with the observed colour change behaviour appears to give these frogs a very useful advantage. Since at least the 1980s, a fungal infection (*Batrachochytrium*

dendrobatidis) has been threatening amphibians around the world, driving some rare species to extinction in the wild [5]. The fungus causes a disease called *chytridiomycosis*, which is usually fatal. It has been observed that tree frog species with the pterorhodin pigment are unusually resistant to this disease. One possible reason for this is their ability to bask in the sun for long periods thanks to the pterorhodin pigment which appears to prevent them from overheating by reflecting, rather than absorbing, the NIR wavelengths present in sunlight. The frogs are therefore able to raise skin temperatures without overheating the rest of the body. The fungus lives on the skin and is denatured by the elevated temperature.

6.2 Optical measurements of tree frog skin

Previous work in looking at the optical properties of tree frog skin has been carried out in collaboration with Mr. Andrew Gray, who is the curator of herpetology at The Manchester Museum. The museum has a large collection of captive-bred and wild-caught tree frogs of several different species, and holds an animal testing licence that allows non-invasive procedures to be carried out on live specimens. All experiments described in this chapter comply with the terms of this licence.

6.2.1 Reflection spectra and NIR photography

The work done previously produced reflection spectra of the tree-frog skin in an attempt to show the differences between pterorhodin-, and non-pterorhodin-containing species. Reflection spectra were produced using a CCD-based spectrometer in conjunction with a white light source. The spectrometers used were an Ocean Optics USB2000 model (wavelength range: 400 nm to 1000 nm, resolution: 1.5 nm) and an Ocean Optics NIRQuest model (wavelength range: 900 to 1700nm, resolution: 1.5 nm). Both spectrometers use a bifurcated, multi-mode fibre, allowing emission and collection of light to and from the sample using the same fibre. Proprietary software from Ocean

Optics allows spectra to be recorded essentially in real time, with the integration time variable from milliseconds to tens of seconds.

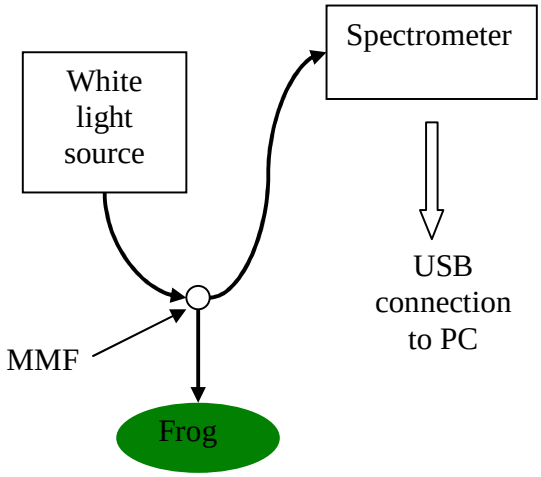

Figure 6.2. Schematic diagram of reflection spectra capture. MMF is the bifurcated, multi-mode fibre.

Figure 6.2 shows a schematic diagram of the reflection spectra capture process. Light from the source is directed, via the fibre, to the skin on the back of the frog. Reflected light is returned to the fibre and so to the spectrometer. A USB connection to a personal computer allows software to control the capture and display of the resulting data. The software allows the system response to be removed automatically from the captured data by recording a “white” spectrum (reflection from a uniform white material, e.g. white card) and a “dark” spectrum (light source off, sample end of fibre covered) before sample data capture. The system response was checked initially using a standard “white” reflector (Ocean Optics, WS-1), but no discernable difference was noted compared to using a white card and so this was used for all subsequent measurements.

In the wavelength range 400 nm to 1000 nm several species of frog were tested, along with a plant leaf that the frogs typically sit on. The resulting spectra are shown in Figure 6.3. Only one species of frog (*Agalychnis Callidryas*) was tested at the longer wavelength range; a composite spectrum from this is shown in Figure 6.4.

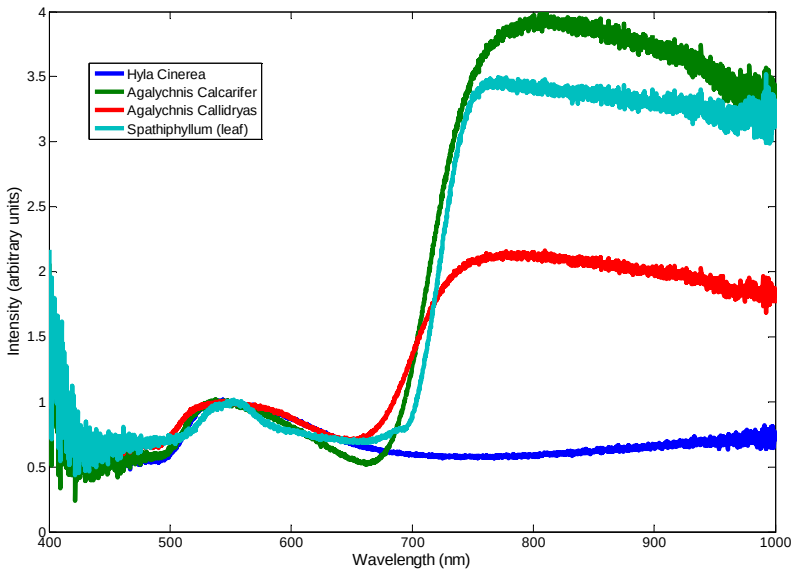

Figure 6.3. Reflection spectra of several frog species and a leaf. Data taken by Dr. Mark Dickinson and Mr. Andrew Gray.

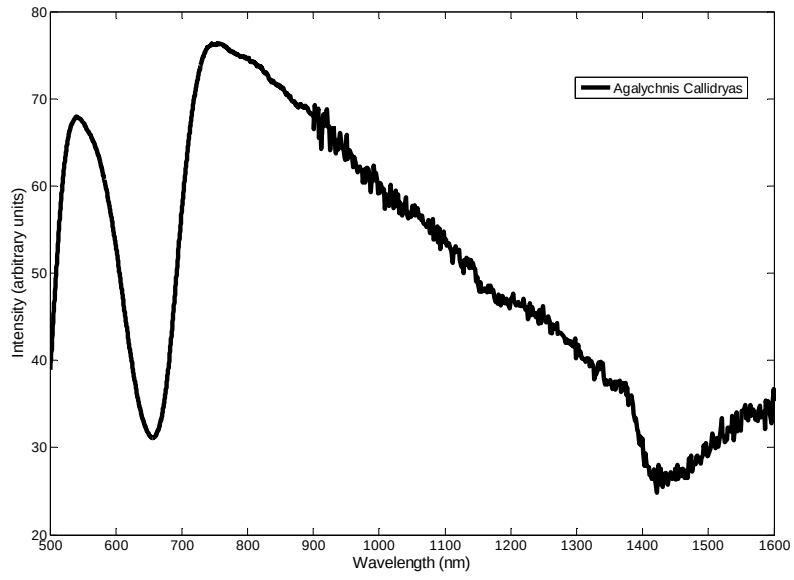

Figure 6.4.Composite reflection spectrum of the frog species *Agalychnis Callidryas* using data from both spectrometers. The data covers the wavelength range from 500 nm to 1600 nm.

The tree frog species *Agalychnis Calcarifer* and *Agalychnis Callidryas* both have the pigment pterorhodin in their skins, while *Hyla Cinerea* does not. The spectra in Figure 6.3 were re-scaled such that the green peaks at 550 nm were at the same intensity. The two species with pterorhodin clearly have much increased reflection of light in the near infrared between 700 nm and 1000 nm, when compared to that of the non-pterorhodin-containing frog *Hyla Cinerea*. The argument for pterorhodin being used for camouflage is supported by these results, since the leaf specimen displays a broadly similar reflection profile to those of the pterorhodin-containing frogs.

Figure 6.4 shows a composite reflection spectrum; data from both spectrometers has been spliced together to show the reflection properties for the *Agalychnis Callidryas* species of tree frog in the wavelength range 500 nm to 1600 nm. Data at the longer wavelengths show that the reflectivity peak apparently due to pterorhodin is not sustained into the near-infrared range, and has disappeared by approximately 1400 nm.

Figure 6.5. Near-infrared photographs of frogs sitting on leaves. The pterorhodin-containing frog is on the left, while the frog without pterorhodin is on the right. Photographs taken by Dr. Mark Dickinson and Mr. Andrew Gray.

The camouflage argument is further supported when comparing near-infrared photographs of frogs with and without pterorhodin, as shown in Figure 6.5 above. The non-pterorhodin frog clearly stands out, since it is reflecting a much smaller fraction of the light than the surrounding leaf. A 780 nm LED was the sole source of illumination for

these images; this falls within the high reflectivity region of the pterorhodin spectrum, as previously shown in Figure 6.3

These results appear to confirm those from the literature suggesting that tree frog species having the pigment pterorhodin in their skin reflect a much greater proportion of near-infrared light than those without the pigment.

6.3 OCT imaging of frog skin

Although reflection spectra provide some information relating to the properties of tree frog skin, they do not give any information about *where* in the skin the reflection is coming from. OCT imaging should allow access to depth-resolved information from the various layers that make up the frog skin. Layers that reflect or backscatter relatively large proportions of the incoming light will appear brighter than those that do not. If the pigment pterorhodin is contained within a particular skin layer in those species that possess it, then that layer will be relatively brighter than corresponding layers in non-pterorhodin-containing species.

6.3.1 Wavelength considerations

Particular consideration must be given to the imaging wavelength if the location of the pterorhodin pigment within the skin is to be found. Observations by the author as part of an undergraduate project seemed to suggest that the reflection of near-infrared light by frogs with pterorhodin tailed off at wavelengths around 1300 to 1400 nm, and these are born out by the spectrum shown previously in Figure 6.4. The OCT imaging wavelength should therefore be chosen to be in the range 700 nm to 1300 nm, if there is to be a significant, detectable differential between the two frog groups.

6.3.2 OCT imaging systems

Two commercial OCT imaging systems were available for this study, both made by Thorlabs. Selected system parameters are detailed in the Table 6.1 below.

OCT imaging systems – select parameters		
Parameter	Thorlabs OCMP1300SS	Thorlabs SDOCT930
Central wavelength	1325 nm	930 nm
Spectral bandwidth	100 nm	100 nm
Resolution (air)	~7 µm	~6 µm
OCT system type	Swept source	Spectral domain
Frame rate	Video frame rate capable (25 fps)	~ 5 fps

Table 6.1. Selected parameters of available OCT imaging systems, taken from [6] and [7] .

The Thorlabs OCMP1300SS swept-source OCT imaging system is described in detail in Chapter 4. For the imaging of frog skin the hand-held probe was used, rather than the microscope attachment used previously.

The Thorlabs SDOCT930 system uses a superluminescent diode as a source of broadband light. The system works in the spectral domain, and captures interference data by means of a multi-detector array and a dispersive element on the interferometer output. Such systems were described in Chapter 2. The system consists of a personal computer connected to a device housing the light source, fibre-based interferometer, and detector array, which is then coupled to the hand-held probe. The probe also contains a visible light camera that images on axis with the OCT image, providing simultaneous video and OCT images of the surface under test. This system was provided to us on a loan basis by Thorlabs, Inc.

6.3.3 The imaging process

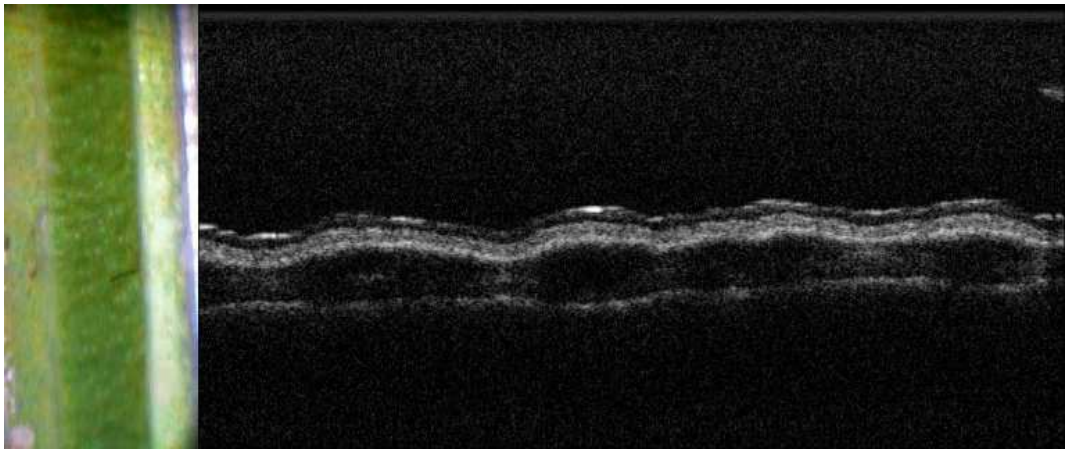

Figure 6.6. Composite of still video image (left) and OCT image (right) from the Thorlabs 930 nm system.

Imaging with each of the two systems was a very similar process. The frogs were held gently in front of their back legs to prevent them moving, and then the imaging probe was held to the skin. Ten images were recorded with each system on each frog species. The 930 nm system also recorded simultaneous, colour video stills of the skin surface.

An example of both the OCT and video images available from the Thorlabs 930 nm system is shown in Figure 6.6, above. The OCT image is taken along the vertical axis running down the centre of the video still image, and is 3 mm wide by 3 mm deep.

Imaging with the two systems was performed on separate occasions; resulting in non-identical areas of skin being imaged. Also, tree frog skin is fairly loose-fitting on the animal; it is not attached to the underlying tissue across the entire body. This can manifest in pockets or "holes" appearing under the skin, where a crease has formed or the skin is not pulled taut. It was hoped that imaging several frogs of each species would allow comparable images to be produced.

6.4 Results

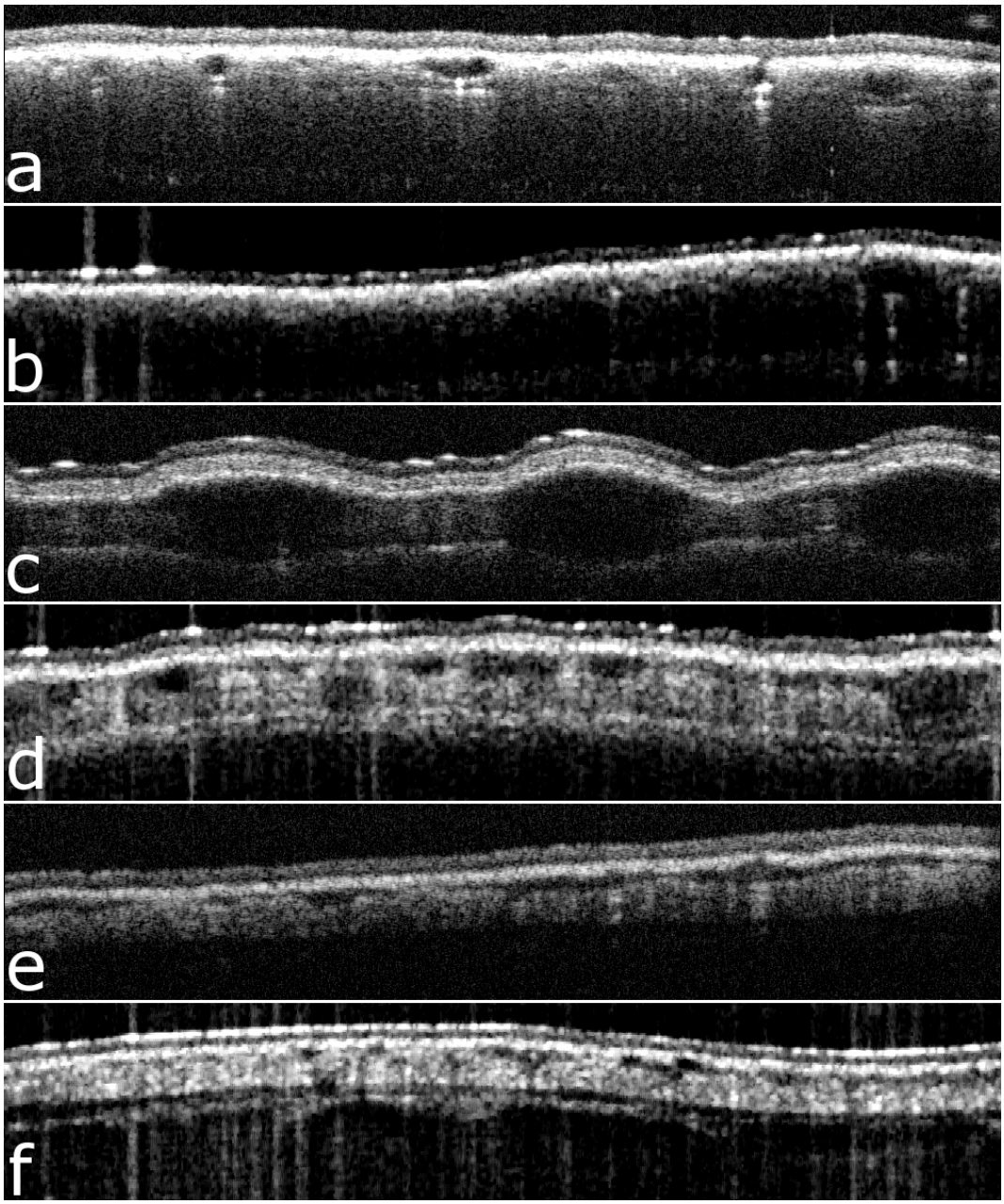

Figure 6.7. Examples of OCT images of frog skin, taken with both 930 nm and 1300 nm systems. *Agalychnis Calcarifer*: a) 930 nm, b) 1300 nm. *Agalychnis Callidryas*: c) 930 nm, d) 1300 nm. *Hyla Cinerea*: e) 930 nm, f) 1300 nm. All images are cropped to 3 mm wide by 1.2 mm deep.

Figure 6.7 shows OCT images, taken with both systems, of three frog species; namely *Agalychnis Calcarifer*, *Aglaychnis Callidryas* and *Hyla Cinerea*. The first two of these (*A. Calcarifer* and *A. Callidryas*) are known to contain the pterorhodin pigment, while *Hyla Cinerea* does not.

6.4.1 Image analysis

Images taken with both systems were analysed in an identical way. First, the images were loaded into Matlab (The Mathworks, Inc.), and then a vertical section through the image was extracted. This was done in a region of the image were the layers of skin were reasonably horizontal, so that averaging across the vertical lines of pixels does not blur or smear the boundaries. This averaged block was made as wide (horizontally) as possible, in order to reduce image noise.

Once the vertical section is selected it is then averaged to produce a single "A-scan", representing an average depth profile of the frog skin. The depth profile can be considered as a plot of interference signal intensity versus depth. The reason for producing depth profiles is as follows: if the pterorhodin pigment is constrained to a particular layer in those frogs that contain it, then the depth profile should have a tall peak (high intensity) at the depth corresponding to the layer. Before commencing imaging it was believed that the 930 nm imaging system would be more likely to show this effect, since the frogs with pterorhodin have high reflectivity in that wavelength region. The 1300 nm wavelength may fall outside the region of high-reflectivity due to pterorhodin (as shown in Figure 6.4), and therefore may not show up any bright layers.

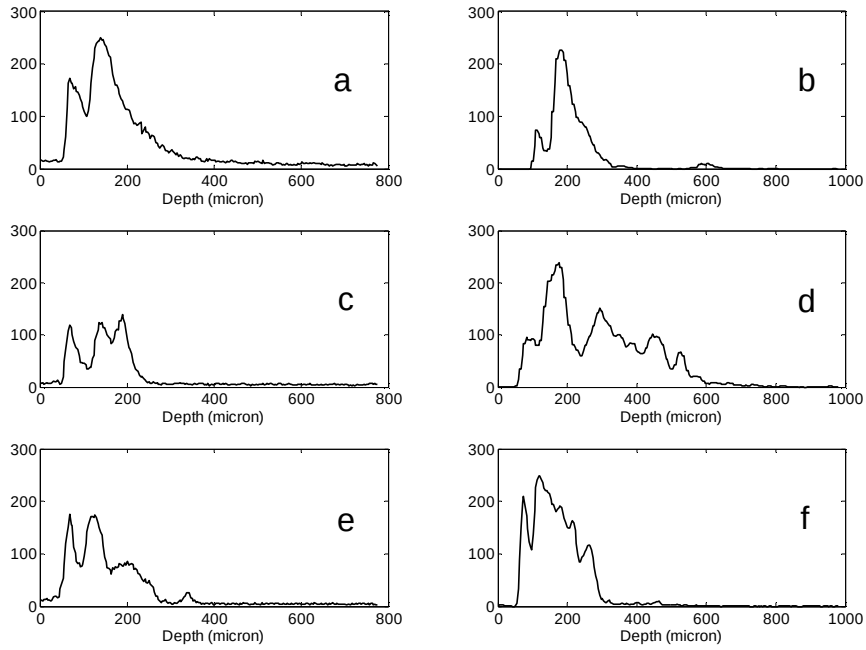

Figure 6.8. Averaged depth profiles of the skin of various frog species, taken from OCT images at 930 nm and 1300 nm. The *y*-axis on each profile is the pixel intensity in arbitrary units. Key: *Agalychnis Calcarifer*: a) 930 nm, b) 1300 nm. *Agalychnis Callidryas*: c) 930 nm, d) 1300 nm. *Hyla Cinerea*: e) 930 nm, f) 1300 nm

Figure 6.8 shows average depth profiles extracted from the OCT images of three frog species shown in Figure 6.7. Since images from both systems are recorded in 8-bit greyscale, the maximum possible intensity (in arbitrary units) in all cases is 255.

The individual profiles provide some clues as to which layers of the frog skin reflect or backscatter the highest proportion of the incident light. However, it seems that inter-species comparison, or even comparisons between frogs of the same species are impossible using data from the images taken. This is explained further in the next section.

6.4.2 Discussion

The depth profiles shown in Figure 6.8 do show the distribution of backscattering locations as a function of depth within the tree frog skin. For example, the second layer in

the 930 nm *Agalychnis Calcarifer* image (Figure 6.7 a) appears to be the brightest, and this is confirmed by the corresponding depth profile. Comparison between the depth profiles extracted at the two wavelengths show common features, with peaks and troughs appearing at similar depth locations. The relative intensities of two peaks within a profile may differ between the 2 wavelengths, and this could warrant further investigation.

The major flaw with the images as captured is related to the intensity scaling of interference data by the two imaging systems. Both systems included a calibration routine whereby the brightest signal from a sample is adjusted such that it corresponds to the highest white level in the image (255 for an 8-bit image). This routine was performed at the start of each imaging session, as is normal protocol for OCT imaging with either system. There are simply too many factors that can produce massive variability in this maximum brightness value to be able to extract meaningful data on relative intensities. Factors affecting the maximum brightness include: light source instability, wetness of frog skin sample and natural variability of the frog population. The result of this is that the images of different frogs cannot be compared in terms of intensity, since they are not related by any absolute scale.

6.5 Conclusions

The OCT images of tree frog skin taken here may be the first time this technique has been used to investigate these animals. The images show that OCT is a suitable technique for imaging the skin of tree frogs, showing skin structure in detail at high resolution.

Unfortunately, the two commercial OCT systems used were unable to provide an absolute intensity scale for the images captured; meaning that cross-image comparison was impossible. The aim of this imaging experiment was to attempt to see if the pigment pterorhodin was isolated in a particular layer of the skin, which would manifest as a brighter layer in frogs containing the pigment when compared to those not containing the pigment. Without an absolute intensity scale it cannot be determined whether a particular

layer in one image is actually brighter than that in another image, or whether one image is simply brighter *overall*.

To negate this problem in future work, imaging of all samples requiring comparison on the basis of brightness or intensity should be performed at the same time, without re-calibrating the system software or turning off the system between images.

References

[1] Joseph T. Bagnara, John D. Taylor, and Giuseppe Prota, *Science* **182** (4116), 1034 (1973).

[2] T. Iga and J. T. Bagnara, *Journal of Experimental Zoology* **192** (3), 331 (1975).

[3] G. Misuraca, G. Prota, J. T. Bagnara et al., *Comparative Biochemistry and Physiology Part B: Comparative Biochemistry* **57** (1), 41 (1977).

[4] P. A. Schwalm, P. H. Starrett, and R. W. McDiarmid, *Science* **196** (4295), 1225 (1977).

[5] Matthew C. Fisher, Trenton W. J. Garner, and Susan F. Walker, *Annual Review of Microbiology* **63** (1), 291 (2009).

[6] *Thorlabs swept source OCT system - operating manual*. (Thorlabs Inc., 2007).

[7] *Thorlabs SD-OCT spectral radar system - operating manual*. (Thorlabs Inc., 2008).

Chapter 7

A pilot study of non invasive imaging of skin – ultrasound versus OCT

7.1 Introduction

One of the major motivating factors for this work is provided by the requirement to investigate various skin connective tissue diseases. An interdisciplinary collaboration with the Dermatological Sciences and Rheumatology research groups at Salford Royal Hospital provides access to patient groups with conditions including systemic sclerosis and primary Raynaud's phenomenon. Systemic sclerosis (SSc) is a multi-system connective tissue disease characterised by tissue fibrosis, particularly involving thickening of the skin, and vascular damage. Primary Raynaud's phenomenon (PRP) is an idiopathic condition (one with no underlying cause) involving colour changes in the fingers brought on by cold conditions or stress. Around 90% of patients with SSc have Raynaud's phenomenon as a secondary condition. Patients with PRP rarely go on to develop SSc, and almost never have systemic changes or other underlying problems. The common link between these conditions is that they affect the cutaneous microcirculation in some way, usually involving impaired or irregular blood flow through the tiny capillaries within the skin tissue.

Previous studies have investigated these conditions using techniques including nailfold capillaroscopy, laser Doppler imaging (LDI) and thermographic imaging [1]. Nailfold capillaroscopy provides high resolution images of capillaries parallel to the skin surface within the fingers, allowing assessment of abnormal vessel structure. The LDI technique provides functional information relating to blood flow velocity, but the results are

dependent on the volume illuminated, which is always estimated. Optical coherence tomography imaging and high frequency ultrasound imaging can also be used to provide structural images of skin tissue. These, together with information from LDI and nailfold capillaroscopy images, can be used as a series of tools for assessing disease severity, progression and treatment response.

This study aims to show that OCT imaging is suitable for use in imaging *in vivo* skin in patients. This is done by comparison with already established imaging techniques; namely high-frequency ultrasound (HFUS), nailfold capillaroscopy and LDI. OCT, HFUS, and nailfold capillaroscopy were used to assess structural differences between patients and healthy controls, while LDI was used to assess functional differences between the same groups.

7.2 Imaging Techniques

7.2.1 Nailfold capillaroscopy

This is a well-established imaging technique that allows structural changes in the microvasculature to be assessed and recorded [2]. It relies on the fact that capillaries in the finger at the point were the skin meets the nail bed (the cuticle) lie parallel to the surface rather than their usual perpendicular orientation. These capillaries are only a few tenths of a millimetre below the surface and so can be imaged using a microscope. In healthy patients the capillaries are generally uniform in size, shape and distribution density. In patients with PRP, SSc and similar conditions the capillaries tend to be much less uniform, with wide variations in vessel thickness and shape. Also, the capillaries tend to be more sparsely distributed in patient groups when compared with control groups.

Nailfold capilaroscopy images are captured using a CCD camera. After averaging and composite image formation using custom software, measurement of the aforementioned geometrical factors can be performed to produce values suitable for statistical analysis.

7.2.2 Laser Doppler imaging (LDI)

LDI is another imaging technique commonly used in assessing changes in the microvasculature [3]. This technique records the Doppler shift induced in a laser beam scattered from moving particles (typically red blood cells) within the flowing blood. The observed Doppler shift is influenced by the volume of tissue illuminated, as well as the velocity of scattering particles within it. The penetration of light into tissue determines this volume illuminated, which is highly dependent on wavelength. Using lasers of different wavelengths allows Doppler shifts from different depth "windows" to be observed. Images are typically built up by raster scanning a single spot across the surface of the subject.

An LDI system from Moor Instruments Ltd. with a built-in red laser source at 633nm was used for this study. This was previously modified by the addition of a second laser source at 532nm; allowing simultaneous dual wavelength imaging. The green laser wavelength of 532nm does not penetrate as far into skin tissue as the red laser, so Doppler shifts from two depth ranges are recorded.

7.2.3 OCT imaging

OCT is the imaging method under test in this study. It has previously been used to look at the structure (and function) of various tissue types in a variety of in vivo and in vitro situations. Penetration of the broadband light sources used in OCT into skin tissue is typically around 1mm; this should allow the boundaries between the uppermost layers to be imaged, and so the layer thicknesses measured. Depth resolutions of between 5 and

10 µm are achievable, with lateral resolutions at a similar level. Images can be recorded at 25 fps for 512 by 512 pixel images.

The OCT system used in this study was kindly loaned to us by the Wellcome Trust Clinical Research Facility, Manchester, UK. It is a Thorlabs, Inc. system (Thorlabs OCM1300SS) using a swept source laser with a central wavelength of 1325 nm and a bandwidth of 100 nm [4].

7.2.4 High-frequency ultrasound

This imaging technique uses sound waves with megahertz frequencies to produce images of reflecting/scattering boundaries within a subject. Sound waves are emitted from a transducer (typically an electrically-stimulated piezo crystal) and are incident upon a tissue surface. At boundaries within the tissue a proportion of the sound is reflected back to the transducer; the time of flight of the sound waves is then recorded. Unlike the familiar ultrasound systems used in, for example, an obstetric environment, the high frequency of the sound waves used here limits penetration into soft tissue to approximately 20mm. However, this more than adequately encompasses the typical depth of the tissue layer boundaries within the skin. At a frequency of 20 MHz, the image depth resolution is approximately 50 µm; dependent on the speed of sound waves within the tissue of interest. Two-dimensional images (depth and width) are formed by laterally scanning the ultrasound transducer across the surface of the subject. High-frequency ultrasound has previously been used to assess skin thickening in patients SSc, in comparison with a control group [5].

The high-frequency ultrasound system used in this study has been kindly loaned to us by Longport Inc. (Reading, UK). It is a Longport EPISCAN I-200 system [6], operating at 20 MHz.

7.3 Patients and Methods

7.3.1 Patients

The study involves two groups; one group of 20 patients with SSc, and a second group of 20 healthy control subjects. The patient group consisted of 4 men and 16 women; with a median age of 61 years (range 28 to 78), all with a confirmed diagnosis of systemic sclerosis as assessed by a consultant rheumatologist. There were 3 out of the total of 20 who identified themselves as a smoker.

The control group consisted of 6 men and 14 women; the median age of this group was 49 years (range 32 to 70). There was 1 subject in the control group who identified themselves as a smoker.

All participants gave written, informed consent before taking part in the study; having had access to an information sheet and time to ask questions before signing up. The study was approved by the Stockport Research Ethics Committee (study number 08/H1012/74).

7.3.2 Protocol

The study consisted of one visit per subject, lasting approximately one hour. Participants were asked to refrain from nicotine and caffeine for a minimum of 4 hours before attending for the study as these can have a detectable effect on blood flow in the microvasculature. On arrival, subjects were acclimatised in a temperature-controlled laboratory at 23°C for 20 minutes. While acclimatising, the necessary paperwork, including consent forms and brief questions relating to current medication and past medical history, was completed.

After 20 minutes of acclimatisation, the participants first underwent nailfold capillaroscopy imaging (VCS, KK Technology, Devon, UK; modified) of the ring finger on the non-dominant hand. Olive oil is used on the skin to improve image quality by acting as an index-matching medium and also removing/smoothing texture on the skin surface, resulting in reduced diffuse reflections. The captured images are greyscale, with a magnification of 300x allowing individual capillary shape and structure to be viewed. A green LED illumination source was used to increase contrast between red blood cells within the capillaries, and the surrounding skin tissue. Each frame is an average of 16 captured frames; the averaging allows the shape of blood vessels to become apparent as high-contrast red blood cells move through the vessel during the imaging sequence. Frames are captured at overlapping locations to allow the entire nail bed across the finger to be imaged. A composite image was then formed by stitching (via image registration) the individual frames together using custom software.

Following nailfold imaging the participants immediately underwent dual-wavelength laser Doppler imaging (Moor LDI-vr, Moor Instruments, Axminster, UK) of the dorsal aspect of the non-dominant hand. This is performed with all room lights off to avoid interference from 100 Hz optical noise. Subjects and researchers wear laser safety goggles in compliance with local laser safety rules for the LDI equipment. The imaging process is performed by raster scanning the dual laser beams across the tissue under test and then capturing the back-scattered, Doppler-shifted light. Imaging an area encompassing a whole hand takes approximately 5 minutes, during which time the participant must remain completely still.

Once the LDI procedure was complete the subject was then imaged using a commercially-available OCT system (Thorlabs Ltd., OCM1300SS) which uses a swept laser as a source of partially coherent broadband light (1300 nm central wavelength, 100 nm bandwidth). The system has a hand-held probe which makes imaging extremely fast and efficient. At each imaging site 10 frames of 1024 by 512 pixels were recorded with dimensions of 1mm wide and 3mm deep. The recording of multiple frames was done to ensure there were at least 1 or 2 frames with a good quality image at each site.

Body sites imaged included: distal and proximal non-dominant ring finger (both dorsal and palmar aspects), dorsum of the hand, dorsal and volar aspects of the forearm and upper arm, and the chest over the breast bone. This makes a total of 10 body sites. Care was taken to ensure that the upper surface of the skin was as horizontal as possible in all images to aid in later analysis.

Following OCT imaging the subject was further imaged using a high-frequency ultrasound imaging system (Episcan I-200, Longport Inc.). This was performed at the same set of body sites as for the OCT imaging technique. At each imaging site 16 frames were recorded; each frame being 512 by 1024 pixels with physical dimensions of 15 mm wide by 22 mm deep. Ultrasound imaging was performed last to ensure that the use of ultrasound gel did not have any influence on the results recorded with the other techniques.

As imaging was performed, a so-called “skin score” was also recorded at each body site location. This is a manual method of assessing skin elasticity and flexibility using a pinch test.

7.4 Images and analysis

The images in Figure 7.1 are examples of those taken during the study.

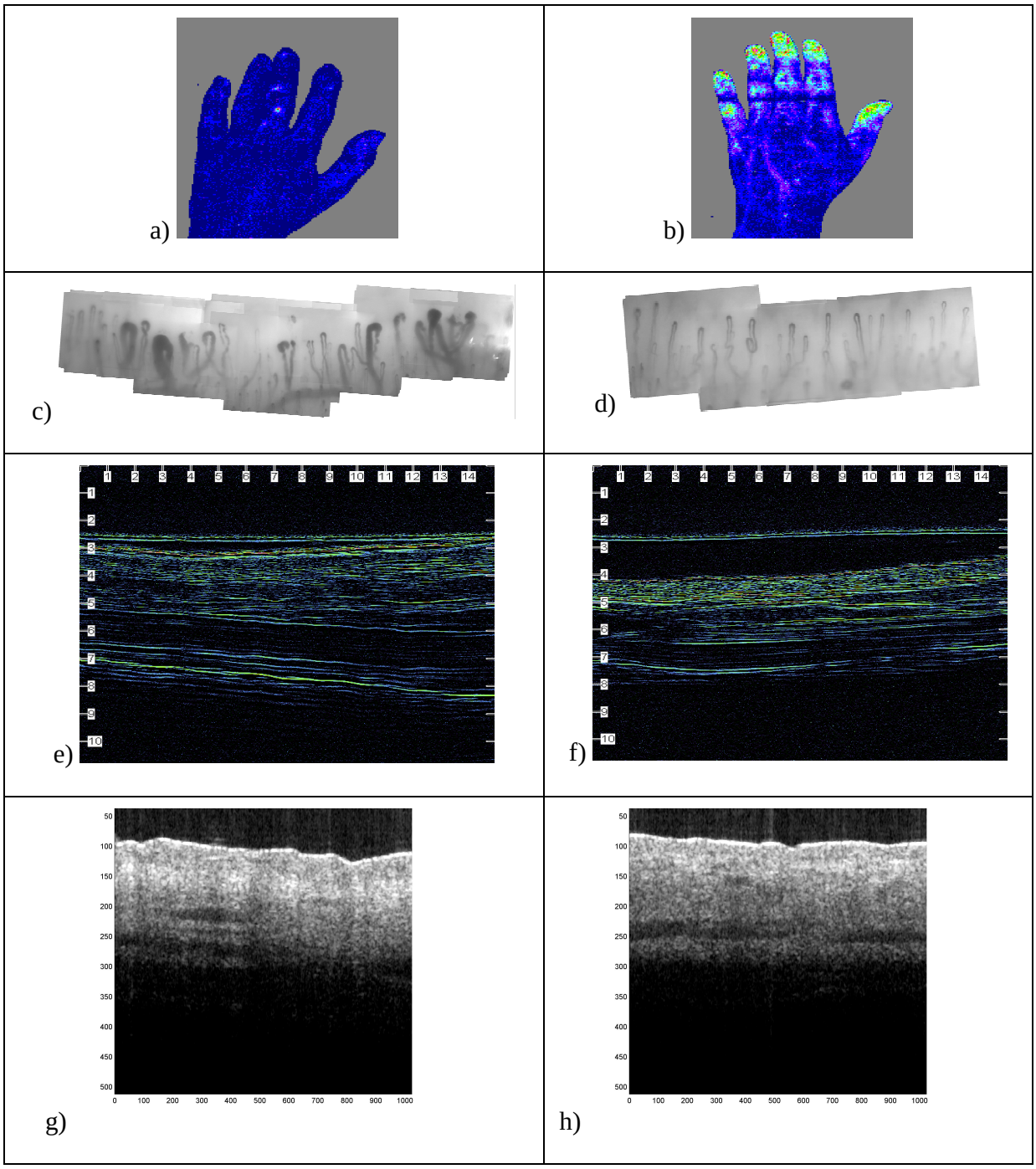

Figure 7.1. Example images from the study data set. Left column are SSc patient images (SSc), right column are control images (HC). From top to bottom images are: a) SSc LDI, b) HC LDI, c) SSc nailfold capillaroscopy, d) HC nailfold capillaroscopy, e) SSc high-frequency ultrasound, f) HC high-frequency ultrasound, g) SSc OCT and h) HC OCT.

7.4.1 Analysis

Once imaging of all subjects was complete, data from the four techniques used were analysed as described below.

LDI images: These images can be analysed using the software provided by Moor Instruments as part of the system. The perfusion level at a particular point in a sample is represented in the image as a colour. The perfusion at specific points, or an average perfusion over a defined region-of-interest (ROI), can be extracted using the software GUI. For each image from this study, three ROIs were defined: (1) the full width of the distal ring finger between the nail and the first joint, (2) The proximal ring finger between the knuckle and the middle joint, (3) the entire dorsal area of the hand describing a distorted rectangular shape with borders at the knuckles, the wrist and either edge of the hand. For each of these ROIs the software produces a numerical measure of average relative perfusion, along with a standard deviation over the ROI. The same process is performed for images produced with both red and green lasers. When all images have been analysed the results are tabulated for statistical analysis.

Nailfold capillaroscopy: These images are assessed using a combination of manual and automatic analysis. Human input is required to identify the top of each individual capillary; the top being the turning point of the vessel as it describes an approximately 180 degree direction change. Once the images have been marked in this way a software program automatically measures each capillary for parameters such as size, tortuosity ("twistiness") and distribution density. These parameters are then tabulated for statistical analysis.

High-frequency ultrasound and OCT images: These two sets of images are analysed in the same way since they are both two-dimensional tomographic "slices" into the tissue. Custom software, including a GUI front-end (see Figure 7.2), developed within the Matlab environment is used to identify boundaries between tissue layers in the images. The images are loaded and a 30-pixel-wide vertical slice is selected at a point in the

image where the surface and subsequent boundaries appear to be flat. The slice is averaged in the horizontal direction to produce a single depth profile through the tissue layers. Peaks in this profile with amplitude higher than a user-adjustable threshold are identified as tissue layer boundaries. The depth of each layer can then be calculated by counting the number of pixels between the peaks. For each body site imaged, two frames (two sections per frame) were analysed and the results averaged.

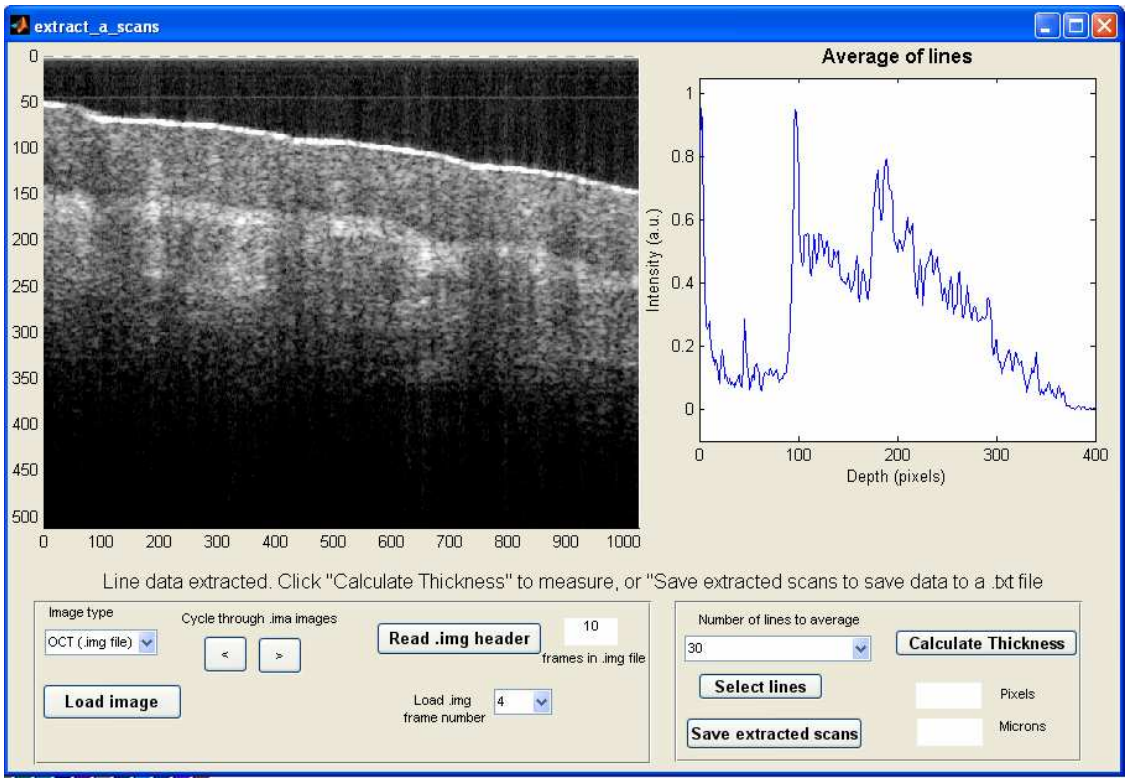

Figure 7.2. Screenshot of Matlab software with GUI used for analysing OCT and ultrasound images.

7.5 Results

The analysis of images taken during this study is an ongoing process. So far, skin thickness measurements (epidermis) from the OCT and high-frequency ultrasound images have been obtained. Statistical testing to enable the comparison of these results

between patient and control groups has also been performed. The following table details the results of these thickness measurements for 10 body sites, averaged over 20 patients.

	High-frequency ultrasound – Mean(SD) (µm)			OCT – Mean(SD) (µm)		
	SSc patient	Control	P-value	SSc patient	Control	P-value
Distal dorsal ring finger	264.4(40.6)	240.3(32.9)	0.0232	97.4(40.3)	89.2(23.8)	0.2200
Proximal dorsal ring finger	260.6(45.4)	243.8(35.0)	0.0979	135.5(32.9)	125.5(41.6)	0.2022
Distal palmar ring finger	280.8(60.5)	280.8(60.5)	0.4741	162.6(56.9)	163.9(32.0)	0.4674
Proximal palmar ring finger	282.2(44.7)	283.5(42.4)	0.4638	157.0(55.3)	161.8(56.9)	0.3954
Dorsum	206.0(36.7)	184.7(35.9)	0.0356	125.7(18.2)	115.3(16.0)	0.0306
Dorsal foreram	214.6(44.0)	197.8(34.6)	0.0968	97.0(19.9)	92.9(14.2)	0.2276
Volar forearm	195.2(32.9)	183.3(32.9)	0.1304	94.5(20.9)	100.0(20.6)	0.2052
Dorsal upperarm	196.3(41.3)	200.4(38.7)	0.3758	95.1(16.9)	99.4(12.3)	0.2018
Volar upperarm	208.4(46.1)	214.1(54.3)	0.3642	92.8(17.8)	88.3(14.4)	0.1992
Chest	165.8(24.7)	166.9(21.8)	0.4464	90.6(14.3)	84.3(14.0)	0.0886

Table 7.1. Epidermal thicknesses, as measured with ultrasound and OCT.

7.6 Discussion

Firstly, it should be noted that the results shown here are a first analysis of the OCT and ultrasound data. The identification of boundaries within these images once a depth profile has been extracted is, at best, difficult. The relatively low contrast available in these images, coupled with issues relating to flatness and uniformity results in many false-positive tissue boundaries being found. These false boundaries have to be checked and removed manually, which is an enormous task given that data is extracted from 800 frames for each of the techniques. It is hoped that changes in the analysis software can improve the accuracy and reliability of this data.

Considering the results in Table 7.1, generally it can be seen that, as expected, patients with SSc tend to have a thicker epidermal skin layer than control subjects at almost all of the body sites measured. However, in almost all cases this observed difference is not statistically significant; that is a p-value of greater than 0.05 is calculated.

The only statistically significant results are for the dorsum site (both techniques) and the distal dorsal finger site (ultrasound only). This means that in these cases a difference in epidermal thickness was measured between SSc patients and healthy control subjects.

Data from the other imaging techniques is in the process of being analysed. Once this is complete all 4 datasets will be added to a more sophisticated statistical model to look for further correlations. Although not shown here, a preliminary analysis of the LDI data appears to show no difference in perfusion between patient and control subjects. This is as expected, since differences in vascular response between the two groups are only manifest when some challenging stimulus, such as heating or cooling, is applied.

7.7 Conclusions

A study comparing patients with systemic sclerosis to a group of healthy control subjects was carried out at Salford Royal Hospital. Subjects were imaged using four imaging techniques looking particularly for differences in skin thickness and microvascular structure. Although analysis is ongoing, the results for the OCT and ultrasound techniques suggest that differences in epidermal thickness between patients and controls can be detected by both techniques, although not so far to a statistically significant level. There is poor agreement between the two techniques as they both give different values for the skin thickness at the various locations. This is probably due to a number of factors including the small number of patients in the study and the fact that each patient has skin that is non-homogeneous and can vary widely from any accepted normal value. There is also probably a high rate of measurement error inherent in the study since it can never be certain that the ultrasound and OCT images are taken from precisely the same location on the skin.

Further data analysis and statistical modelling is planned and will include data from all four imaging techniques, as well as various demographic and medical information sources.

7.7.1 Acknowledgments

The author would like to thank Donna Buckley for her marathon image analysis efforts, and also for putting together the analysis software into its final form, including the brilliant GUI. Also, Je Song Shin (Jason) is acknowledged for his help with analysing some of the LDI data, as well as providing an extra pair of hands during the study. Finally, thanks go to Tonia Moore for all her help with organising this study, especially in recruiting subjects.

References

[1] M. E. Anderson, T. L. Moore, M. Lunt et al., *Rheumatology (Oxford, England)* **46** (3), 533 (2007).

[2] M. E. Anderson, P. D. Allen, T. Moore et al., *The Journal of rheumatology* **32** (5), 841 (2005).

[3] M. E. Anderson, T. L. Moore, S. Hollis et al., *Rheumatology (Oxford, England)* **41** (3), 324 (2002).

[4] *Thorlabs swept source OCT system - operating manual*. (Thorlabs Inc., 2007).

[5] T. L. Moore, M. Lunt, B. McManus et al., *Rheumatology (Oxford, England)* **42** (12), 1559 (2003).

[6] *Episcan I-200 operating manual*. (Longport, Inc., 2007).

Chapter 8

Conclusions & further work

8.1 Conclusions

The following conclusions can be drawn from the work presented in this thesis.

Firstly, a high-speed OCT imaging system has been designed and built and is now in the final stages of testing and optimisation. The original design brief was to build a fast imaging OCT system capable of "video rate" output and the ability to resolve structures at the scale of the microcirculatory system in humans. Every component of the system has been characterised, and its suitability assessed against the original design brief. Initially, a pre-prototype system was constructed to allow component testing; for example in measuring the stability of the SLD light source. This test system provided answers to most component issues and allowed the final system design to be finalised. An interferometer design was chosen to maximise signal-to-noise ratio, using dual balanced detectors to theoretically enable shot noise limited performance to be achieved. Various associated electronics problems relating to signal timing and image acquisition were analysed and solved.

Chapter 3 presents some initial images taken using the system (Figures 3.28 and 3.29), and highlights the areas which still require some work. These images show that the system is not providing images limited only by the properties of the light source. Simple electronic filtering, coupled with a sub-optimal objective lens, result in resolving performance being between 3 times and 5 times worse than it should be. These issues are in the process of being resolved to enable the OCT system to be used for its intended purpose of imaging human skin in vivo.

Secondly, a compact supercontinuum light source, the SuperK from Koheras, was tested and characterised in Chapter 4, in order to see if such sources are suitable for integration into OCT imaging systems. Although the source provided large bandwidths and high optical powers, it also had problems associated with the pulsed nature of its output, along with high noise levels. Time constraints limited the testing of the source to basic parameters, but enough information was available to conclude that the source is unsuitable for use in OCT imaging. Other versions of the same light source with higher optical power outputs and much higher pulse rates (in the megahertz rather than kilohertz range) may be worth thinking about for OCT imaging. This is because no other light source is currently available with the potential for such high resolution imaging due to the massive broadband output of these supercontinuum sources.

Chapter 5 describes a liquid-based blood flow model that was constructed and imaged using a commercial Doppler OCT (DOCT) system. The flow model allowed the testing of the capabilities of DOCT in imaging small flow volumes when surrounded by scattering media. This model is a simple analogue to blood flow within vessels surrounded by scattering tissues, the conditions aiming to be imaged with the system described in Chapter 3. Most scattering solutions used in the model were made using diluted Intralipid, a solution of predominantly fat molecules suspended in water, with an appearance similar to milk. Adjusting the concentration of the solution allows different scattering properties to be obtained, in turn allowing an approximation to blood flowing in a vessel within a surrounding tissue matrix to be imaged. Solutions of polystyrene microspheres were investigated as these would seem to be a more suitable model for the cellular components of blood in particular. These were found to be difficult to work with as the flow rates tested were too low to keep the spheres in solution. DOCT images of all situations were recorded, with false-colour imaging used to represent Doppler-induced phase shift in dynamic situations. The possibility of extracting velocity profiles across the vessels in these images was also investigated, although this wouldn’t be possible in vivo due to the much reduced size of the vessels in the human microcirculation.

In Chapter 6 two OCT systems utilizing different wavelengths (1300nm and 930nm) were used to image the skin of certain species of neo-tropical tree frog. This was in an attempt to isolate the location of an unusual pigment called pterorhodin, which apparently allows the frogs to bask in the sun for longer than those without the pigment. Although the results were ultimately inconclusive, this is the first time that OCT imaging has been used to study these creatures.

Finally, a clinical study of skin thickening and blood flow in patients with scleroderma compared to healthy controls was carried out, and this was discussed in Chapter 7. Twenty subjects from each group (40 in total) were imaged using OCT, high-frequency ultrasound (HFUS), nailfold capillaroscopy, and laser Doppler imaging. Patients suffering from scleroderma generally have thickened skin and poor peripheral circulation in areas of the body such as hands and feet. As expected, analysis of both OCT and HFUS images independently show the thickened skin in patients when compared with healthy control subjects. The agreement between the two techniques is poor, with (for example) each technique suggesting a different absolute thickness for a particular skin layer within a specific patient. Laser Doppler imaging and nailfold capillaroscopy both showed the expected result of reduced peripheral blood perfusion in the hands of scleroderma patients when compared to healthy control subjects.

8.2 Further work

The OCT system designed, built and tested in Chapter 3 certainly warrants further work in improving imaging performance and overall usability. As mentioned previously, the current electronic signal processing used does not work well and needs to be replaced with something more suitable. Signal processing techniques to extract the “envelope” of the interference signal can be applied, either in hardware or software to form the static OCT images required. Replacing the objective lens with a higher numerical aperture part should enable increased image contrast and improved lateral resolution. A 30 mm focal length, 25.4 mm diameter lens will be used here, and has the added practical advantage of

shortening the working distance from hand probe to sample. Improved system software is also being implemented by another student to make the system more reliable and easier to use in general.

Linking the work in Chapter 3 to that in Chapter 7; the ultimate goal for the OCT system is to be used in clinical studies on patients with various skin and microcirculatory conditions (scleroderma, psoriasis, morphea, etc.). When the suggested improvements to the system are carried out it will be ready for use in future studies. There are several of these currently planned including one that copies the format of that discussed in Chapter 7, but replacing scleroderma patients with patients with morphea. Morphea is a localised condition; patients typically have patches of affected skin which is generally thicker and has increased blood perfusion, making it ideal for both affected and unaffected areas to be imaged and compared.

Further work imaging tree frogs with OCT could potentially give some useful results. The study described in Chapter 6 could have given conclusive findings if an absolute measure of optical power was available for all measurements. This would allow the intra-species comparison of skin depth profiles and give a good idea which frogs reflect strongly from a specific layer within their skin. One way of doing this would simply be to measure optical power incident on the frog at several wavelengths during each imaging session.